CRANFIELD UNIVERSITY

Rachel Nichols

Material Characterisation, Testing, and Modelling of Finite Element Analysis of Impact Structures

School of Engineering
MSc by Research

MSc
Academic Year: 2011 - 2012

Supervisor: Rade Vignjevic
October 2012

CRANFIELD UNIVERSITY

School of Engineering
MSc by Research

MSc

Academic Year 2011 - 2012

Rachel Nichols

Material Characterisation, Testing, and Modelling of Finite Element Analysis of Impact Structures

Supervisor: Rade Vignjevic
October 2012

ABSTRACT

Formula One race cars have to pass rigorous safety tests before they are allowed on track. This type of testing has been in place for years but the requirements for testing are continually increasing in order to reduce the amount of risk to the drivers' safety during a race. The number of structures that need to be made and tested can quickly make this process an expensive one. Additionally, it is necessary to pass the mandated tests within a reasonable amount of time so as not to have an impact on the development on the rest of the car. There is a desire to reduce the number of structures needed for testing through finite element analysis (FEA), and as such, to reduce the time needed to pass the safety tests. FEA of laminated composites can be complex and is a balance between accuracy and the time it takes to find a solution.

The current project looks into increasing understanding of the requirements for material characterisation, experimental impact testing, and explicit simulation of a carbon fibre fabric pre-impregnated with epoxy resin. Mercedes-Benz Grand Prix (MGP) Formula One Team has provided a pre-preg material for evaluation. Material experiments were performed per the American Society for Materials and Testing (ASTM) in order to find the tensile modulus, tensile strength, Poisson's ratio, compressive strength, shear modulus, and shear strength of the material. Nine tubes were manufactured at MGP and tested in the drop tower at the Cranfield Impact Centre (CIC).

The explicit solver of the software program LS-DYNA was used to model the material tests performed while evaluating the material models 022, 054, 055, 058, and 158.LS-DYNA was then used to simulate the drop tower tests. The tube was modelled using shell elements and material model 055, which uses Chang-Chang for tensile and compressive fibre mode failure and Tsai-Wu for tensile and compressive matrix mode failure. An emphasis was placed on matching the simulation results with the unfiltered experimental data, especially the initial peaks loads present in the data. The effects of simulation parameters were looked into such as time-step for element deletion, hourglass viscosity type, softening of crashfront elements, and the contact stiffness between the

tube and the impacting wall. It was found that the physical modelling of the tube had the largest effect on the simulation results. The physical modelling consisted of the chamfered trigger, the mesh distribution, and the mesh size. An interesting finding is that an irregular mesh was necessary to prevent the tube from losing contact with the impacting wall.

Keywords:

Formula One, material model validation, LS-DYNA

ACKNOWLEDGEMENTS

I would like to thank my supervisor, Rade Vignjevic, for his guidance this past year; the Cranfield Impact Centre for supporting this project; and finally, everyone at Mercedes GP for their enthusiastic support.

TABLE OF CONTENTS

LIST OF FIGURES

LIST OF TABLES

LIST OF EQUATIONS

LIST OF ABBREVIATIONS

CU	Cranfield University
MGP	Mercedes-Benz Grand Prix
CIC	Cranfield Impact Centre

1 Introduction

1.1 Objective

This study was undertaken to increase understanding of the necessary parameters needed to perform a predictive crash analysis using FEA software.

1.2 Background and Motivation

The requirements for crash testing of Formula One race cars have been increasing and the amount of time available to pass the tests has become smaller. All of the crash testing must be complete before the car undergoes any track testing. Previously, the crash testing had to be complete before the first race of the season, which gave the teams an extra month in their crash testing schedule. While it is possible to pass all of the crash tests using an iterative design process without the use of finite element analysis software, it can be a costly and time-consuming approach.

A more desirable approach would be to use a crash analysis software to create the first design of the structure. Further iterations could then be used to optimise the structure; reducing the weight and making the car safer for the driver. Currently, it can be difficult to accomplish the first successful iteration of the design before the required deadline, let alone have the luxury of optimising the design. Reducing the mass of the impact structures on the car will contribute to the overall performance of the car. And while the sport of Formula One is known for extravagant budgets, the teams have become increasingly more aware of opportunities for cost savings. There is a need to reduce the amount of full-scale crash testing iterations that can occur in order to pass the crash tests.

1.3 Methodology

The plan for this project was to perform material testing and small coupon testing of a given prepreg material. The material testing was done through known, accepted standards for composite material testing. The coupon testing was performed with a drop tower and using a geometry that was known to be satisfactory for the impact energy of the drop tower.

After analysing data from the material testing, single element finite element analyses were performed using the material properties found in order to compare available composite material models in LS-DYNA. Simulations replicating the material tests were also performed.

Simulations were then done of the coupon testing in the drop tower. Through these simulations, various parameters were examined for their effect on the simulation results. An emphasis was placed on matching the peak unfiltered load from the tests and the simulations.

2 Literature Review

2.1 Composites in Racing

The Federation Internationale De L'Automobile (FIA) is the governing body for the Formula One Championship. The FIA has been dictating the safety rules of the sport since 1963 with ever increasingly stringent requirements for crash testing (Mellor, 2002).

The first carbon fibre monocoques in F1 were introduced by teams McLaren and Lotus during the same year of 1981. The monocoque by McLaren was similar to contemporary monocoque construction and was built by an American aerospace composites manufacturer, Hercules Corporation. The monocoque by Lotus was closer to the previous generation of aluminium-skinned honeycomb monocoques in that it was constructed from flat sandwich panels of honeycomb with carbon fibre skins utilising the "cut and fold" method (Wright, 2001, p. 315).

At this time, composites structures were not believed to be good in impact situations mainly because of issues seen with Rolls-Royce's RB211 carbon fibre fan blades during bird-strikes (Wright, 2001, p. 235). Savage noted, "Indeed many designers of repute expressed grave doubts as to the suitability of such brittle materials in what is a highly stressed application" (Savage, 2010, p. 100). However, that belief was changed after John Watson's 1981 crash in the McLaren carbon fibre monocoque, from which "he was able to walk away from the debris unscathed" (Savage, 2010, p. 100). Since their introduction into F1, monocoque manufacturing has remained relatively the same.

It is desirable to use composite materials in structures, specifically when combined with honeycomb, because of their high strength to weight ratio. Composites have another advantage in that they can have "controlled anisotropy," which means the laminate schedule of a composite can be tailored so it meets the loading requirement (Agarwal et al., 2006).

2.2 Composite Failure Modes

Brittle composite materials fail with a different failure mode than ductile metals. Hull states that, “Tubes made from these materials, which are homogeneous, isotropic and ductile, collapse by progressive plastic folding. The fold geometry and the collapse loads depend on the shape and dimensions of the tubes and can be predicted with some accuracy” (Hull, 1991, p. 378-379). In contrast, it is difficult to accurately model the energy-absorption of a composite structure. Composite structures can fail with a progressive crush that has the ability to absorb more energy than plastic folding. When composite structures fail, a crashfront is formed that moves along the structure during impact (Hull, 1991, p. 379).

Composite structures exhibit four main failure modes when under impact: transverse shearing, brittle facture, lamina bending, and local buckling (Farley, 1992). Farley has described these failure modes and attempted to relate the energy-absorbing capability of a structure to changes in the mechanical properties of its materials (Farley, 1992, p. 7). It was found that parameters such as fibre orientation and laminate stacking sequence will dictate the failure mode of the tube and in turn, the overall energy-absorption of the structure (Farley, 1992, p. 12).

2.3 Scaling of Composite Structures

In the beginning of the project, scaling of composites structures was researched as a possible solution to costly full-scale testing. Composite testing can be an expensive process, especially for large aircraft structures. It would be desirable to be able to perform testing on a scaled-down version of the structure (Jackson, 1994). While testing of scaled-down composite structures has seen some success in aircraft design, it is not suitable for use in impact analysis of energy-absorbing structures. The first reason for this is because the scaled-down structure and the full-scale structure must exhibit the same failure modes (Dormegnie et al., 2003). It has already been shown that the failure mode of a structure is highly dependent on geometry ratios. The second reason this approach will not accurately predict the energy-absorption of a structure is

because small-scale tests “underestimate the damage that develops in larger structures under scaled impacts” (Tarfaoui et al., 2007). Similarly, Voit found that similitude laws used for scaling structures do not apply when the structure is damaged (2008). Again, it has been shown that the main mode of energy-absorption for composite structures is through the structure breaking apart. It can be then decided that testing of scaled-down structures is not a viable option for predicting the energy-absorption of the full-scale structure. It is better to focus on accurately modelling composites in FEA.

2.4 Composite Tubes

A progressive crush is desired and to achieve this with circular tubes, the thickness to diameter ratio should be 0.02 and the length to diameter ratio should be 1.5. These critical ratios were shown to be “almost identical for static and dynamic tests” (Mamalis et al., 1994, p. 675).

Mamalis found that carbon fibre circular tubes with an epoxy resin absorbs more energy than an equivalent structure made from fibreglass and epoxy resin (1997, p. 131).

2.5 Composite Cones

Most composite structures require a trigger in order to initiate a progressive crush of the structure. However, with a conical geometry, failure is initiated at the small end of the cone and the structure does not need a machined trigger in order to experience a progressive crush (Price and Hull, 1987). This is an advantage to using cones instead of straight circular tubes because it removes the inconsistency of manufacturing and properly modelling the trigger.

Rezadoust found that empty cones constructed of fibreglass and epoxy resin, with a diameter to thickness ratios of 160, 250, and 390 and angles of 0, 11, and 22 failed by severe buckling and were not good energy-absorbers (2008, p. 149). This range of ratios will be avoided in order to have a progressive crush of the structure.

Mahdi has shown that the failure mode of cones made from carbon fibre and epoxy is very sensitive to the angle of the cone (2002, p. 289). The average load on the structure will increase as the angle is increased, while the initial peak load will be lowered.

2.6 Material Models

Bisagni compared experimental results from testing of carbon fibre composite cones with simulations created in LS-DYNA. MAT_054, MAT_055, and MAT_058 were compared. It was found that MAT_055 was the only material model to match the average load of the experiments and also exhibited a brittle failure while the others failed in a ductile manner (2005, p. 494).

Kubiak also compared experimental results with simulations in LS-DYNA. The experiments were performed on straight, circular tubes and the simulations were done using MAT_022, MAT_054, MAT_055, and MAT_059. Again, MAT_055 was able to match the experimental results better than the other material models but it was not possible to visualise the correct failure mode with this model (2007).

3 Material Testing

The material supplied for this study is a prepreg from Umeco (formerly known as Advanced Composites Group) with Hexcel fibres IM7 and Umeco epoxy resin MTM249. The fibre tows of IM7 are woven into a 2x2 twill fabric and the prepreg has 42% resin by weight.

MGP has supplied material data, which was originally provided by Umeco, for this prepreg. The properties given by MGP can be seen in Table 1.

Table 1: Given Material Properties

Density ($\frac{kg}{mm^3}$)		1.480×10^{-6}
Cured Ply Thickness (mm)		0.235
ν_{12}		0.05
Stiffness (GPa)	E_{11T}, Longitudinal Tensile Elastic Modulus	64.6
	E_{11C}, Longitudinal Compressive Elastic Modulus	60.9
	E_{22T}, Transverse Tensile Elastic Modulus	64.6
	E_{22C}, Transverse Compressive Elastic Modulus	64.4
	G_{12}, Shear Modulus in the 1-2 Plane	3.57
	G_{23}, Shear Modulus in the 2-3 Plane	2.37
	G_{31}, Shear Modulus in the 3-1 Plane	2.37
Strength (MPa)	σ_{11T}, Longitudinal Tensile Stress	960
	σ_{11C}, Longitudinal Compressive Stress	607
	σ_{22T}, Transverse Tensile Stress	881
	σ_{22C}, Transverse Compressive Stress	586
	τ_{12}, Shear Stress in the 1-2 Plane	112
	ILSS, Interlaminar Shear Strength	77

Prepreg manufacturers do not always test every combination of resin content available and instead may provide material properties that are scaled based on the results of testing of a material with a different percentage of resin. It is unclear if the material properties provided by Umeco are scaled values or if they provided values from testing the actual 42% resin weight prepreg. Specific shop processes can affect the cured properties of the material so it is good practice

to always perform material testing. Manufacturing aspects such as cure cycle, laminator technique, cleanroom cleanliness, and the total time the material has spent outside of the freezer can influence the final performance of the material. As such, it was decided to perform some material testing to verify the given values.

There are a variety of material tests that have to be performed in order to fully populate a LS-DYNA material model. The tests performed are as described below. Additional testing that could further enhance the material models are also discussed but could not be performed due to time constraints of the project.

3.1 Composite Material Orientation

Prepreg material can be used in a unidirectional state or the tows can be woven into a fabric. Both unidirectional and woven materials have a longitudinal and transverse direction. Longitudinal and transverse can also be referred to as warp and weft, respectively. The longitudinal direction corresponds to the direction of the material that the fibres follow. For unidirectional materials, this is easy to identify because all of the fibres lay flat and point in the same direction. The transverse direction of a unidirectional material is referred to as the matrix direction. For a woven fabric material, it can be more difficult to identify the longitudinal direction. The longitudinal direction for a woven material is best described as the direction that the material comes off the roll. A diagram of this can be seen in Figure 1.

Quite a few woven fabrics are considered to be balanced materials, meaning that they have the same properties in the longitudinal and transverse directions. While this is true for a plan weave fabric, it is not necessarily true for a twill or harness satin. Even so, it is common practice to treat a twill as a balanced fabric. In the case of an unbalanced fabric, the longitudinal direction is usually the direction with higher strength and modulus properties.

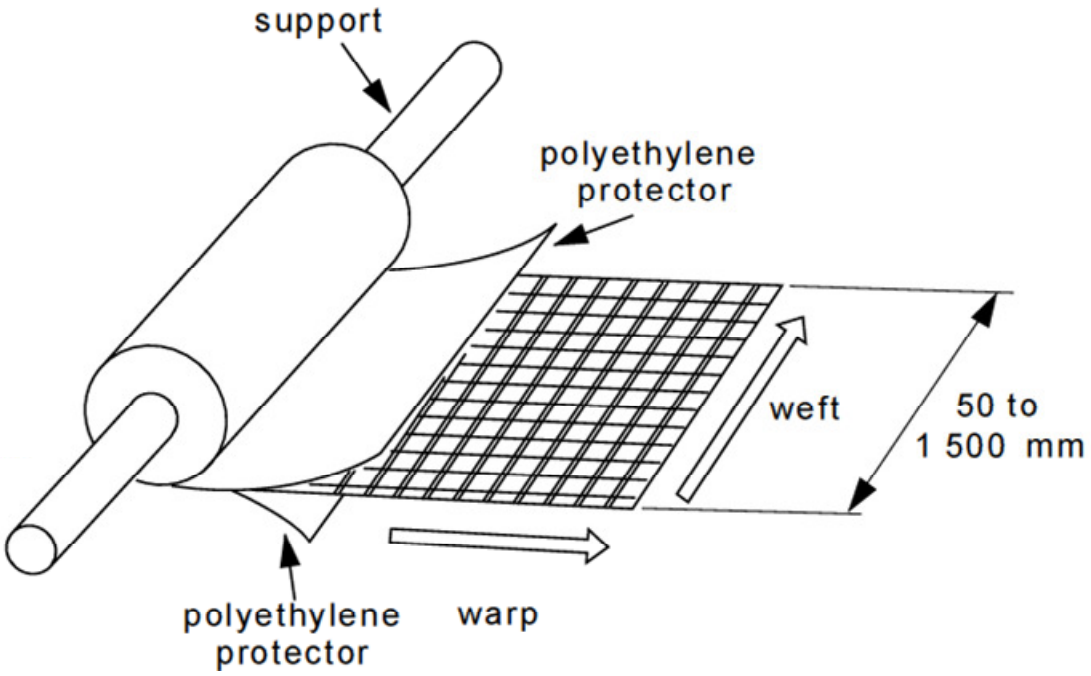

Figure 1: Warp and Weft Diagram.

Source (Hexcel Corporation, 2005, p. 4)

When speaking about the material coordinate system used for finite element analysis, the x-direction corresponds to the 1-axis, the y-direction corresponds to the 2-axis, and the z-direction corresponds to the 3-axis. The shear stresses act on a face perpendicular to the principal stresses. This can be seen in Figure 2. The 1-axis is the axis from which the material orientation is measures. Therefore, the 1-axis also corresponds to a material angle of 0 degrees while the 2-axis corresponds to 90 degrees.

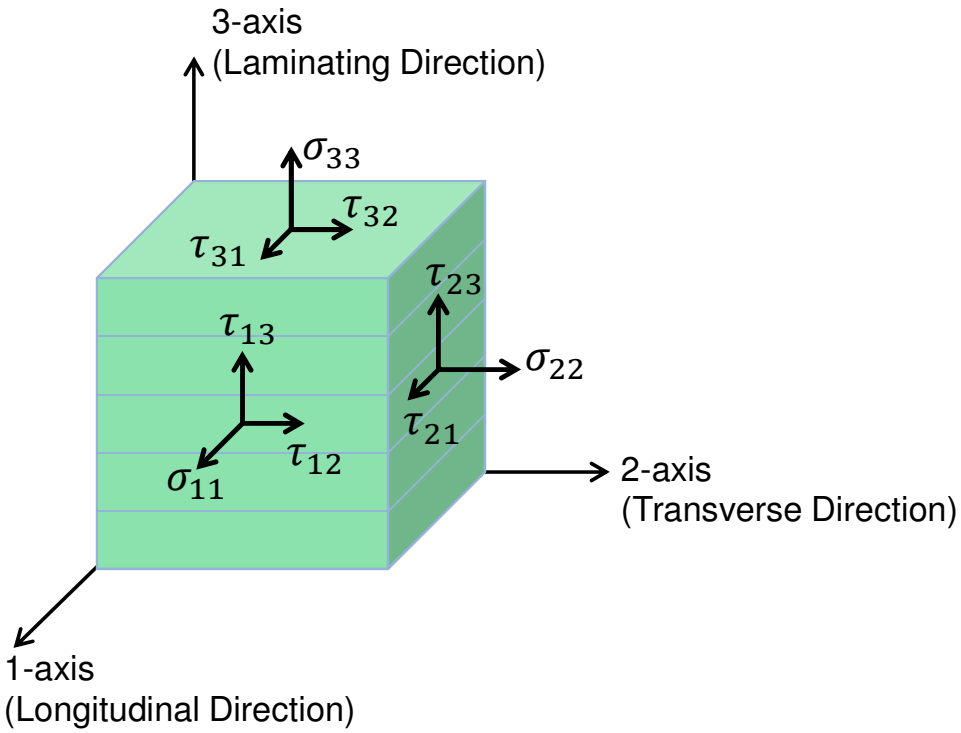

Figure 2: Material Coordinate System

Source: Adapted from (ASTM Standard D5379/D5379M, 2005, p. 2)

The above described terms of longitudinal, transverse, 0 degrees, 90 degrees, and the material coordinate system convention will be used throughout remainder of this text.

3.2 Tensile Properties

3.2.1 Testing

Tensile testing was performed per ASTM D3039 Standard Test Method for Tensile Properties of Polymer Matrix Composite Materials. Through tensile testing, the ultimate tensile strength, ultimate tensile strain, tensile modulus, and Poisson's ratio of the material was found. All tests were performed at room temperature. Sixteen specimens were made in total. Eight of the specimens had all plies oriented with the 0 degree direction parallel to the axis of loading. These will be referred to as the "0 degree tensile" specimens. The remaining eight specimens had all plies oriented with the 0 direction perpendicular to the loading direction. These will be referred to as the "90 degree tensile"

specimens. Each specimen had 11 plies oriented as described above which resulted in a nominal thickness of 2.585 mm. ASTM D3039 recommends a thickness of 2.5 mm for specimens made of woven fabric (ASTM Standard D3039/D3039M, 2008). Each specimen was 250 mm long and 25 mm wide. Fibreglass tabs that were 56 mm in length were bonded to each end and on either side of each specimen, as recommended by the specification. This resulted in an approximate gauge length of 150 mm. Figure 3 shows a typical tensile specimen. A drawing of the specimen profile can be seen in Figure C-9. The actual cross-sectional dimensions of each specimen, measured with callipers, can be seen in Table 2.

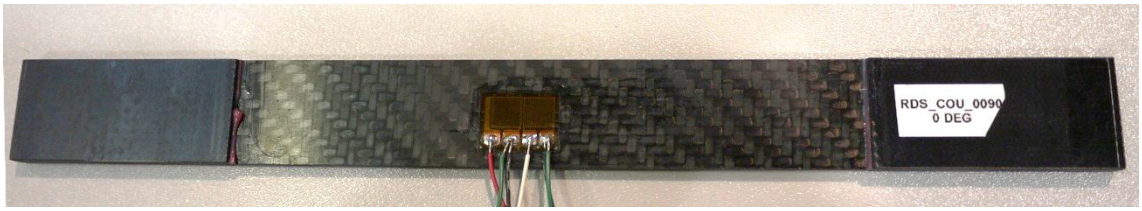

Figure 3: Tensile Specimen

Table 2: Tensile Specimen Dimensions

Specimen Number	Type	Width (mm)	Thickness (mm)	Cross sectional area (mm^2)
1	0	25.63	2.28	58.4
2	0	25.81	2.8	72.3
3	0	25.69	2.65	68.1
4	0	25.79	2.73	70.4
5	0	25.59	2.62	67.0
6	0	25.59	2.65	67.8
7	0	25.88	2.48	64.2
8	0	25.78	2.66	68.6
1	90	25.8	2.42	62.4
2	90	25.58	2.49	63.7
3	90	25.65	2.34	60.0
4	90	25.97	2.46	63.9
5	90	25.73	2.29	58.9
6	90	25.82	2.48	64.0
7	90	25.47	2.28	58.1
8	90	25.46	2.47	62.9

Each specimen had a 90 degree tee rosette strain gauge bonded to its surface in order to measure the tensile modulus and Poisson's ratio. The 90 degree tee rosette consists of two general purpose strain gauges placed at 90 degrees to each other on the same matrix backing. Each gauge is labelled by a numeral on the matrix backing close to the gauges. The 90 degree tee rosette was oriented on each specimen so that the sensing axis of gauge 1 is parallel with the loading axis and on the centreline of the specimen. The sensing axis of gauge 2 is perpendicular to that of gauge 1 so it is also perpendicular to the loading axis. Figure 4 shows a 90 degree tee rosette bonded to a tensile specimen. Gauge 1 is on the left-hand side and gauge 2 is on the right-hand side.

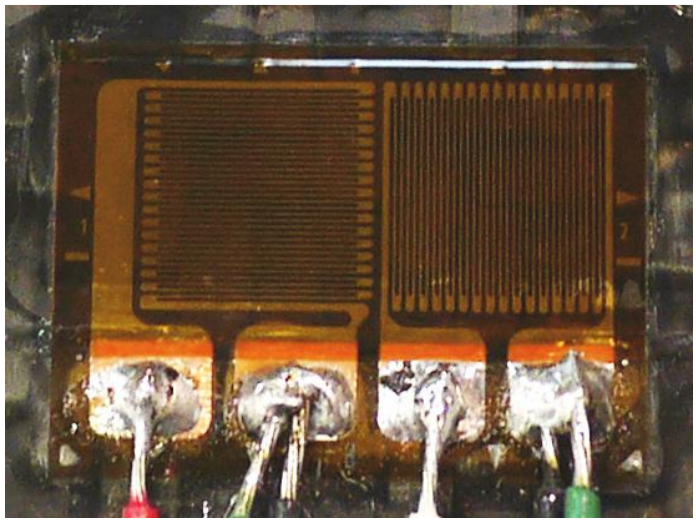

Figure 4: 90 degree tee rosette bonded to specimen

The gauge length of each strain gauge was 6.35mm. The strain gauges were ordered from Vishay Precision Group's Micro Measurements. The part number of the strain gauges is CEA-06-250UT-350. These strain gauges should be used with materials that have coefficients of thermal expansion similar to steel, in the range of 9.0-13.5 $\frac{mm}{mm℃}$ (Vishay Precision Group, 2010) It would have been preferable to use strain gauges for materials with lower coefficients of thermal expansion that are closer to a carbon/epoxy composite, however, the lead time for these gauges did not work within the project schedule. The measured values from the strain gauges will be adjusted to compensate for this difference. The measurements from gauge 2 will be further adjusted as it needs to be corrected for transverse sensitivity because the main sensing axis of the gauge was not aligned with the loading axis. A description of the compensation used on the results from the gauges can be seen in Appendix B.

Each specimen was testing using a 200 kN Instron machine, model 5582 (Figure 5). The specimens were held in the machine by mechanical wedges grips (Figure 6). Care was taken to make sure the specimens were aligned when placed in the machine in order to reduce bending in the specimen during testing. A tensile specimen fitted in the Instron machine can be seen in Figure 7

Figure 5: 200kN Instron Machine

Figure 6: Mechanical Wedge Grips

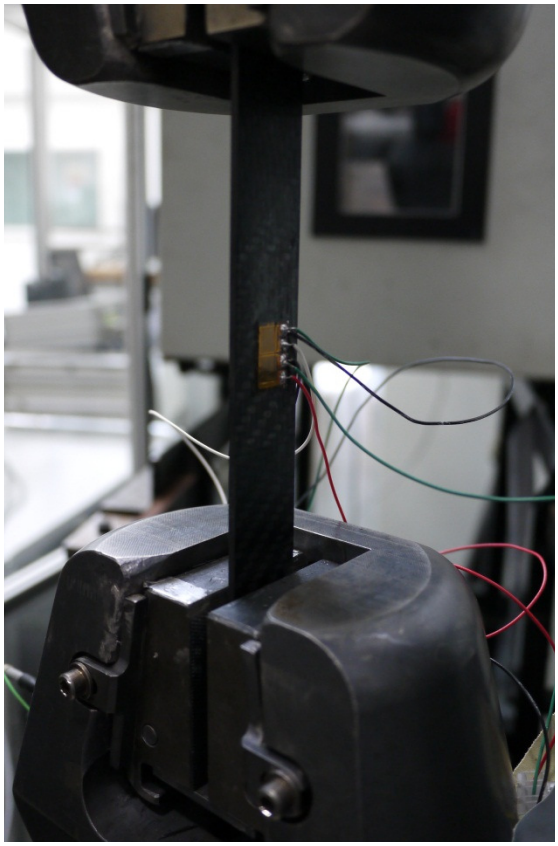

Figure 7: Tensile Specimen in Instron Machine

The bending in the specimen can be measured during a tensile test by bonding another strain gauge to the opposite side of the specimen and comparing the output from all gauges; however, this was not done as it would increase the number of strain gauges needed. The speed of testing was set at $2\frac{mm}{min}$ and each specimen was tested to failure. The strain in microstrain ($\mu\varepsilon$) from each gauge and the load in kilonewtons (kN) from the Instron machine were recorded at 200 Hz during each test.

3.2.2 Results

The tensile strength for each specimen was calculated by dividing the load at failure by the cross-sectional area of the specimen (Equation 1).

$$\sigma_{max} = \frac{P_{max}}{A} \qquad \textbf{Equation 1}$$

The tensile chord modulus was calculated by dividing the change in stress by the change in strain (Equation 2). The strain range used for this calculation was 1000 $\mu\varepsilon$ to 3000 $\mu\varepsilon$.

$$E = \frac{\Delta\sigma}{\Delta\varepsilon} \qquad \textbf{Equation 2}$$

Poisson's ratio was calculated by dividing the negative of the change in transverse strain by the change in longitudinal strain. The strain range used for this calculation was also 1000 $\mu\varepsilon$ to 3000 $\mu\varepsilon$.

$$\upsilon = \frac{-\Delta\varepsilon_t}{\Delta\varepsilon_l} \qquad \textbf{Equation 3}$$

Two of the data sets for the 0 degree tensile specimens could not be used because the data was incorrectly recorded during the tests. This happened for specimen 1 and specimen 4. The results from the usable data sets can be seen in Table 3. Graphs of the test data can be seen in Appendix A.

Table 3: Tensile Specimen Results

Specimen Number	Type	Maximum Load (kN)	Tensile Strength (GPa)	Tensile Modulus (GPa)	Tensile Strain	Poisson's Ratio
2	0	58.2	0.805	61.2	0.012	0.0518
3	0	64.1	0.941	66.4	0.013	0.0451
5	0	67.0	1.00	66.6	0.014	0.0390
6	0	68.6	1.01	68.3	0.014	0.0463
7	0	56.4	0.878	71.1	0.011	0.0432
8	0	58.8	0.857	64.9	0.012	0.0432
1	90	62.8	1.01	70.7	0.013	0.0591
2	90	56.4	0.885	70.0	0.012	0.0536
3	90	59.4	0.990	73.7	0.013	0.0524
4	90	63.6	0.995	72.9	0.011	0.0646
5	90	54.6	0.927	74.5	0.012	0.0463
6	90	58.7	0.916	67.7	0.013	0.0420
7	90	63.2	1.09	77.1	0.013	0.0438
8	90	62.9	1.00	70.1	0.013	0.0445

The majority of the specimens failed laterally along the specimen where the tabs were bonded to the specimens. This was expected because there is a change of cross-section between the specimen gauge length and where the tabs are bonded, which results in a stress concentration. A failed tensile specimen can be seen in Figure 8.

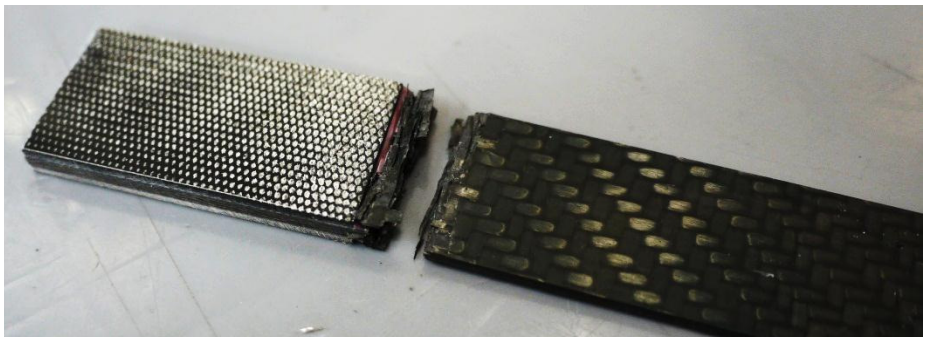

Figure 8: Typical Tensile Specimen Failure

All but one specimen failed in two places, where each tab was bonded. The failures at either end of the specimen gauge length seemed to happen simultaneously. A typical failed specimen can be seen in Figure 9.

Figure 9: Tensile Specimen Failure at Tabs

The average values, standard deviation, and coefficient of variation for each set of specimens were calculated. The results of these can be seen in Table 4 and Table 5.

Table 4: 0 Degree Tensile Specimen Statistics

	Average Value	Standard Deviation	Coefficient of Variation (%)
Tensile Strength (GPa)	0.916	0.0823	8.99
Tensile Modulus (GPa)	66.4	3.31	4.98
Tensile Strain	0.013	0.001	8.67
Poisson's Ratio	0.0448	0.004236	9.46

Table 5: 90 Degree Tensile Specimen Statistics

	Average Value	Standard Deviation	Coefficient of Variation (%)
Tensile Strength (GPa)	0.976	0.0642	6.57
Tensile Modulus (GPa)	72.1	3.00	4.16
Tensile Strain	0.012	0.001	6.15

In both the 0 degree specimens and the 90 degree specimens, the tensile modulus had the best coefficient of variation.

3.3 Compressive Properties

3.3.1 Testing

Compressive properties of a laminate can be difficult to achieve consistently. The current most popular method is ASTM D6641 Standard Test Method for Compressive Properties of Polymer Matrix Composite Materials Using a Combined Loading Compression (CLC) Test Fixture (Adams, 2005). However, the fixture required was unavailable at the time of testing and would be expensive to purchase or manufacture. Instead, a fixture was manufactured per the requirements in ASTM D695 Standard Test Method for Compressive Properties of Rigid Plastics. This test method also recommends a "compression tool" to be used to apply the load to the specimen. However, this would again increase the cost of testing so instead the fixture was placed directly in the Instron machine. All compression testing was performed per ASTM D695. Through this compression testing method, the ultimate compressive strength of the material was found. All tests were performed at room temperature. Sixteen specimens were made in total. The specimens were made by laminating a single panel and then water-jet cutting the profile of each specimen. Eight of the specimens had all plies oriented with the zero degree direction parallel to the axis of loading. These will be referred to as the "0 degree compression" specimens. The remaining eight specimens had all plies oriented with the zero direction perpendicular to the loading direction. These will be referred to as the "90 degree compression" specimens. Each specimen had 16 plies oriented as described above which resulted in a nominal thickness of 3.76 mm and the profile used was defined in the specification (ASTM Standard D695, 2010). Figure 10 shows a typical compression specimen. A drawing of the specimen profile can be seen in Figure C-10. The actual cross-sectional dimensions of each specimen, measured with callipers, can be seen in Table 6. The fixture used to support the specimen during testing can be seen in Figure 11.

Figure 10: Compression Specimen

Table 6: Compression Specimen Dimensions

Specimen Number	Type	Width (mm)	Thickness (mm)	Cross-sectional Area (mm^2)
1	0	12.82	3.45	44.23
2	0	12.77	3.41	43.55
3	0	12.72	3.23	41.09
4	0	12.81	3.56	45.60
5	0	12.8	3.56	45.57
6	0	12.83	3.57	45.80
7	0	12.79	3.54	45.28
8	0	12.8	3.53	45.18
1	90	12.84	3.49	44.81
2	90	12.74	3.43	43.70
3	90	12.87	3.54	45.56
4	90	12.82	3.46	44.36
5	90	12.83	3.47	44.52
6	90	12.82	3.48	44.61
7	90	12.84	3.48	44.68
8	90	12.74	3.48	44.34

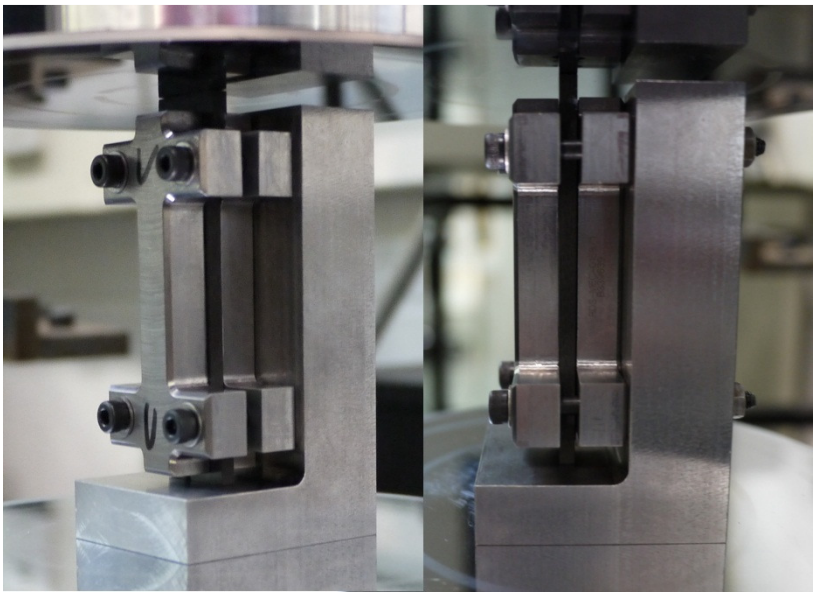

Figure 11: Compression Testing Jig

Each specimen was testing using a 200 kN Instron machine, model 5582 (Figure 5). The specimens were held in the compression jig which sat on flat platens fixed to the Instron machine (Figure 11).

The speed of testing was set at 1.3 $\frac{mm}{min}$ and each specimen was tested to failure. The load in kN and extension in mm from the Instron machine were recorded at 500 Hz during each test.

3.3.2 Results

The compressive strength for each specimen was calculated by dividing the load at failure by the cross-sectional area of the specimen (Equation 1). The results from each test can be seen in Table 7. Graphs of the test data can be seen in Appendix A.

Table 7: Compression Specimen Results

Specimen Number	Type	Maximum Load (kN)	Compressive Strength (GPa)
1	0	24.6	0.557
2	0	24.8	0.570
3	0	25.9	0.631
4	0	25.1	0.551
5	0	24.8	0.543
6	0	25.6	0.559
7	0	24.6	0.544
8	0	23.6	0.523
1	90	24.4	0.544
2	90	24.6	0.564
3	90	26.6	0.583
4	90	21.8	0.492
5	90	25.1	0.565
6	90	24.7	0.553
7	90	24.1	0.540
8	90	25.5	0.576

All specimens, except for 90 degree specimen 7, failed at the point where the cross-section of the specimen necks down. This was expected because there is a change of cross-section in this area. The 90 degree specimen 7 failed at the base of the specimen.

The average values, standard deviation, and coefficient of variation for each set of specimens were calculated. The results of these can be seen in Table 8 and Table 9.

Table 8: 0 degree Compression Specimen Statistics

	Average Value	Standard Deviation	Coefficient of Variation (%)
Compressive Strength (GPa)	0.560	0.0321	5.73

Table 9: 90 degree Compression Specimen Statistics

	Average Value	Standard Deviation	Coefficient of Variation (%)
Compressive Strength (GPa)	0.552	0.0284	5.14

The coefficients of variation from the compression testing results are comparable to the coefficients of variation obtained from the tensile testing.

3.4 Shear Properties

3.4.1 Testing

Shear testing was performed per ASTM D5379 Standard Test Method for Shear Properties of Composite Materials by the V-Notched Beam Method. Through shear testing, the ultimate shear strength and the shear modulus of the material were found. All tests were performed at room temperature. Eight specimens were made in total. The specimens were made by laminating a single panel and then water-jet cutting the profile of each specimen. Each specimen had 16 plies, with a ply schedule of $[0,90]_{4s}$, which resulted in a nominal thickness of 3.76 mm. A drawing of the specimen profile can be seen in Figure C-11. The actual cross-sectional dimensions of each specimen, measured with callipers, can be seen in Table 10. A jig was used to restrain the specimen during testing. A typical specimen fixed in the jig can be seen in Figure 12.

Table 10: Shear Specimen Dimensions

Specimen Number	Width (mm)	Thickness (mm)	Cross-sectional Area (mm^2)
1	12.38	3.19	39.5
2	12.42	3.36	41.7
3	12.44	3.44	42.8
4	12.37	3.58	44.3
5	12.4	3.59	44.5
6	12.41	3.57	44.3
7	12.4	3.44	42.7
8	12.38	3.23	40.0

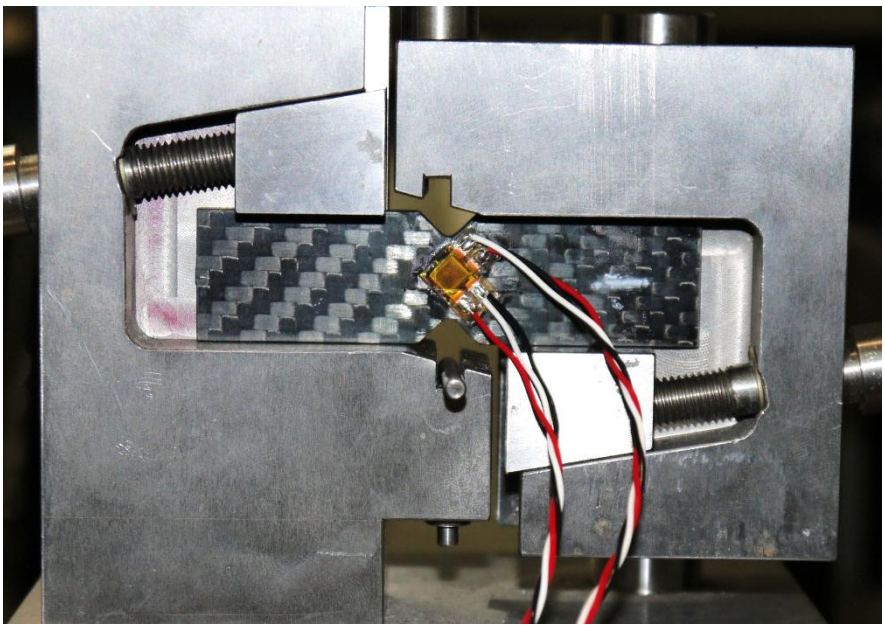

Figure 12: Shear Specimen in Test Jig

Each specimen had a 90 degree tee rosette strain gauge bonded to its surface in order to measure the shear modulus, similar to the tensile specimens. The 90 degree tee rosette was oriented on each specimen so that the sensing axis of gauge 1 is at a 45 degree angle to the loading axis and on the centreline of the specimen. The sensing axis of gauge 2 is perpendicular to that of gauge 1.

The gauge length of each strain gauge was 3.18 mm with a normal strain range of ±3%. The part number of the strain gauges is CEA-06-125WT-350. As with the tensile specimens, the measurements from the strain gauges on the shear specimens will need to be corrected for transverse sensitivity, which is described in Appendix B.

Each specimen was tested using a 200 kN Instron machine, model 5582 (Figure 5). The speed of testing was set at 1.5 $\frac{mm}{min}$. Each specimen was tested until the specimen deflected to the point where the lower right-hand side of the notch on the specimen came into contact with the jig. It is typical for the specimen to come in contact with the jig towards the end of the test as shown in Figure 13, where it is referred to on the graph as “fixture bottoms out,” meaning

that there is no more travel left in the jig. A specimen in contact with the jig can be seen in Figure 14.

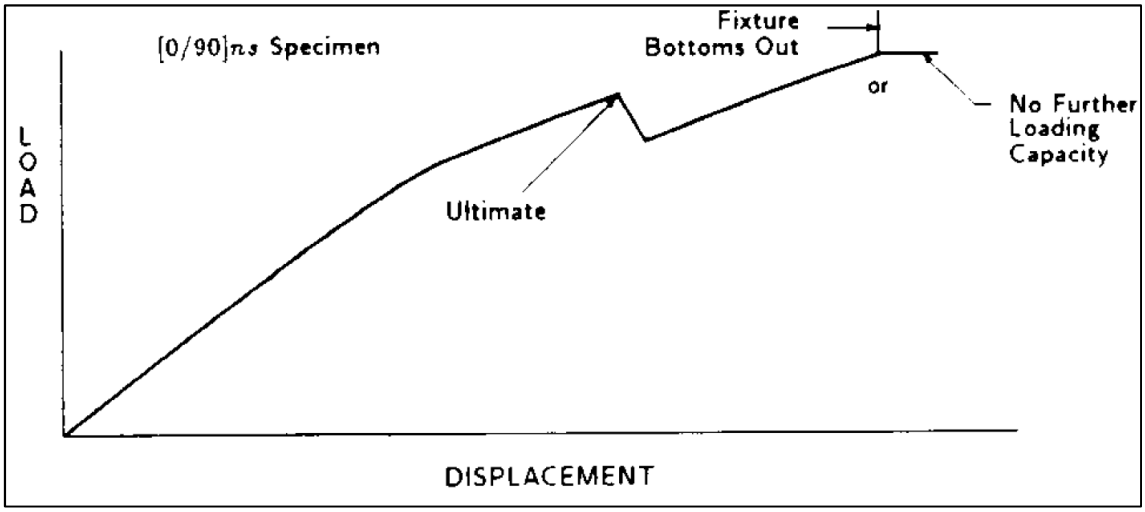

Figure 13: Typical Shear Test Data - Load versus Displacement Graph

Source (ASTM Standard D5379/D5379M, 2005, p. 4)

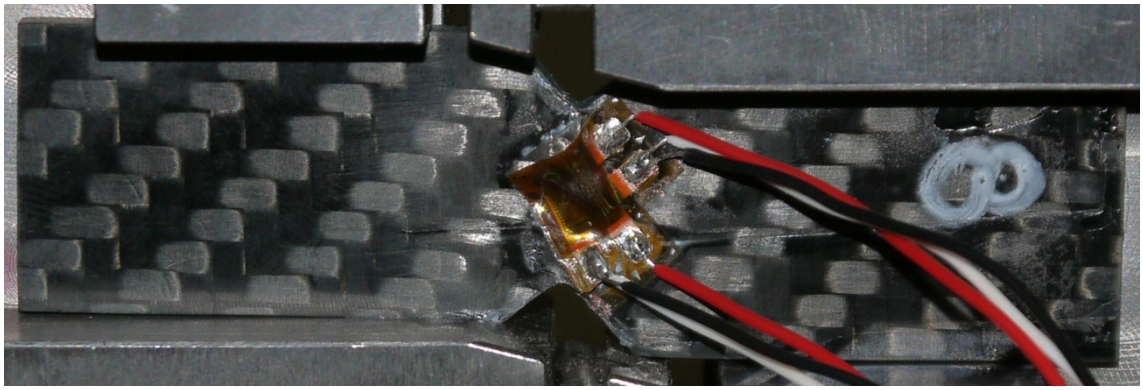

Figure 14: Failed Shear Specimen Contacting Jig

It can be seen in Figure 14 that the lower right-hand side of the notch has come in contact with the jig and the strain gauge has delaminated from the specimen surface. The strain in microstrain ($\mu\varepsilon$) from each gauge and the load in kilonewtons (kN) from the Instron machine were recorded at 200 Hz during each test.

3.4.2 Results

The shear strength for each specimen was calculated by dividing the load at failure by the cross-sectional area of the specimen at the notch (Equation 1). The shear strain at each data point was calculated by summing the absolute value of the readings from each strain gauge (Equation 4).

$$\gamma = |\varepsilon_{+45}| + |\varepsilon_{-45}| \qquad \textbf{Equation 4}$$

The results from the test can be seen in Table 11. Graphs of the test data can be seen in Appendix A.

Table 11: Shear Specimen Results

Specimen Number	Max Load (kN)	Shear Stress (GPa)	Shear Modulus (GPa)	Shear Strain
1	5.1	0.129	5.60	0.05
2	5.7	0.137	5.27	0.05
3	5.9	0.138	5.21	0.05
4	6.0	0.135	5.34	0.05
5	6.1	0.136	5.28	0.05
6	6.0	0.136	5.20	0.05
7	5.8	0.135	5.62	0.05
8	5.3	0.133	5.65	0.05

The peak load for each specimen was difficult to define because most of the specimens reached a peak immediately before coming into contact with the jig. For each test, the peak load was assumed to be the maximum load that occurred before the specimen came in contact with the jig and created a sharp rise in load. An example of this can be seen in Figure 15. The lack of a clearly defined peak load will affect the accuracy of the maximum shear strength.

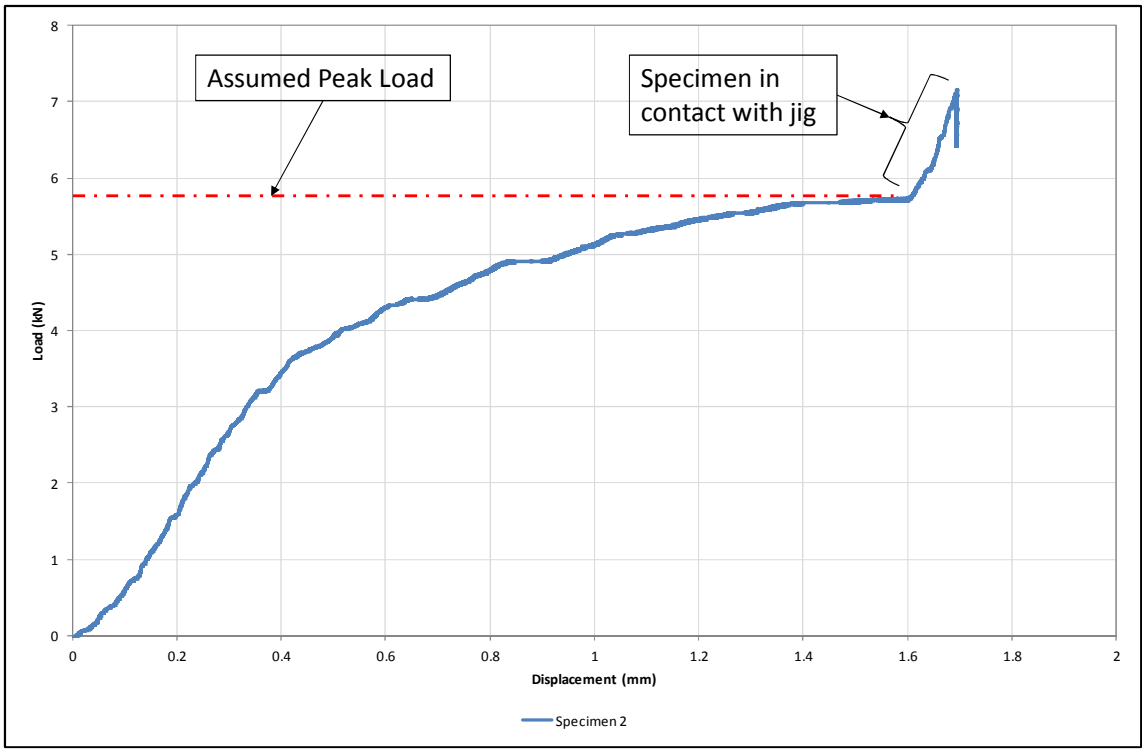

Figure 15: Assumed Peak Load Location for Shear Specimens

For each shear test, there were visible ply failures but the specimens did not break into two separate pieces. This type of failure mode is acceptable as outlined in ASTM D5379 (Figure 16).

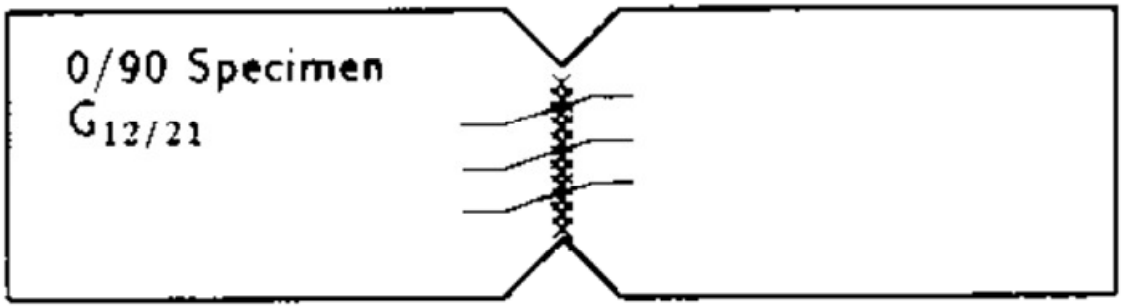

Figure 16: Typical Acceptable Failure Mode for 0/90 Shear Specimens

Source (ASTM Standard D5379/D5379M, 2005, p. 10)

The maximum strain is defined as the strain at the maximum load or 5% strain, whichever is smallest. For two of the specimens, the strain gauges dis-bonded from the surface of the specimen before they reached 5% strain. The gauges on the remaining specimens stopped reading when they reached 5% strain.

Therefore, the maximum strain was assumed to be 5%. Due to the peak load being difficult to find and having to assume the strain reached the maximum allowable per the test specification; care will be taken when using these values in the finite element analysis. The average values, standard deviation, and coefficient of variation for each of specimens were calculated. The results can be seen in Table 12.

Table 12: Shear Specimen Statistics

	Average Value	Standard Deviation	Coefficient of Variation (%)
Shear Stress (GPa)	0.135	0.003	2.108
Shear Modulus (GPa)	5.394	0.193	3.576
Shear Strain	0.05	-	-

3.5 Material Testing Conclusion

A summary of the values found through testing and how they compare with the given values can be seen in Table 13.

Table 13: Material Properties Summary

Parameter		Given Value	Measured Value	Per cent Difference
ν_{12}		0.05	0.0448	-10%
Stiffness (GPa)	E_{11T}	64.6	66.4	3%
	E_{11C}	60.9	-	-
	E_{22T}	64.6	72.1	12%
	E_{22C}	64.4	-	-
	G_{12}	3.57	5.39	51%
	G_{23}	2.37	-	-
	G_{31}	2.37	-	-
Strength (MPa)	σ_{11T}	960	916	-5%
	σ_{11C}	607	560	-8%
	σ_{22T}	881	976	11%
	σ_{22C}	586	552	-6%
	τ_{12}	112	135	21%
	ILSS	77	-	-
Strain	ε_{11T}	-	0.013	-
	ε_{22T}	-	0.012	-
	ε_{12}	-	0.050	-

The properties found for the longitudinal direction were closer to the given values than the properties found for the transverse direction. It is interesting to note that testing shows the transverse direction has a higher tensile modulus and tensile strength than the longitudinal direction. It is common practice to assume that the longitudinal and transverse directions are equal for a balanced weave. The data shows that this might not be a valid assumption. However, the higher properties in the transverse direction could be a result of the relatively low number of specimens that were tested. More tests would have to be performed on both the longitudinal and the transverse directions to get a better statistical spread of data.

The test results for the compressive strengths in both the longitudinal and transverse directions matched well with the given data. The compressive

modulus could not be found through these tests because an extensometer was not used to measure the change of length of the specimen. It was attempted to use the Instron machine displacement to find the modulus; however, this resulted in a value that was 24% less than the given value and is not representative of what is happening with the material, therefore, it was not used in analysis. In order to find the compressive modulus an extensometer needs to be used that fits with the current fixture or a change of test method needs to be made to one that has an unsupported gauge length so a strain gauge or extensometer can be used.

There was a large discrepancy between the tested value for shear stress and the given value. During shear testing, all of the specimens eventually bottomed out on the fixture and for some data sets, it was difficult to find the maximum load. Even so, if the specimens had not bottomed out on the fixture, the loads could have been even higher, which would result in a larger discrepancy with the given value. The shear test standard, ASTM D5379, states that “the shear failure load may be lower than the maximum load attainable during the test” (2005). It is possible that this specific shear test does not work well with this material. Another reason for the discrepancy is the different test methods used. The test method used by Umeco for this shear value is unknown. The found shear modulus in the 1-2 plane was also much higher than the given value. Again, this could be from the same issues described above. The shear modulus in the 2-3 and 3-1 plane can be found using this same test method by manufacturing specimens with the stacking direction in the appropriate axis. However, the manufacturing of the specimens would take much longer because of the amount of plies needed in the stacking direction. Issues can arise when laminating that many plies at once and the test specification does not describe a method that works with all materials. This means that it would have to first be verified that a method of manufacturing would produce accurate, repeatable results. It was thus decided to not perform these tests.

4 LS-DYNA Material Models

The following section will go through the theory and single-element tests of a few of the most commonly used composite material models.

4.1 Single-element Test Approach

Single-element tests were performed with each material model in order to better understand the differences between each model. The approach used was similar to that used by Schweizerhof (1998).

The single-element tests consisted of one shell element with constraints and a constant velocity applied. Each shell element represented a cube with dimensions of 1 mm by 1 mm by 1 mm, therefore each side of the shell element was 1 mm and the thickness of each element was 1 mm. Each single-element was tested in tension, compression, and shear. For each loading scenario, a strain rate of 1 $\frac{1}{s}$ was chosen. This strain rate equates to a velocity of 1 x 10^{-3} $\frac{mm}{ms}$. For the tension test setup, nodes 1 and 2 have a constant velocity applied in the positive x-direction. Node 4 is restrained in the x-direction and node 3 is restrained in the x- and y-directions. A diagram of the tension test setup can be seen in Figure 17.

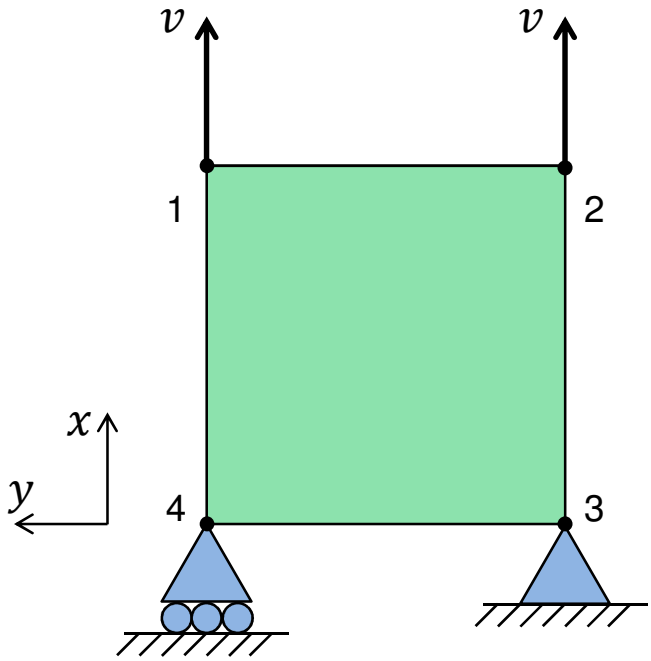

Figure 17: Single-element Tension Test

For the compression test setup, nodes 3 and 4 were restrained in the same fashion as the tension test. Nodes 1 and 2 were loaded with a constant velocity in the negative x-direction. This can be seen in Figure 18.

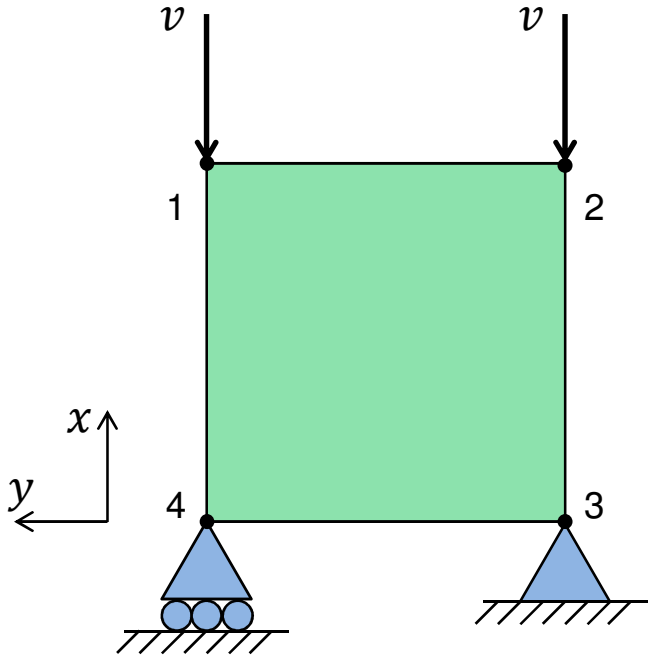

Figure 18: Single-element Compression Test

For the shear test setup, an additional constraint was applied to nodes 1 and 2. Nodes 1 and 2 were set to move together in the x-direction. This prevented the element from distorting in a way which caused node 1 to rotate around node 3, and placing the element in a mixed-mode loading scenario. The constant velocity was applied in the positive y-direction. A diagram for the shear test setup can be seen in Figure 19.

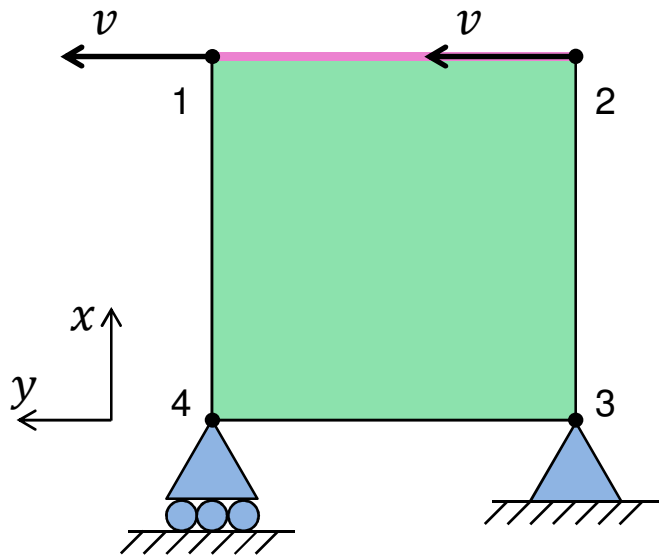

Figure 19: Single-element Shear Test

The tension, compression, and shear single-element tests were all done with two through-thickness points of integration because the loading in in-plane with the element. Each single-element test was repeated using material orientations of 0, 45, and 90 degrees, with respect to the global coordinate system.

4.2 Material Model 22

4.2.1 Theory

Material model 22 is a linear elastic failure model. The behaviour of an element is defined by the elastic modulus until the failure strength of the material is reached. Once failure is reached, the stress in the element is immediately reduced to zero. Material model 22 has three modes of failure based on the approaches described in (Chang and Chang, 1987a) and (Chang and Chang, 1987b). The LS-DYNA Theory Manual describes these failure modes as matrix

cracking, compression, and fibre breakage (Hallquist, 2006). The failure modes available depend on the input values of the tensile strength in the longitudinal (X_T) and transverse (Y_T) directions, the compressive strength in the transverse direction (Y_C), the shear strength (S_C), and a nonlinear shear stress parameter (α). Material model 22 does not have any inputs for a crashfront algorithm, which can define a softening of parameters for elements deemed to be within the crashfront.

Failure by matrix cracking is shown in Equation 5. Failure occurs when $F_{YT} > 1$.

$$F_{YT} = \left(\frac{\sigma_2}{Y_T}\right)^2 + \overline{\tau} \qquad \textbf{Equation 5}$$

Compressive failure is shown in Equation 6. Failure occurs when $F_{YC} > 1$.

$$F_{YC} = \left(\frac{\sigma_2}{2S_C}\right)^2 + \left[\left(\frac{Y_C}{2S_C}\right)^2 - 1\right]\frac{\sigma_2}{Y_T} + \overline{\tau} \qquad \textbf{Equation 6}$$

Failure by fibre breakage is shown in Equation 7. Failure occurs when $F_{XT} > 1$.

$$F_{XT} = \left(\frac{\sigma_1}{X_T}\right)^2 + \overline{\tau} \qquad \textbf{Equation 7}$$

In the above equations, a fibre matrix shearing term, $\overline{\tau}$, is used. This is defined as shown in Equation 8.

$$\overline{\tau} = \frac{\frac{\tau_{12}^2}{2G} + \frac{3}{4}\alpha\tau_{12}^4}{\frac{S_C^2}{2G} + \frac{3}{4}\alpha S_C^4} \qquad \textbf{Equation 8}$$

G is the shear modulus in the 1-2 plane. All equations listed are taken from the LS-DYNA Theory Manual (Hallquist, 2006).

4.2.2 Single Element Tests

Single-element tests as described in Section 4.1 were done with Material Model 22. The results for tension, compression, and shear can be seen in Figure 20, Figure 21, and Figure 22, respectively.

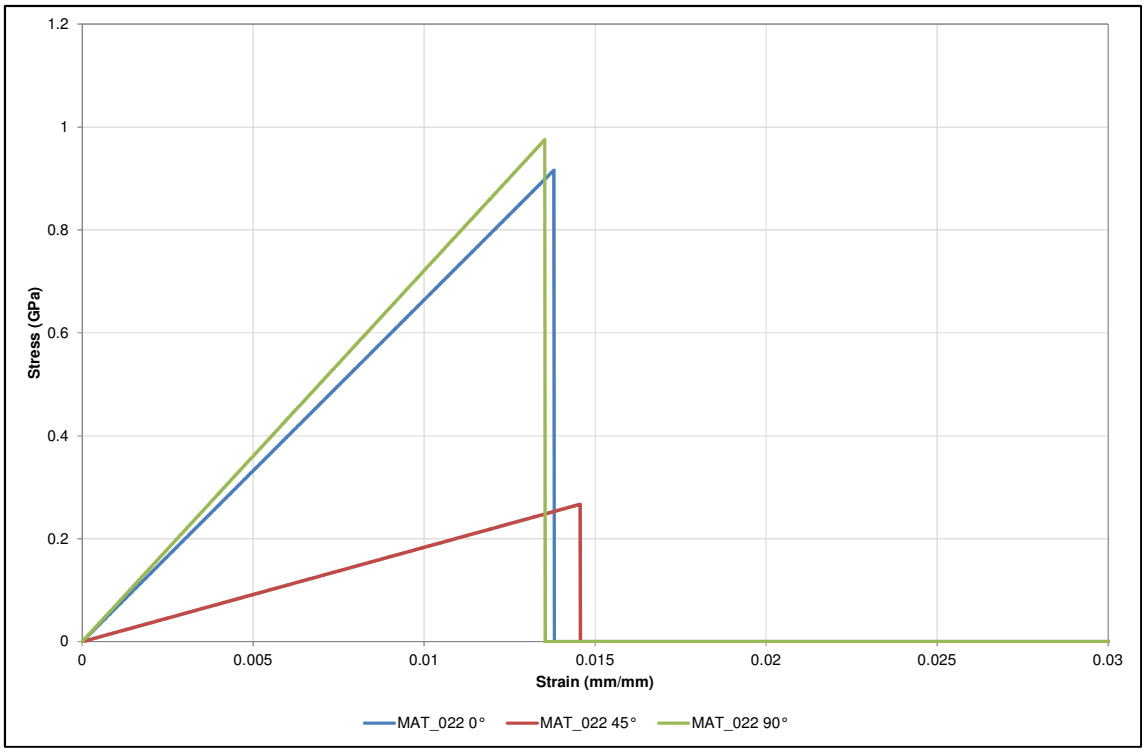

Figure 20: Single Element MAT_022 Tension

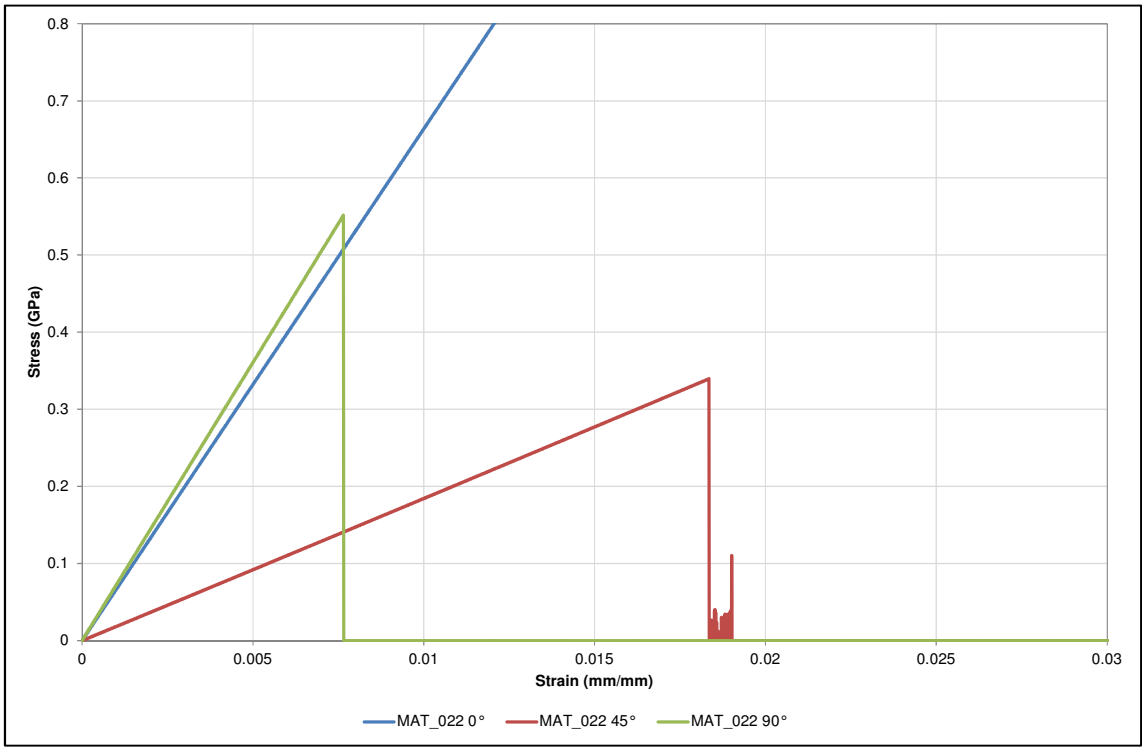

Figure 21: Single Element MAT_022 Compression

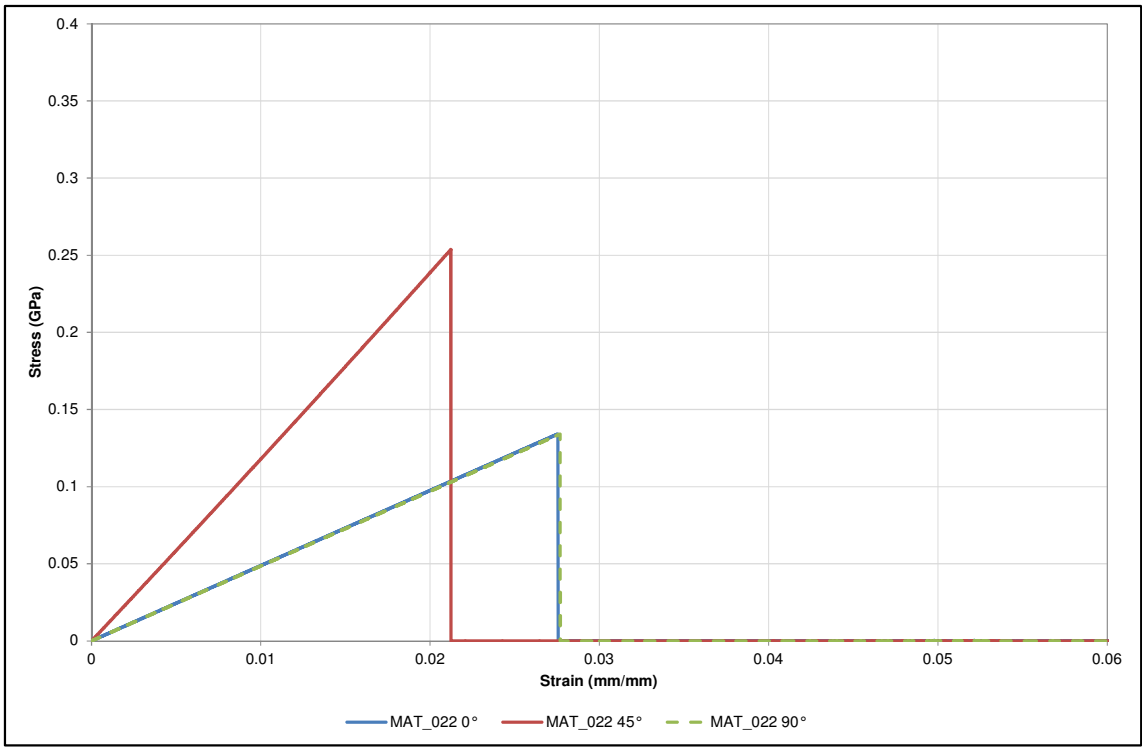

Figure 22: Single Element MAT_022 Shear

A summary of the results from the single element test of material model 22 can be seen in Table 14. The values from LS-DYNA were compared with the values entered on the material card.

Table 14: MAT_022 Single Element Results

	LS-DYNA Value	Material Card	Per cent Difference
Tensile Stress 0° (GPa)	0.916	0.916	-0.01%
Tensile Stress 90° (GPa)	0.975	0.976	-0.06%
Compressive Stress 0° (GPa)	-	0.560	-
Compressive Stress 90° (GPa)	0.552	0.552	-0.08%
Shear Stress 0° (GPa)	0.134	0.135	-0.61%
Shear Stress 90° (GPa)	0.134	0.135	-0.70%

The values from the simulations align well with values entered on the material model. As expected, there is no compressive failure in the 0° direction because the material card does not require it.

4.3 Material Models 54 and 55

4.3.1 Theory

Material models 54 and 55 are based on material model 22. Material model 54 and 55 are linear elastic models. Material models 54 and 55 can be used as either failure or damage models. The behaviour of an element is defined by the elastic modulus until the failure strength of the material is reached. Once the failure strength is reached, the stress in the element can be immediately reduced to zero, or the stress in the element will stay at a value defined in the material parameters. The definition for failure in the matrix for material model 54 is the same as material model 22, as described in (Chang and Chang, 1987a) and (Chang and Chang, 1987b). Failure in the matrix for material model 55 is taken from (Tsai and Wu, 1971). Material model 54 has more options for failure definition such as maximum strain in the matrix, maximum shear strain, maximum strain for fibre tension, maximum strain for fibre compression, and effective failure strain. The failure criteria for material model 54 are as follows.

Failure will occur in tension in the fibres if $F_{XT}^2 \geq 0$ in Equation 9. When $\beta = 1$, the equation becomes the original equation as defined by Hashin (1980).

$$F_{XT}^2 = \left(\frac{\sigma_1}{X_T}\right)^2 + \beta\left(\frac{\tau_{12}}{S_C}\right) - 1 \qquad \textbf{Equation 9}$$

Failure in compression of the fibres occurs when $F_{XC}^2 \geq 0$, as shown in Equation 10.

$$F_{XC}^2 = \left(\frac{\sigma_1}{X_C}\right)^2 - 1 \qquad \textbf{Equation 10}$$

Failure of the matrix in tension occurs when $F_{YT}^2 \geq 0$, as shown in Equation 11.

$$F_{YT}^2 = \left(\frac{\sigma_2}{Y_T}\right)^2 + \left(\frac{\tau_{12}}{S_C}\right)^2 - 1 \qquad \textbf{Equation 11}$$

Failure in compression of the matrix is defined as $F_{YC}^2 \geq 0$, as shown in Equation 12.

$$F_{YC}^2 = \left(\frac{\sigma_2}{2S_C}\right)^2 + \left[\left(\frac{Y_C}{2S_C}\right)^2 - 1\right]\left(\frac{\sigma_2}{Y_C}\right) + \left(\frac{\tau_{12}}{S_C}\right)^2 - 1 \qquad \textbf{Equation 12}$$

Material model 55 has the same failure criteria in tension and compression of the fibres as material model 54 (Equation 9 and Equation 10).The failure in tension and compression of the matrix is combined into one equation with failure defined when $F_{YTC}^2 \geq 0$, as shown in Equation 13.

$$F_{YTC}^2 = \left(\frac{\sigma_2}{Y_C Y_T}\right)^2 + \left(\frac{\tau_{12}}{S_C}\right)^2 + \left(\frac{(Y_C - Y_T)\sigma_2}{Y_C Y_T}\right) - 1 \qquad \textbf{Equation 13}$$

All equations listed are taken from the LS-DYNA Theory Manual (Hallquist, 2006).

Element deletion for both material models is defined by TFAIL, which defines the minimum time-step size of an element. After the minimum time-step size is reached, the element is deleted. Both material models will use a crashfront algorithm when TFAIL is greater than zero. The first parameter needed for the crashfront algorithm is SOFT. SOFT is the value that the material strength will be reduced by if an element becomes a crashfront element. An element is

considered to be in the crashfront if a neighbouring element has been deleted. Material model 54 has additional controls that can be applied to the crashfront elements such as softening of fibre tensile strength, softening of compressive fibre strength after matrix compressive failure, and the number of layers that must fail before the crashfront algorithm is initiated. This last parameter enables elements to be considered part of the crashfront earlier because usually all integration points must fail. Parameters defining the crashfront were not used for the single element tests.

4.3.2 Single Element Tests

Single-element tests as described in Section 4.1 were done with Material Model 54 and Material Model 55. The results for each test can be seen in the following figures.

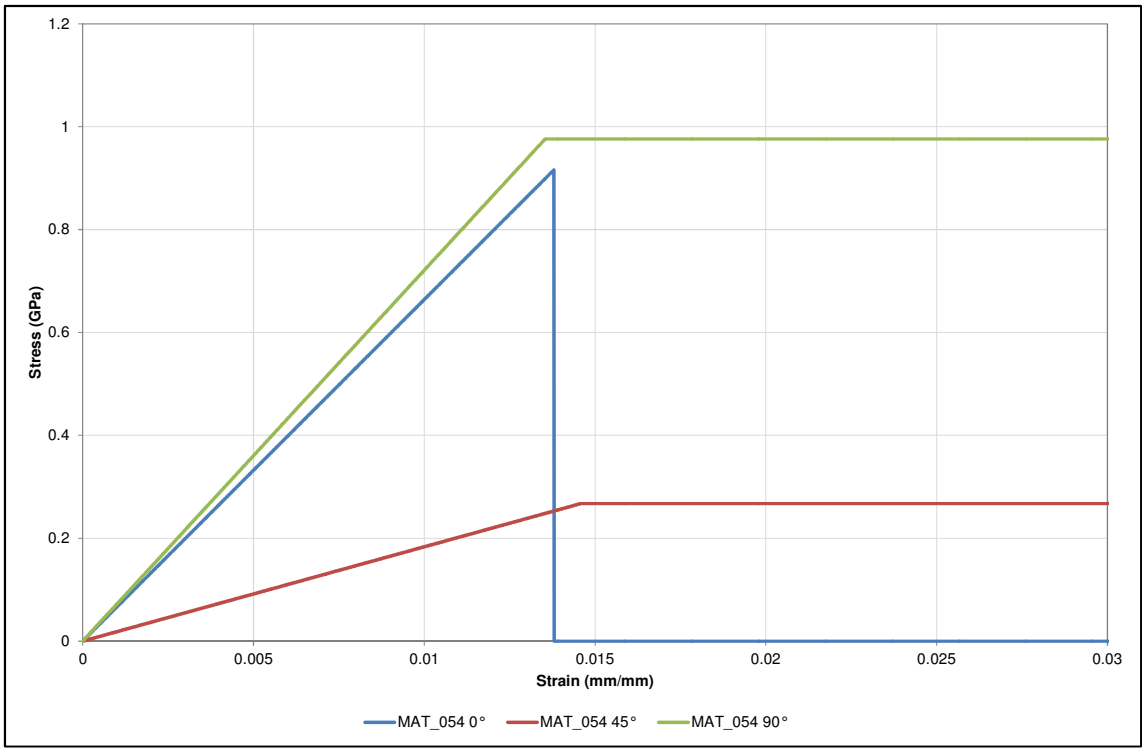

Figure 23: Single Element MAT_054 Tension

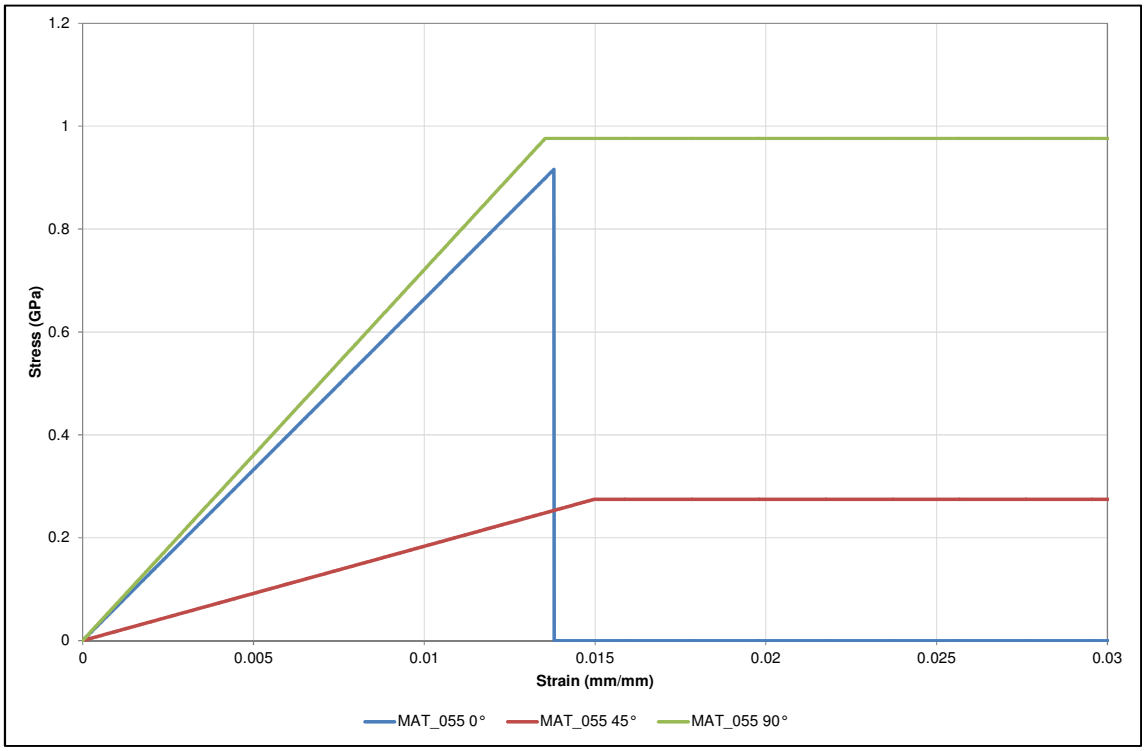

Figure 24: Single Element MAT_055 Tension

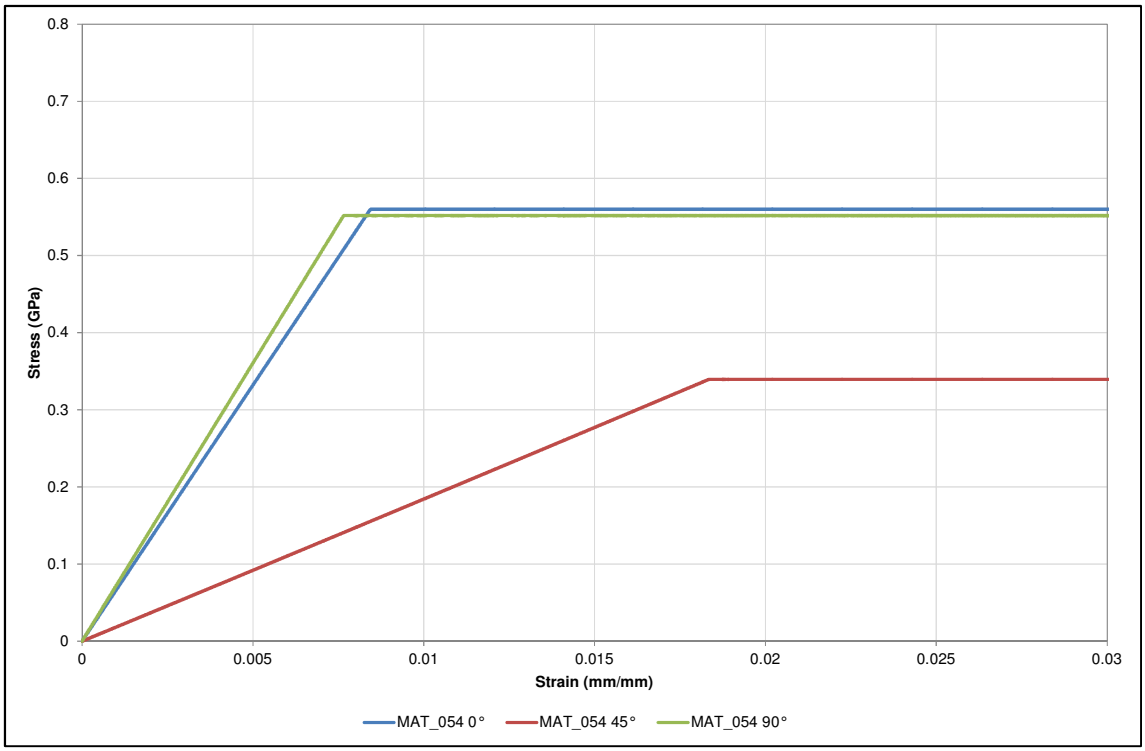

Figure 25: Single Element MAT_054 Compression

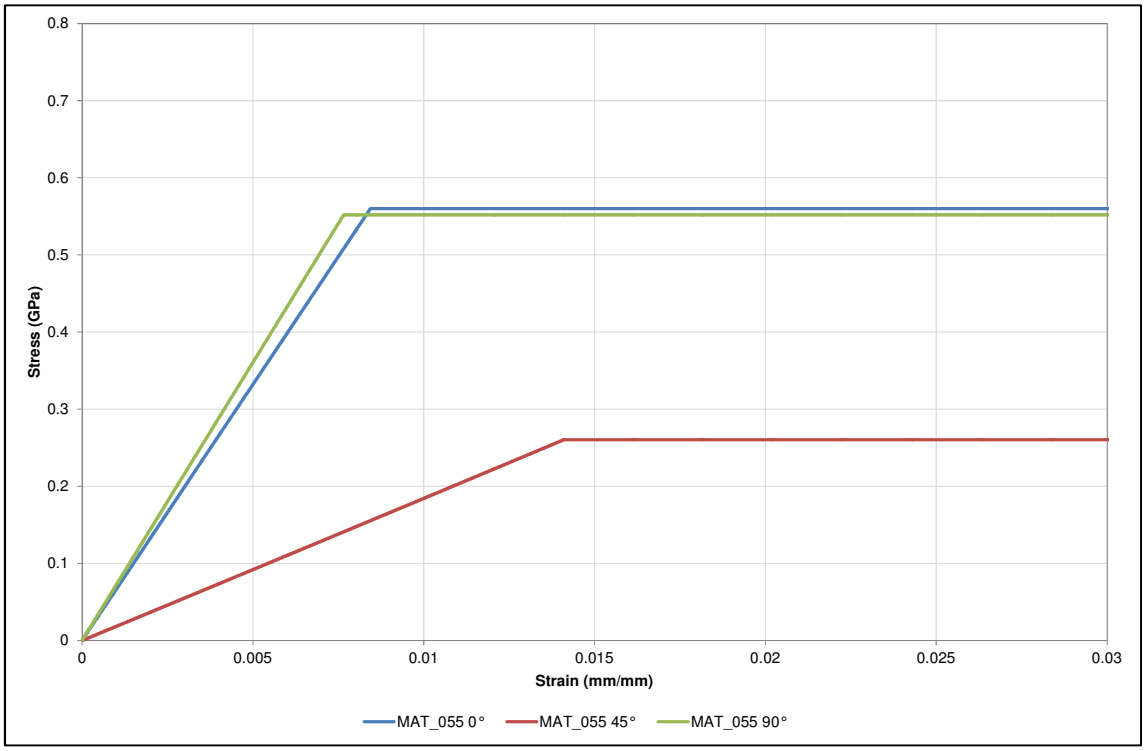

Figure 26: Single Element MAT_055 Compression

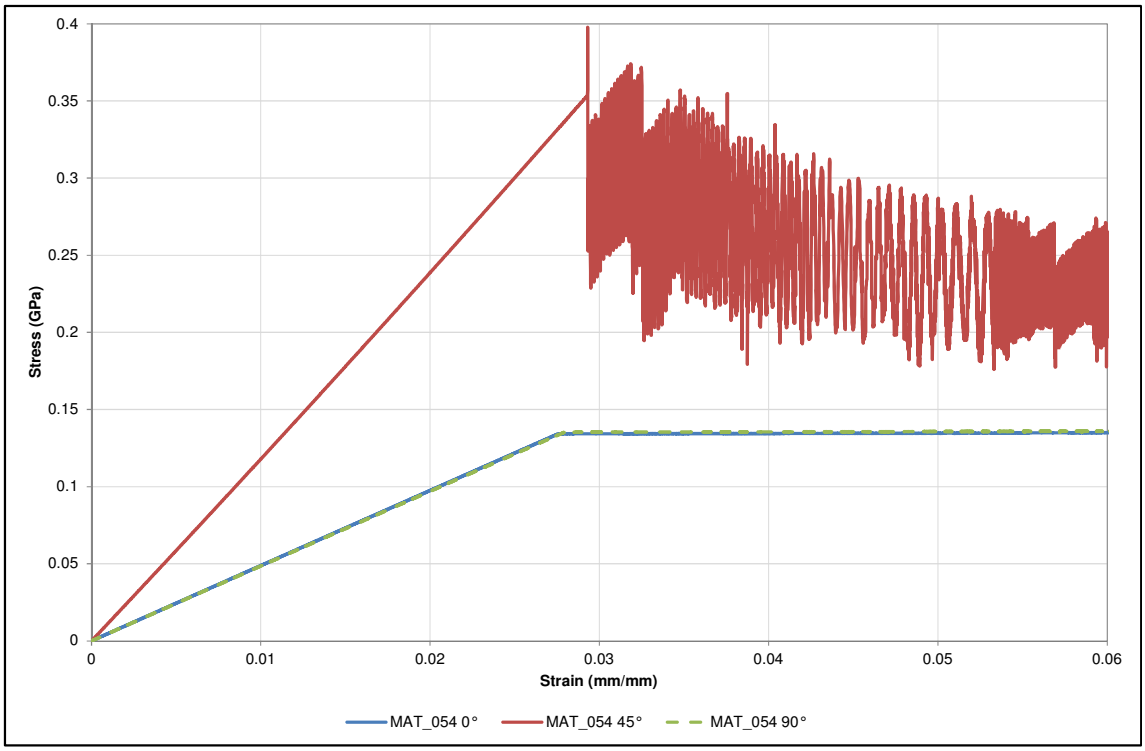

Figure 27: Single Element MAT_054 Shear

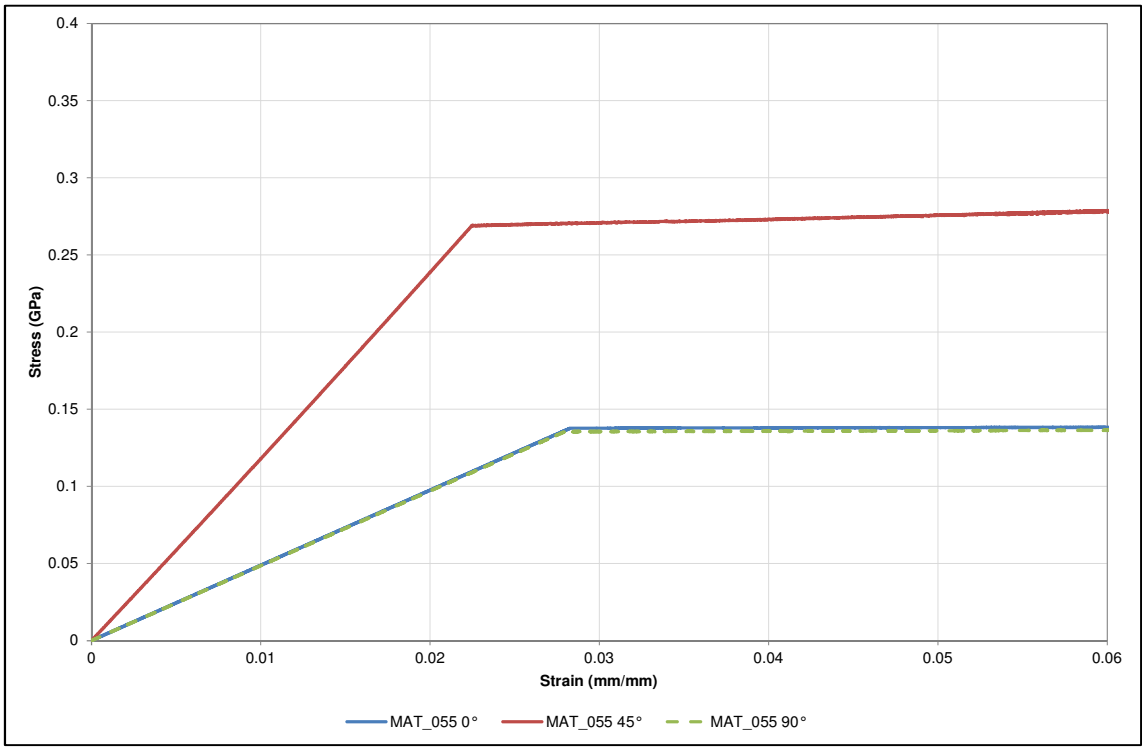

Figure 28: Single Element MAT_055 Shear

A summary of the results from the single element tests of material models 054 and 055 can be seen in Table 15 and Table 16. The values from LS-DYNA were compared with the values entered on the material card.

Table 15: Material Model _054 Single Element Results

	LS-DYNA Value	Material Card	Per cent Difference
Tensile Stress 0° (GPa)	0.916	0.916	-0.01%
Tensile Stress 90° (GPa)	0.976	0.976	0.00%
Compressive Stress 0° (GPa)	0.560	0.56	0.00%
Compressive Stress 90° (GPa)	0.552	0.552	0.00%
Shear Stress 0° (GPa)	0.146	0.135	8.51%
Shear Stress 90° (GPa)	0.146	0.135	8.20%

The majority of the values from the material model 054 simulations align well with the values entered on the material card. The shear stress in the 0° and 90° do not match as well as they did with material model 022.

Table 16: Material Model_055 Single Element Results

	LS-DYNA Value	Material Card	Per cent Difference
Tensile Stress 0° (GPa)	0.916	0.916	-0.01%
Tensile Stress 90° (GPa)	0.976	0.976	0.00%
Compressive Stress 0° (GPa)	0.560	0.56	0.00%
Compressive Stress 90° (GPa)	0.552	0.552	0.03%
Shear Stress 0° (GPa)	0.149	0.135	10.34%
Shear Stress 90° (GPa)	0.148	0.135	9.36%

Similar results were obtained with material model 055. Everything but the shear stress values matched well with the values entered on the material card. The shear stress values were slightly worse than material model 054.

4.4 Material Models 58 and 158

4.4.1 Theory

The LS-DYNA manuals offer limited information as to what is happening with material model 58. An explanation of this material model as incorporated in LS-DYNA is best described by Schweizerhof (1998). The underlying theory is gone into further detail in (Matzenmiller et al., 1995). Material model 58 is similar to material model 54 in that they are both derived from (Hashin, 1980). Material model 58 is a linear elastic damage model and material model 158 is a viscoelastic damage model. For both of the models, the behaviour of an element is defined by the elastic modulus until the damage threshold of the material is reached. The stress of the element then goes through a nonlinear smooth transition of damage. In a damage model, when the maximum strength of the material is reached, the stress in the element does not immediately drop to zero as it does for a failure model. The stress in a failed element of a damage model drops off at a defined rate. Equation 14 and Equation 15 describe the failure in the fibre and in the matrix, respectively.

$$F_{fibre} = \frac{\sigma_1^2}{\left(1-\omega_{1\,C,T}\right)^2 X_{C,T}^2} - r_{fibre\,C,T} = 0 \qquad \textbf{Equation 14}$$

$$F_{matrix} = \frac{\sigma_2^2}{\left(1-\omega_{2\,C,T}\right)^2 Y_{C,T}^2} + \frac{\tau_{12}^2}{(1-\omega_{12})^2 S_C^2} - r_{matrix\,C,T} = 0 \qquad \textbf{Equation 15}$$

r is a strain damage threshold that dictates the size of the elastic region. ω describes the damage evolution law used in this material model. Before the maximum strength is met, ω is defined by Equation 16.

$$\omega = 1 - exp\left[-\frac{1}{m_i e}\left(\frac{\varepsilon_i}{\varepsilon_f}\right)^{m_i}\right] \qquad \textbf{Equation 16}$$

m_i is a parameter that relates developing failure modes to the strains. ε_f is the nominal failure strain while ε_i represents either the strain in the longitudinal or

transverse directions. After the maximum strength is reached, ω is calculated using Equation 17.

$$\omega = 1 - \frac{\alpha X_{C,T}}{E\varepsilon} \qquad \textbf{Equation 17}$$

α is a coefficient with a value between zero and one that defines a yield-stress from the strength value. It should be noted that this α is different than the α used in material model 22, which is a parameter for the nonlinear shear stress in Equation 8.

The combination of Equation 14 and Equation 15 define behaviour for unidirectional materials only. For a fabric prepreg, the failure modes in both directions are taken to be the same and are defined by Equation 18 and Equation 15.

$$F_{fibre} = \frac{\sigma_1^2}{\left(1 - \omega_{1\,C,T}\right)^2 X_{C,T}^2} + \frac{\tau_{12}^2}{(1 - \omega_{12})^2 S_C^2} - r_{fibre\,C,T} = 0 \qquad \textbf{Equation 18}$$

In order to invoke the smooth fabric failure surface, FS must be set to 1 in the material card. The smooth failure surface for unidirectional materials is obtained when FS is set to 0. The prepreg that is under investigation is a woven fabric so the smooth fabric failure surface will be used. All equations listed are taken from the LS-DYNA Theory Manual (Hallquist, 2006).

Material model 158 is the rate-sensitive version of material model 58. Material model 158 applies a viscous stress tensor over the stress tensor. This model achieves that by using a Maxwell model which consists of a damper and spring in series (Hallquist, 2006). Although the user inputs for this model are limited, it is of interest because the strain rate sensitivity of a prepreg greatly affects the outcome of an impact test.

4.4.2 Single Element Tests

Single-element tests as described in Section 4.1 were done with Material Model 58 and Material Model 158. The results for each test can be seen in the following figures.

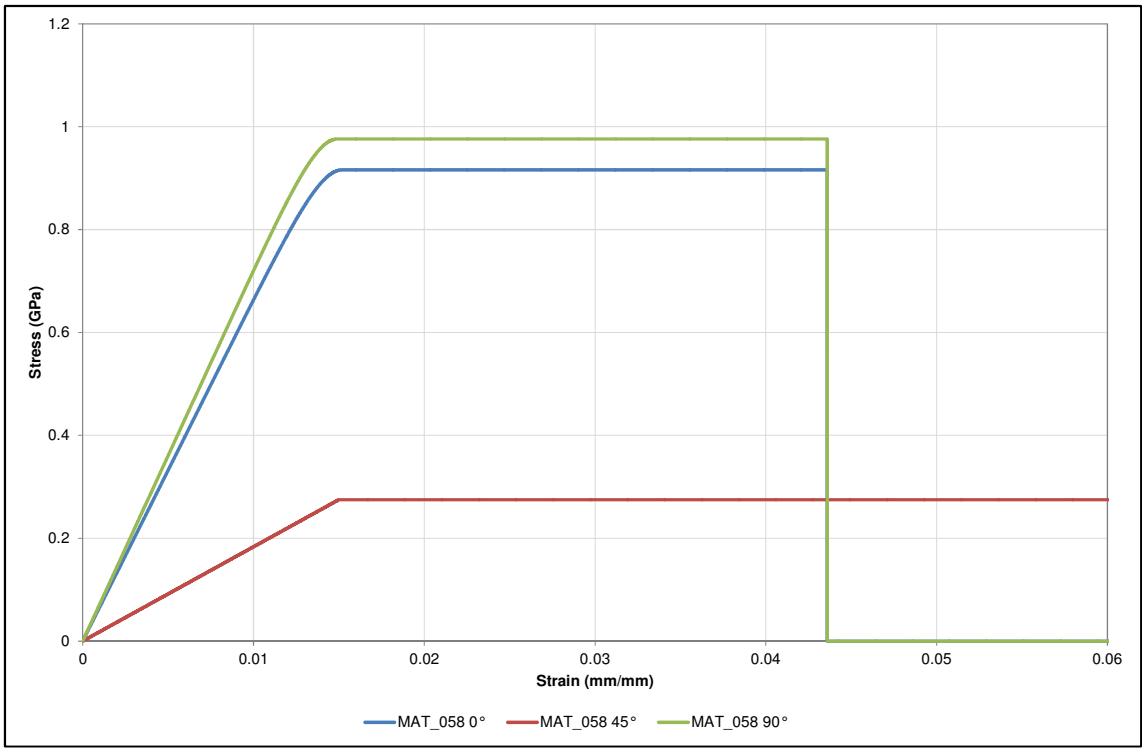

Figure 29: Single Element MAT_058 Tension

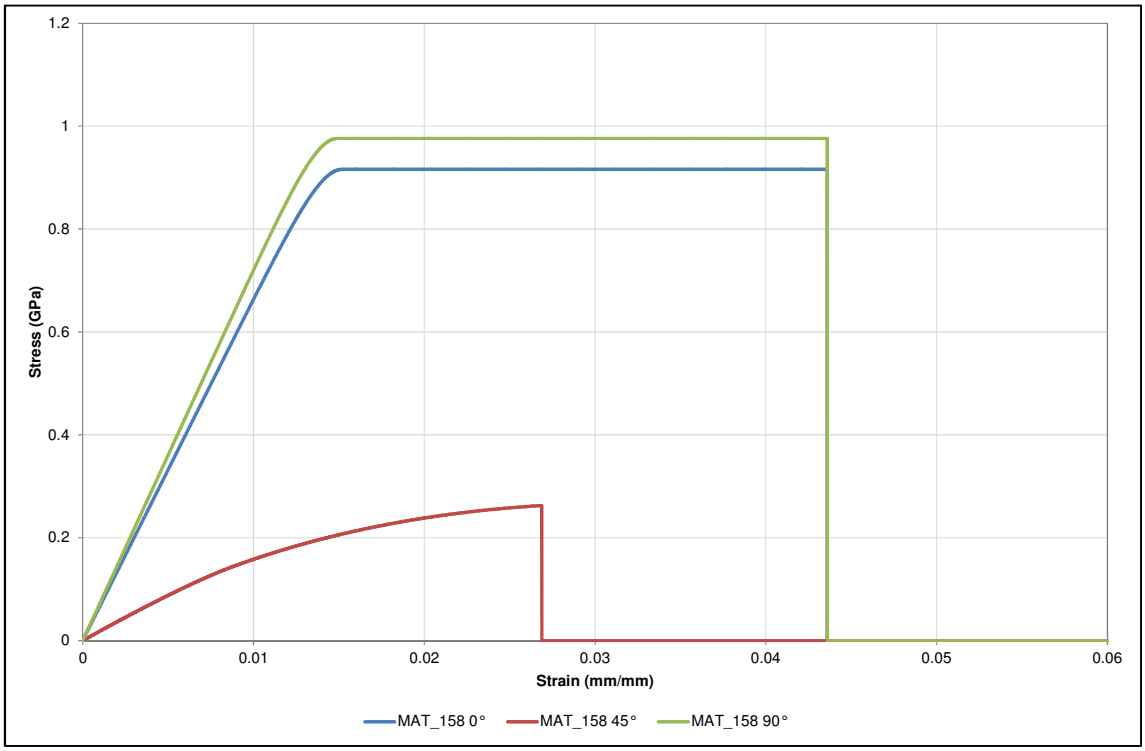

Figure 30: Single Element MAT_158 Tension

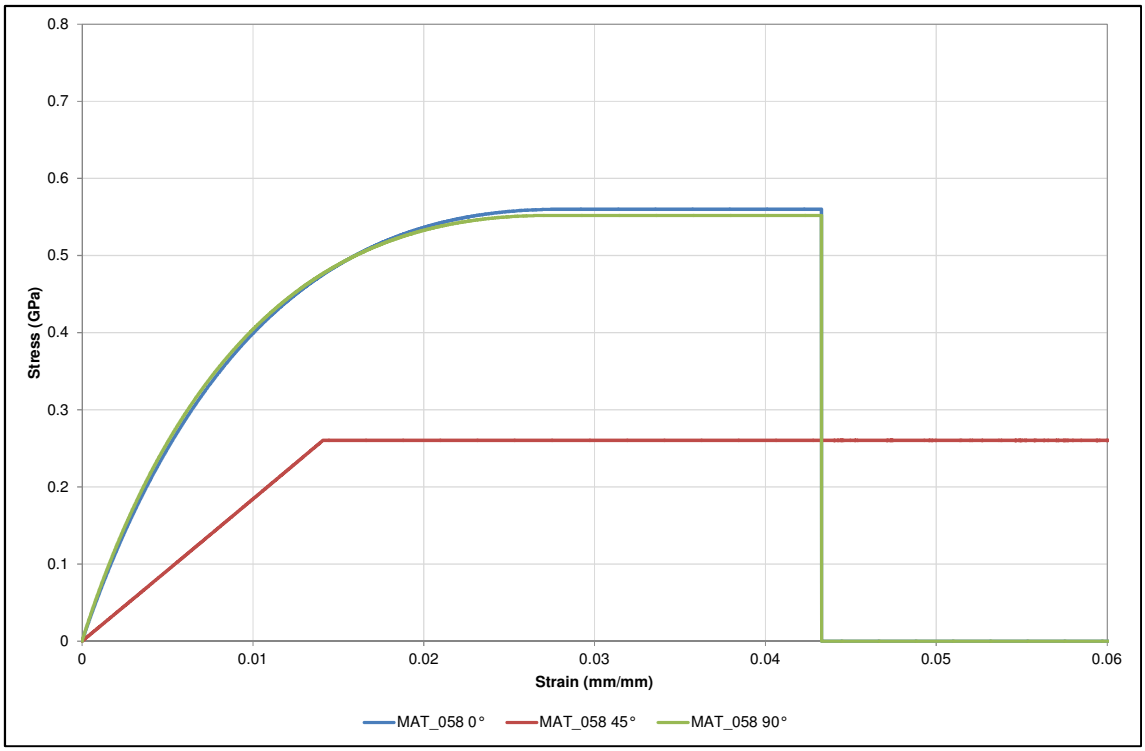

Figure 31: Single Element MAT_058 Compression

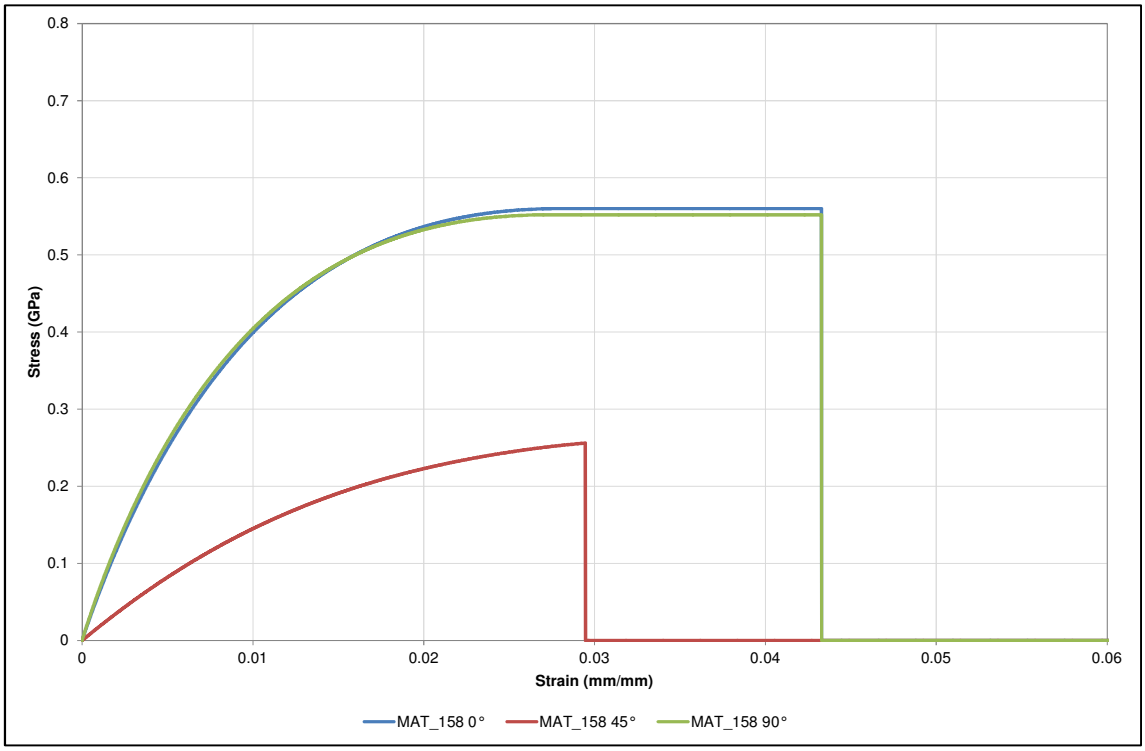

Figure 32: Single Element MAT_158 Compression

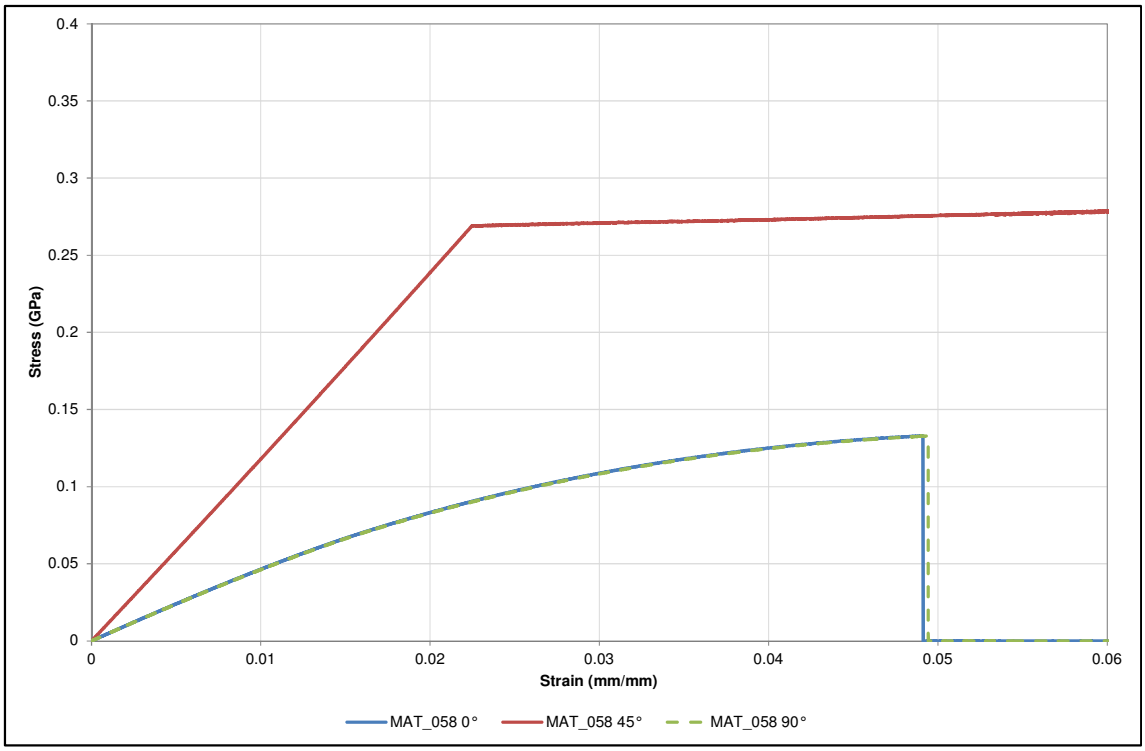

Figure 33: Single Element MAT_058 Shear

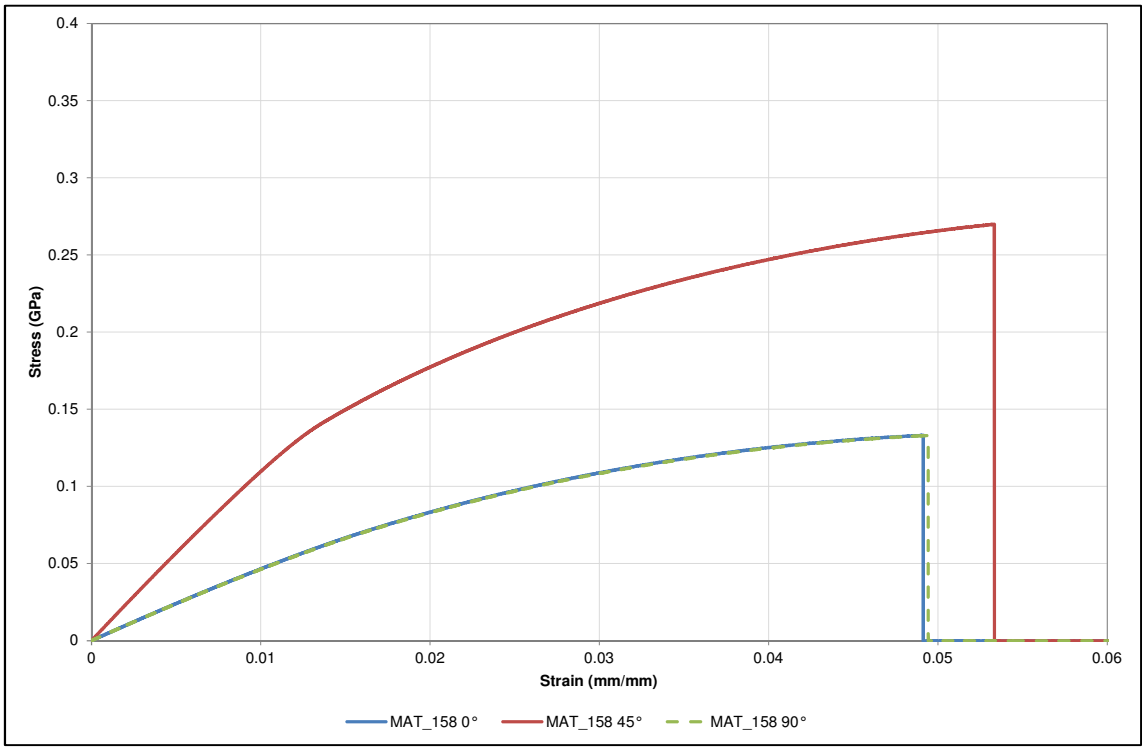

Figure 34: Single Element MAT_158 Shear

The nonlinearity that occurs in the results of material models 058 and 158 is a result of the damage that is inherent in these material models. The parameter m_i in Equation 16 dictates the amount of nonlinearity. However, this is not a parameter that can be adjusted using the LS-DYNA input cards for these material models, so the value of m_i is fixed.

A summary of the results from the single element tests of material models 058 and 158 can be seen in Table 17 and Table 18. The values from LS-DYNA were compared with the values entered on the material card.

Table 17: Material Model_058 Single Element Results

	LS-DYNA Value	Material Card	Per cent Difference
Tensile Stress 0° (GPa)	0.916	0.916	0.00%
Tensile Stress 90° (GPa)	0.976	0.976	0.00%
Compressive Stress 0° (GPa)	0.560	0.56	0.00%
Compressive Stress 90° (GPa)	0.552	0.552	0.00%
Shear Stress 0° (GPa)	0.133	0.135	-1.51%
Shear Stress 90° (GPa)	0.133	0.135	-1.59%

All of the values from the material model 058 simulations align well with the values entered on the material card.

Table 18: Material Model_158 Single Element Results

	LS-DYNA Value	Material Card	Per cent Difference
Tensile Stress 0° (GPa)	0.916	0.916	0.00%
Tensile Stress 90° (GPa)	0.976	0.976	0.00%
Compressive Stress 0° (GPa)	0.560	0.56	0.00%
Compressive Stress 90° (GPa)	0.552	0.552	0.00%
Shear Stress 0° (GPa)	0.133	0.135	-1.43%
Shear Stress 90° (GPa)	0.133	0.135	-1.50%

Similar results were obtained with material model 158.

5 Material Testing Simulations

5.1 Tensile Simulations

A simulation of the tensile testing was created as a preliminary step to validating the material model. The simulation was set up using the same dimensions from the actual material testing (3.2.1). All elements were quadrilateral elements with each side being 5 mm in length (Figure 35). The simulation was also run with all elements at half the size (2.5 mm in length) but this did not affect the results. Each element had one point of integration for every prepreg ply in the specimen. The tabs in the actual material testing were made from a glass fibre prepreg and bonded to the carbon specimens. For simplicity, the elements representing the tabs in the simulation were modelled as thicker carbon pieces. This saved having to model the bond between the glass and carbon using a contact definition, which would increase the complexity of the simulation. The specimen is restrained by the left-hand tab and a constant velocity is applied to the right-hand tab.

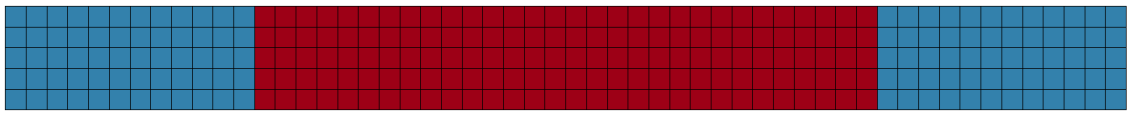

Figure 35: Tensile Simulation FE

During the beginning of the simulation, a tensile wave moved across the specimen. This can be seen in Figure 36, which plots the stress in each element in the loading direction (x-direction) at different times during the simulation. The arrows indicate the direction of travel of the tensile wave. The colour scale in Figure 36 is different at each time-step, therefore, the colours in the diagram should only be used to visualise the movement of the tensile wave as they do not relate to each other.

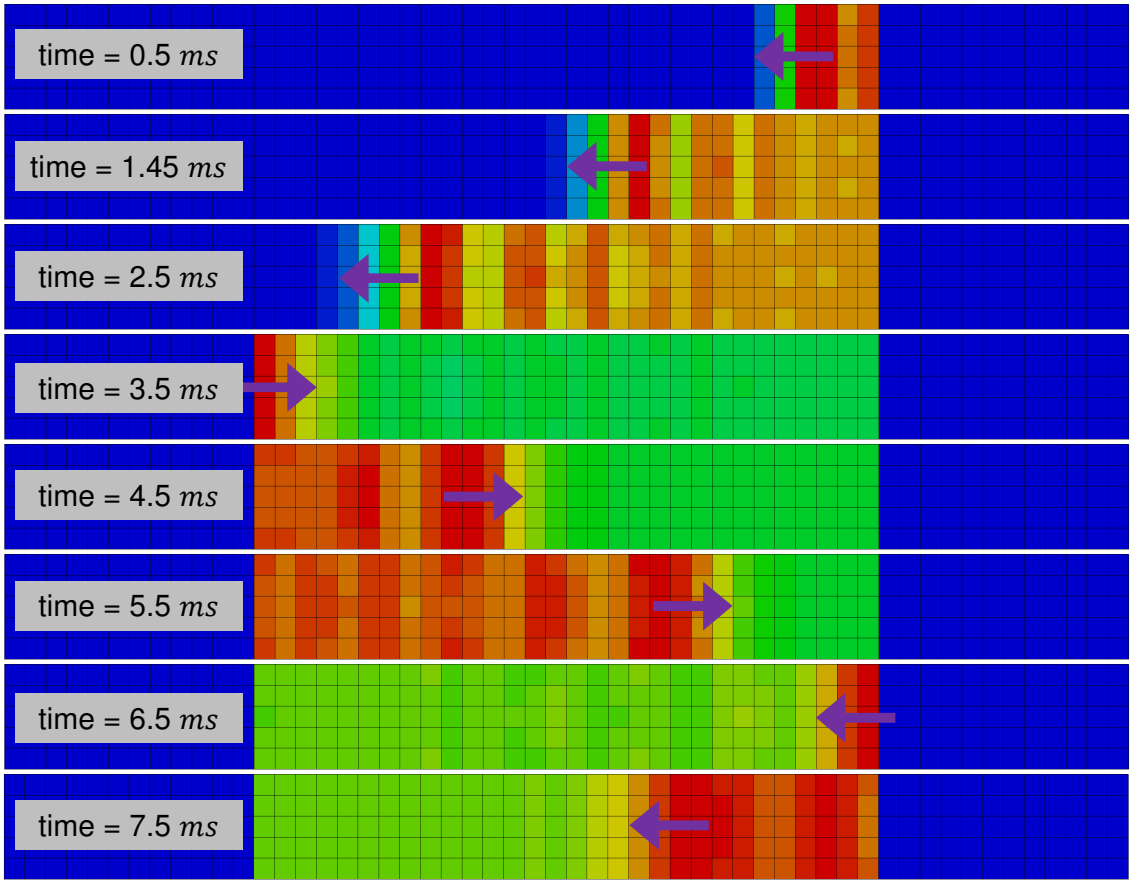

Figure 36: Tensile Simulation – Tensile Wave

The specimen eventually failed in a similar fashion as in the actual tests. At seemingly the same time, the specimen broke at both ends, where the tabs are bonded. This can be seen in Figure 37.

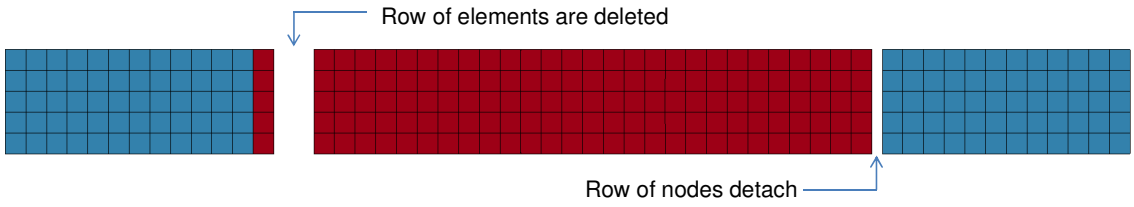

Figure 37: Tensile Simulation at Failure

Most likely, the failure at the fixed tab occurs first and the failure at the moving tab is subsequently caused by the tensile wave moving along the specimen after failure occurs at the fixed tab. However, this could not be clearly seen in the simulation. The results from the simulations as compared the averages of the actual tests can be seen in Figure 38 and Figure 39.

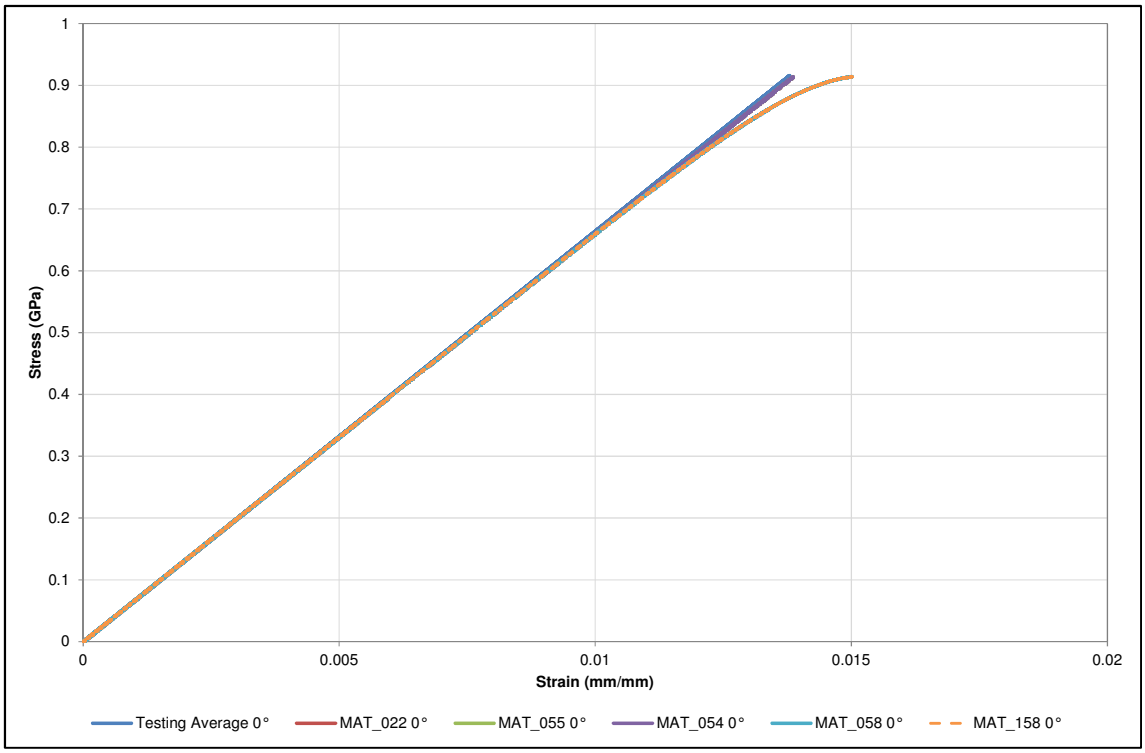

Figure 38: 0° Tensile Simulation Results

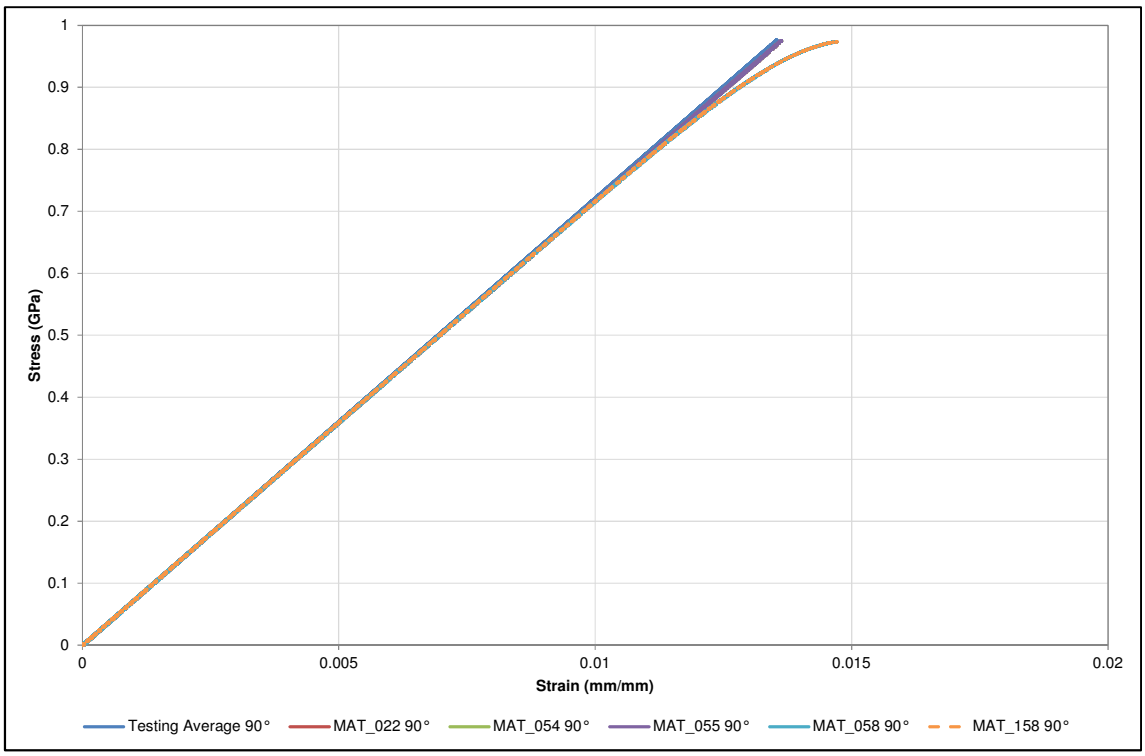

Figure 39: 90° Tensile Simulation Results

Material models 022, 054, and 055 followed the testing average with the same slope and maximum stress. Material models 058 and 158 followed the slope of the testing average up to a point of divergence which represents the damage inherent in these models. Material models 058 and 158 then failed at the same maximum stress as the testing average.

5.2 Compressive Simulations

A simulation of the compressive testing was created as a preliminary step to validating the material model. The simulation was set up using the same dimensions from the actual material testing (3.3.1). All elements were quadrilateral elements with 10 elements along the width of the specimen (Figure 40). This resulted in an element size of 1.9 mm at the ends and 1.27 mm within the gauge length. The simulation was also run with all elements at half the size (0.95 and 0.635 mm in length) but this did not affect the results. Each element had one point of integration for every prepreg ply in the specimen. The specimen is restrained by the left-hand nodes and a constant velocity is applied to the right-hand nodes. Restraints were also placed on some nodes within the gauge length that prevented the nodes from moving out of plane, which is representative of the test setup used.

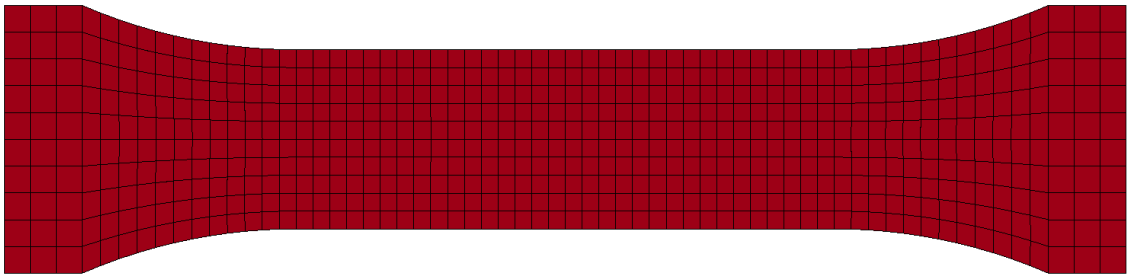

Figure 40: Compressive Simulation FE

The compressive simulation failed in a similar way to the actual tests. Elements began to fail and be deleted where the specimen changed cross-section. This can be seen in Figure 41.

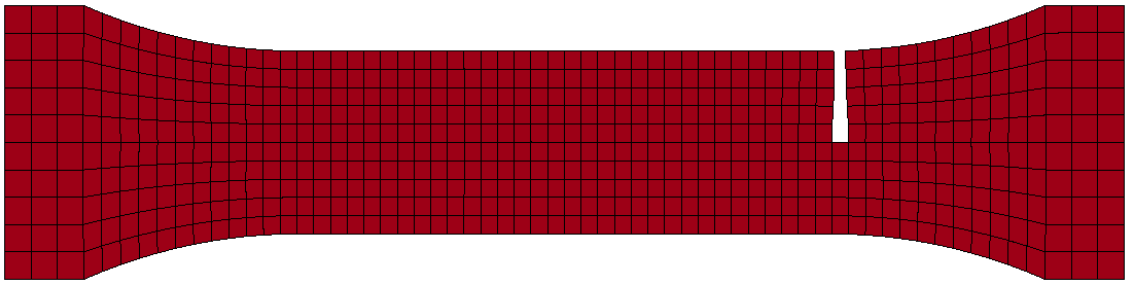

Figure 41: Compressive Simulation at Failure

The results from the simulations as compared the averages of the actual tests can be seen in Figure 42 and Figure 43.

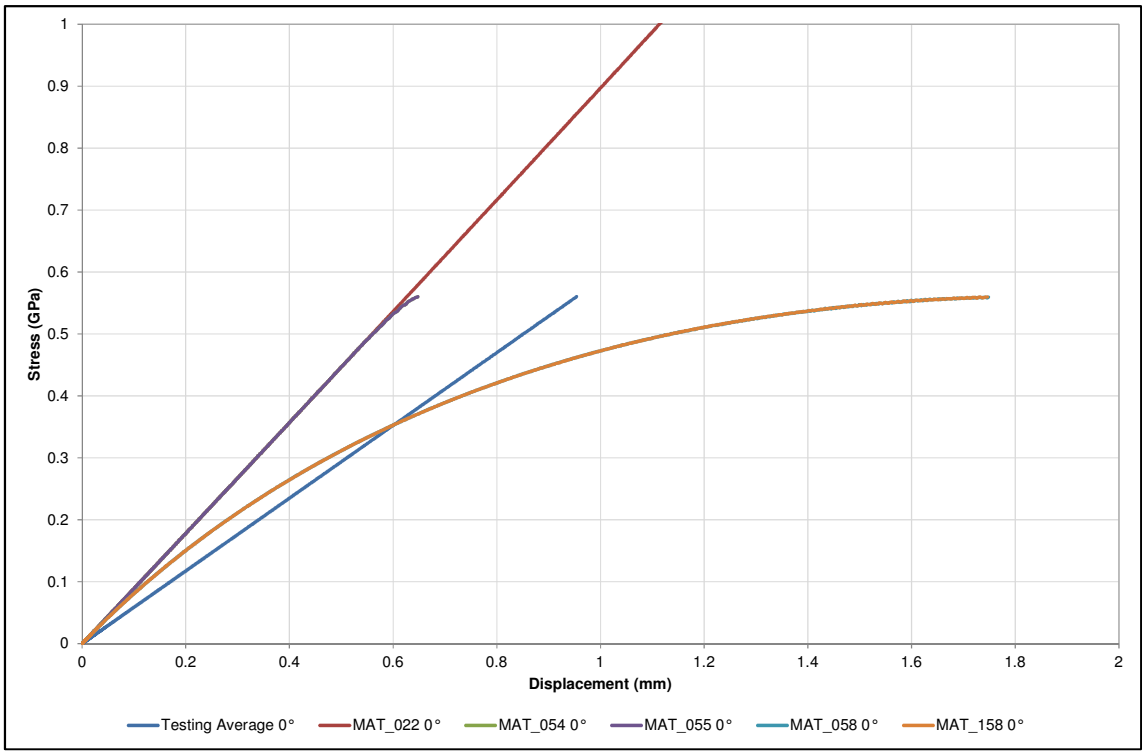

Figure 42: 0° Compressive Simulation Results

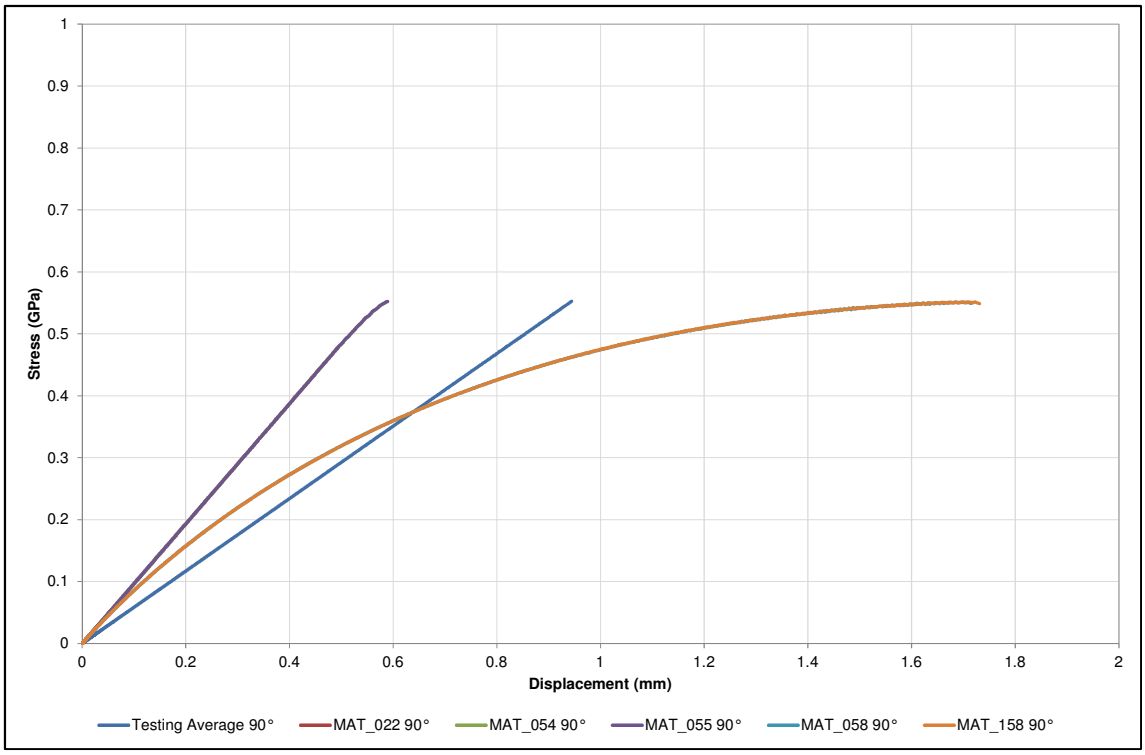

Figure 43: 90° Compressive Simulation Results

All of the material models failed at the same stress as the tests, with the exception of material model 022 in the 0° direction. This is due to material model 022 not having a failure criterion in compression for the 0° direction. The slope of each material model is different than the tests. This is due to the fact that the compressive modulus could not be directly measured using the test setup. It was instead elected to keep the given value for the compressive modulus. As can be seen in the figures, the given value for the compressive modulus does not match with the test results. As previously seen with the tensile simulation results, material models 058 and 158 exhibit damage until reaching the failure stress.

5.3 Shear Simulations

A simulation of the shear testing was created as a preliminary step to validating the material model. The simulation was set up using the same dimensions from the actual material testing (3.4.1). The material models used were 055 and 158. All elements were quadrilateral elements with the majority of the elements having a length of 1 mm on each side (Figure 44). This simulation was only run

with the elements at this size. Each element had one point of integration for every prepreg ply in the specimen. The specimen is restrained by the left-hand nodes and a constant velocity is applied to the right-hand nodes.

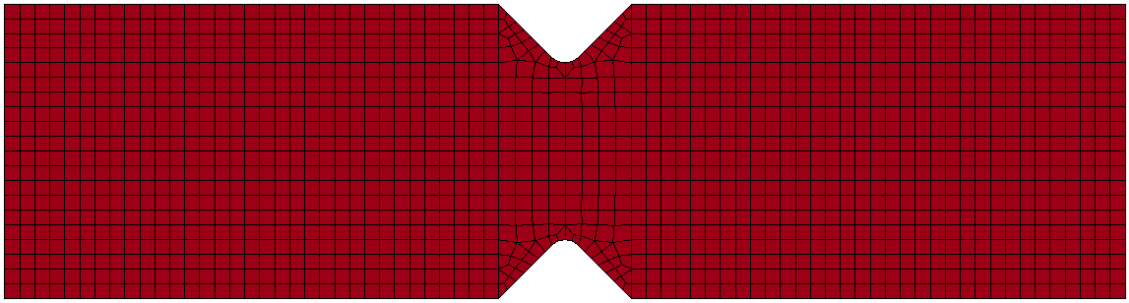

Figure 44: Shear Simulation FE

The simulations failed as expected, with elements failing in the centre of the specimen, where the cross-section is at a minimum. The failure of the simulations can be seen in Figure 45.

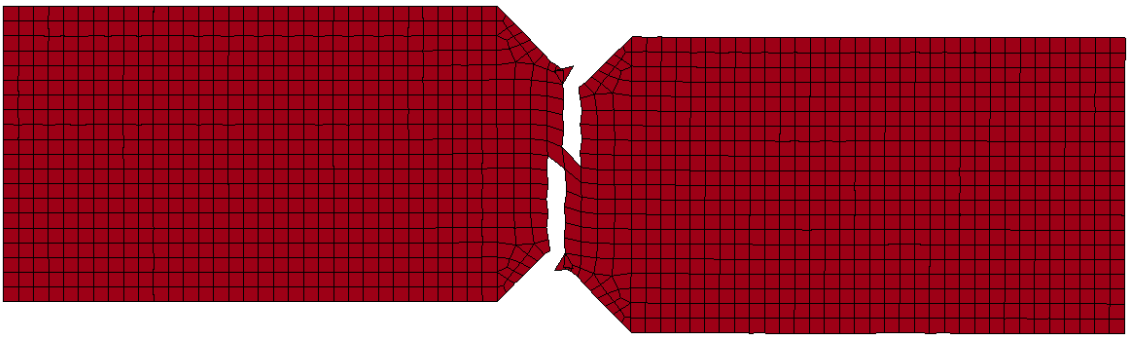

Figure 45: Shear Simulation at Failure

The results from the simulations as compared to one of the actual tests can be seen in Figure 46.

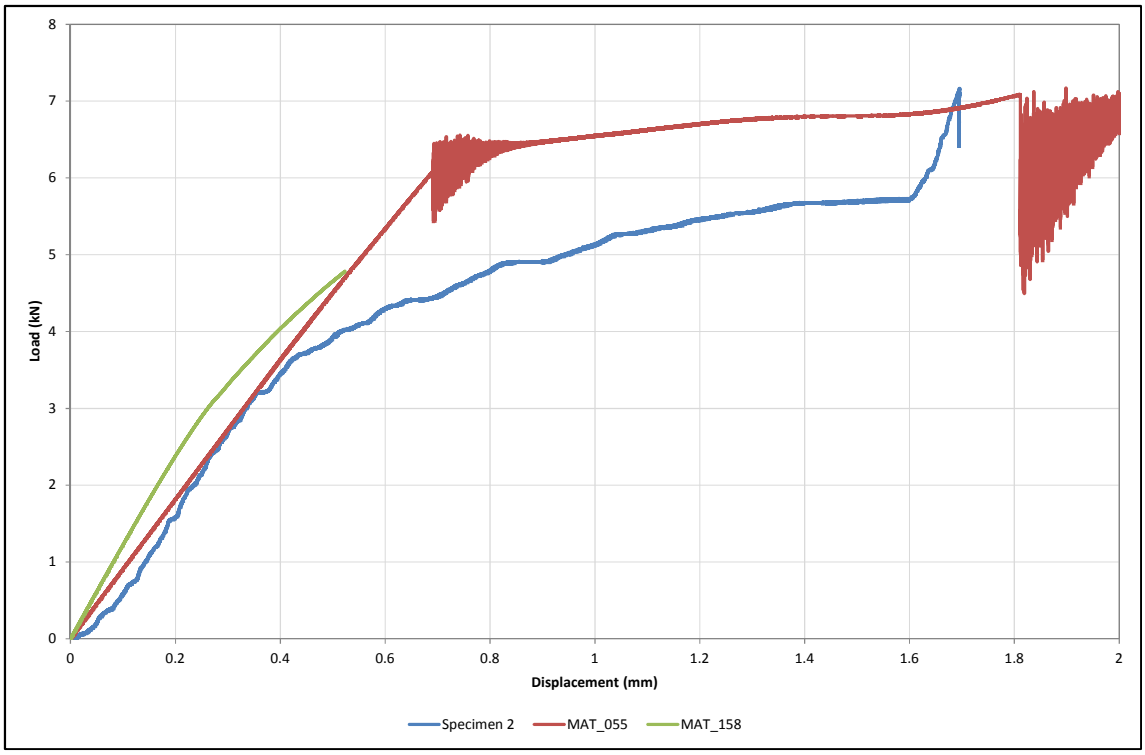

Figure 46: Shear Simulation Results

Material model 158 underestimated the failure load while material model 055 overestimated the failure load. The slopes of both material models matched well with the test data when compliance in the test setup is taken into account. Shear simulations were also run using material model 022 and 058 but the simulations became unstable and did not produce a satisfactory result.

5.4 Material Simulation Conclusions

Overall, it was seen that material models 054 and 055 were better correlated to the actual test data. Material model 022 matched the test data well for tension, but fell short in compression because of a lack of defined compressive failure strength in the 0° direction. The inherent damage present in material models 058 and 158 caused these simulations to drift from the test data, most notably in the compressive simulations. Material models 058 and 158 may achieve results that are closer to the test data if their parameters are adjusted. For the shear test simulations, only the results for material models 055 and 158 are shown because the results for material models 022 and 058 were unstable.

More time would be needed to examine why these simulations became unstable.

It is interesting to note that in all cases of tensile, compressive, and shear loading, the simulations failed much quicker than the actual tests, in real time. This occurred even when the simulation results matched well with the test results. This could be due to compliances in the test setup or the Instron machine itself. This could also point to a fault in the controls of the Instron machine, that perhaps it was not applying the correct velocity. However, review of the time versus displacement data shows that this was not the case and that the velocities applied during the physical testing were as expected.

6 Coupon Testing

Testing of smaller structures is done at MGP in order to compare the impact performance of different materials. The standard shape used is a simple tube with a machined chamfer as a trigger. The tool is a steel male mandrel with an outer diameter of 48.5 mm. For the specific prepreg that will be used, as described in Section 3, the tube is laminated with six plies which results in a nominal thickness of 1.41 mm. The thermal expansion of the steel mandrel causes the final cured tubes to have a larger diameter than the mandrel. The tubes are cut to 100 mm in length. A 45° chamfer at the top edge of the tube is post-machined after cure. This chamfer serves as the “trigger” or “initiator” of the tube. A trigger is the part of the tube that helps to initiate the crushing of the tube because local failures occur at the trigger. Without a trigger, the initial load will be higher and the collapse mode of the tube could be global buckling. Buckling collapse modes are undesirable for energy absorption because they are less efficient than lamina bending and transverse shearing (Farley, 1992, p. 7). Two additional configurations of the laminate schedule were chosen: three plies and twelve plies. These were selected in order to compare the specific energy absorption (SEA) of each configuration.

6.1 Coupon Geometry

The following tables show the dimensions and mass of each coupon prior to testing.

Table 19: Measurements of 3-ply Configuration Coupons

Coupon #	1	2	3
Mass (kg)	0.0158	0.0156	0.0156
OD (mm)	50.12	50.06	50.11
ID (mm)	48.67	48.66	48.68
t (mm)	0.73	0.71	0.72
L (mm)	100.03	100.13	100.23
t/OD	0.015	0.014	0.014
OD/t	68.66	70.68	69.43

Table 20: Measurements of 6-ply Configuration Coupons

Coupon #	1	2	3
Mass (kg)	0.0333	0.0331	0.0331
OD (mm)	51.48	51.54	51.45
ID (mm)	48.71	48.65	48.67
t (mm)	1.42	1.41	1.39
L (mm)	100.08	100.10	100.01
t/OD	0.028	0.027	0.027
OD/t	36.25	36.55	37.01

Table 21: Measurements of 12-ply Configuration Coupons

Coupon #	1	2	3
Mass (kg)	0.0658	0.0658	0.0658
OD (mm)	54.30	54.29	54.38
ID (mm)	48.66	48.67	48.67
t (mm)	2.79	2.79	2.76
L (mm)	100.40	100.33	100.12
t/OD	0.051	0.051	0.051
OD/t	19.49	19.47	19.68

6.2 Testing

Each tube was tested in the Rosand drop tower at the CIC (Figure 47). The first coupon of each ply configuration was tested at half of the intended energy to ensure that there would not be any damage to the drop tower. As an additional precaution, aluminium honeycomb was placed around the first few coupons tested (Figure 48). If there was a problem with the coupon, the honeycomb would have prevented a collision of the impacting mass and the drop tower base.

Figure 47: Drop Tower

Within the drop tower, a mass is released from a set vertical height onto the test piece. The height the mass is dropped at is determined by the controlling software of the drop tower, using the desired impact velocity. The drop tower software simultaneously records the time, load, and velocity during the test. The data was recorded at 20 kHz. The nominal speed used was 7 $\frac{m}{s}$ and the impact mass was 67.2 kg.

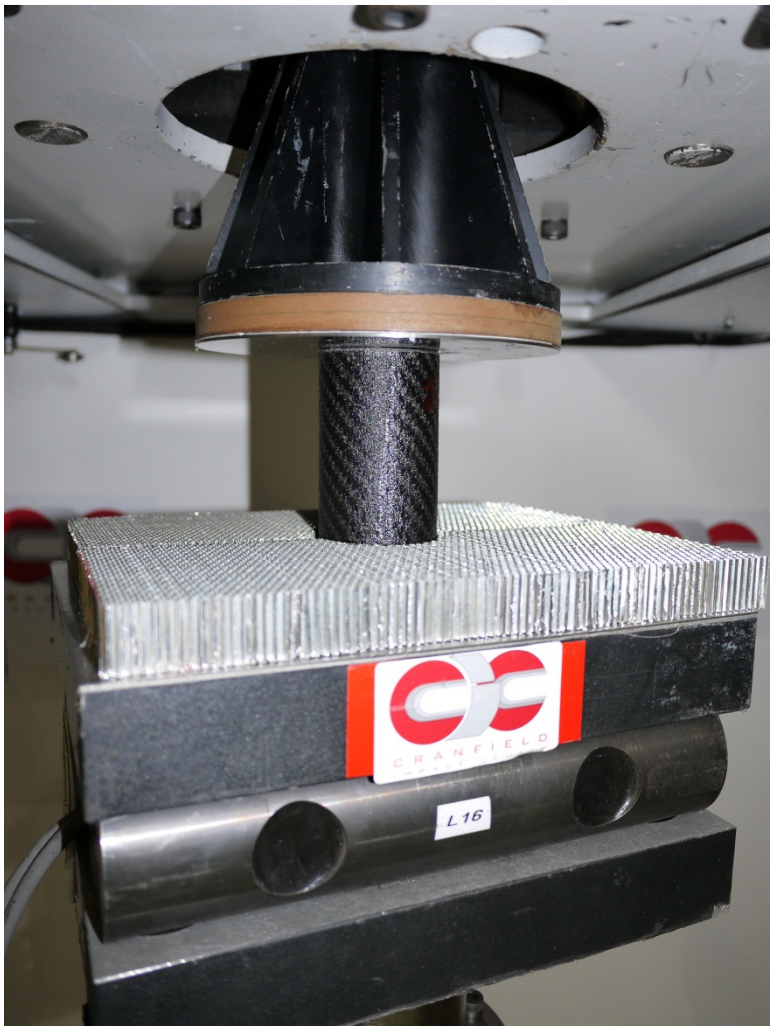

Figure 48: Coupon in Drop Tower

6.3 Results

All tubes failed by brittle fracturing, which is a combination of transverse shearing and lamina bending (Farley, 1992). The brittle fracturing failure is dominated by lamina bending, which is a matrix-controlled crushing mode (Farley, 1992). A typical failure can be seen in Figure 49. The lamina bending can be seen by plies of each coupon folding towards the outside and towards the inside of the tube. A good view of the debris wedge that was formed can be seen in Figure 50.

Figure 49: Coupon Failure

Figure 50: Debris Wedge

The raw data from each coupon configuration can be seen in 0. A graph comparing the SEA of each coupon versus the impact energy can be seen in Figure 51.

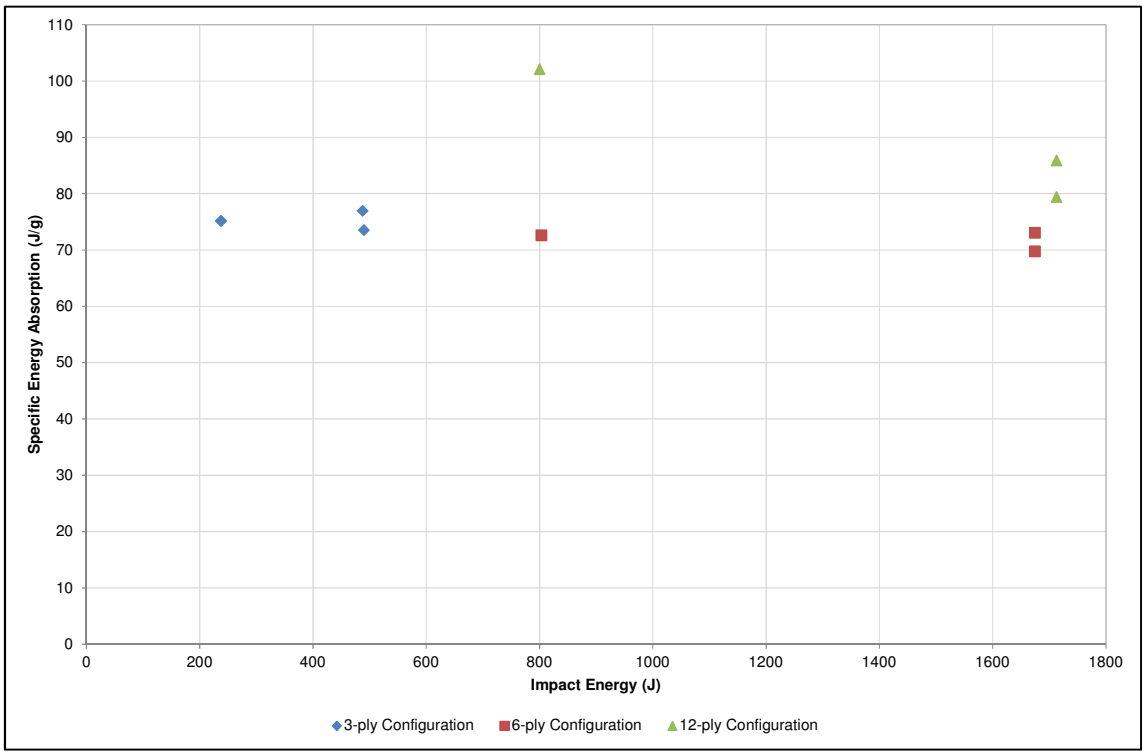

Figure 51: SEA versus Impact Energy

Figure 51 shows that although different impact energies were used, all of the coupons have similar values for SEA. The 12-ply configuration coupon that was impacted with a lower energy is an exception to this.

7 Coupon Testing Simulations

It was decided to start the simulations with material model 055 because it performed the best in the material testing simulations. Material model 054 had an identical performance to material model 055, however, material model 054 requires more parameter inputs. It was assumed that working with a smaller selection of parameters would provide a better baseline model to build on.

The simulations contain three main components: the composite tube, the lower wall (the floor), and the impacting wall. The composite tube was modelled using shell elements, as in the single-element testing. The coupon configuration chosen for the laminate was the 6-ply configuration. The impacting wall was given a mass of 67.2 kg and an initial velocity of 7.02 $\frac{m}{s}$. The value of friction between the tube and both surfaces was set at 0.5 for both the static and the dynamic friction.

In order to save computational time, not all simulations were run until the end of the impact. The simulation would only be run as far as was needed to examine the effect of parameter changes.

7.1 MAT_055

Early simulations that were performed frequently terminated prematurely due to out-of-range velocity nodes. This occurs when a node experiences a sudden change of velocity within one time-step. This was solved using a combination of time-step scale factors, element formulation, and hourglass control. This combination of values can be seen in Table 22.

Table 22: Parameters Affecting Simulation Stability

Parameter	Value	Description	Card used on
Time-step scale factor	0.9	Scale factor for calculated timestep	*CONTROL_TIMESTEP
Element formulation	2	One point of integration shell	*SECTION_SHELL
Hourglass Control Type	4	Hourglass viscosity type	*CONTROL_HOURGLASS
Hourglass Coefficient	0.01	Scale factor for hourglass	*CONTROL_HOURGLASS

7.1.1 Trigger Angle and Mesh

The trigger geometry proved to have a great effect on the stability of the structure. An effort was made to model the trigger so that it best represented the actual trigger on the structure, which is a 45° chamfer that begins as the thickness of the laminate and becomes a knife edge. A diagram of the geometry of actual tube chamfered trigger can be seen in Figure 52. This is only a diagram of the uppermost portion of the tube and is not to scale.

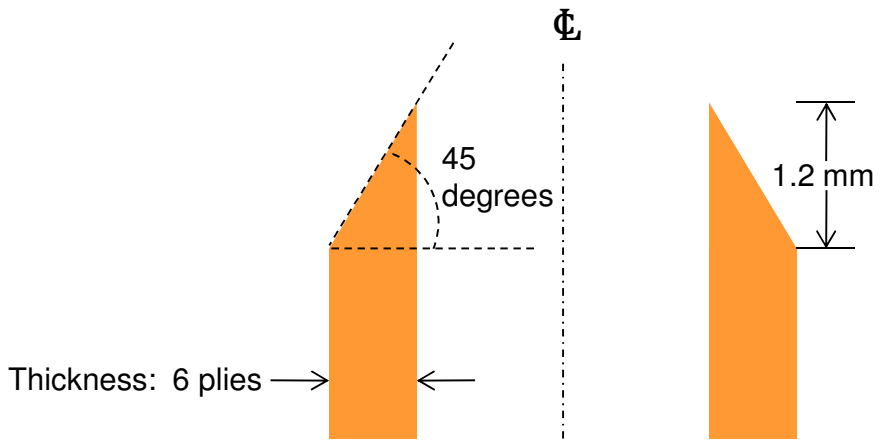

Figure 52: Actual Tube Trigger Diagram [not to scale]

The representation of the initial finite element model of the chamfered trigger, using shell elements, can be seen in Figure 53. Each coloured bar represents a shell element and the yellow circles are nodes. Again, this is only a diagram of the uppermost portion of the tube and is not to scale. In this model, the

uppermost elements were aligned with the main tube elements and were given different values for thickness in order to represent the chamfer on the tube.

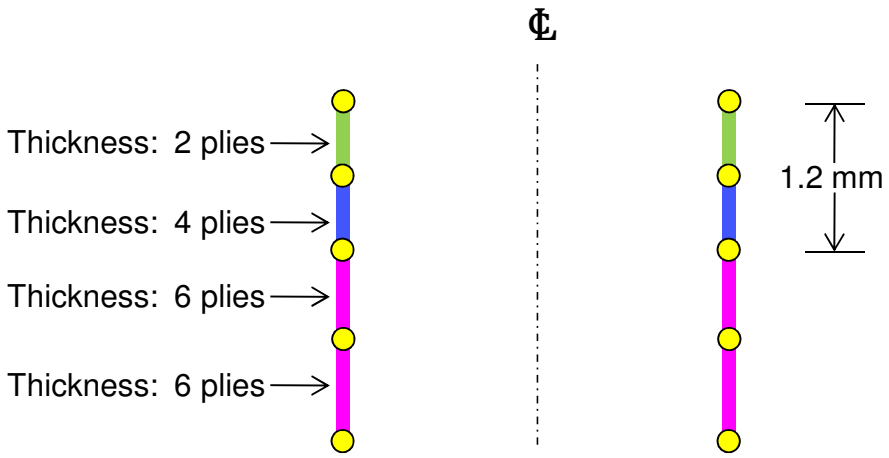

Figure 53: Initial Shell FE Tube Trigger [not to scale]

A representation of how this initial model would physically look can be seen in Figure 54.

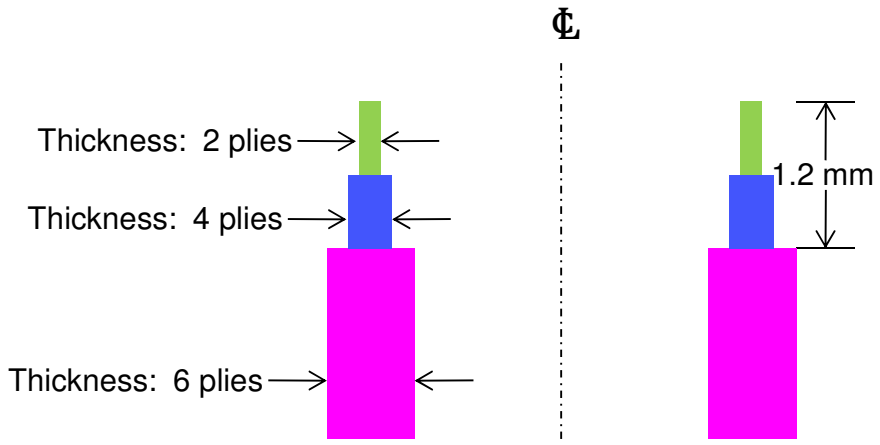

Figure 54: Physical Representation of Initial Shell FE Tube Trigger [not to scale]

Different combinations of thicknesses were trialled; however, this model of the trigger had to be moved away from in order to keep the tube stable. It was found that the trigger elements needed to be modelled at an angle to the main tube elements. The value of the model trigger angle was varied in the

simulations and the results can be seen in Figure 58. A diagram of the finite element model with an angled trigger can be seen in Figure 55.

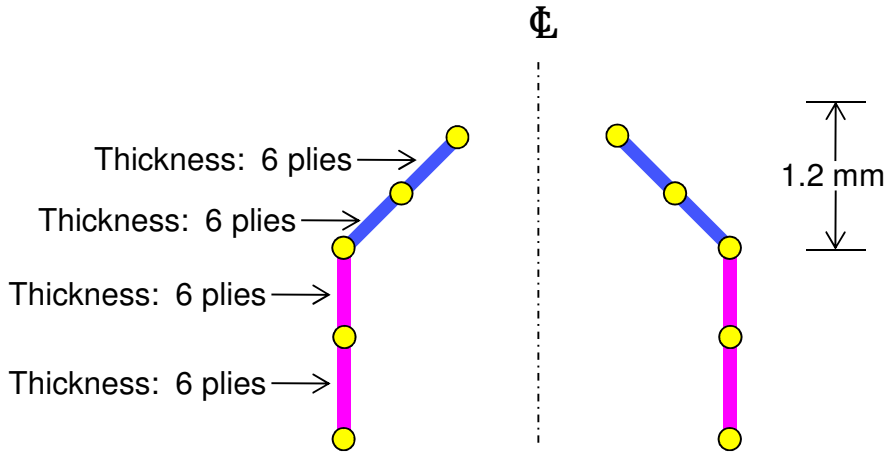

Figure 55: Angled Trigger Shell FE [not to scale]

For this model, all shell thicknesses were set to be equal. A representation of how this angled trigger model would physically look can be seen in Figure 56.

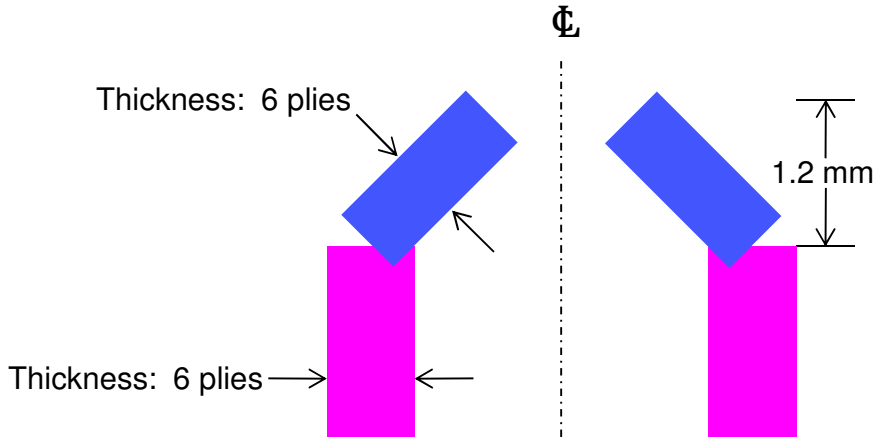

Figure 56: Physical Representation of Angled Trigger Shell FE [not to scale]

This difficulty with simulating the trigger accurately supports the necessity to look at a different geometry for material characterisation testing. A diagram of the entire model can be seen in Figure 57. The green elements are rigid solid elements that represent the impacting wall.

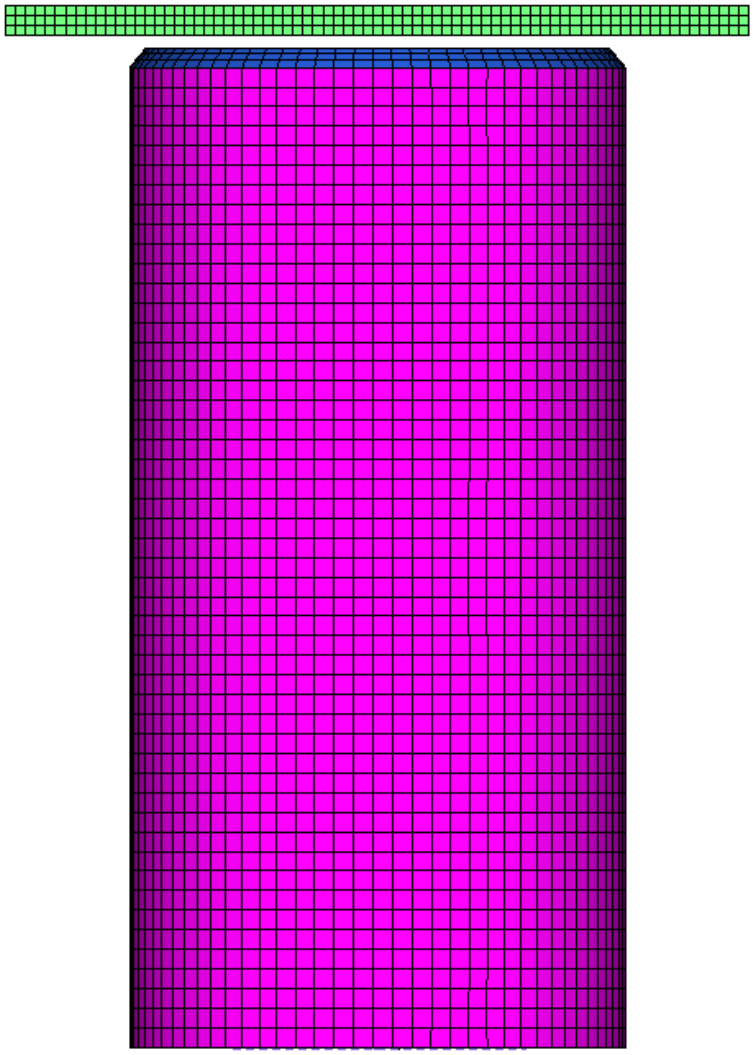

Figure 57: Basic Tube and Chamfer Mesh

The trigger angle mostly affects the initial peak load of the simulation. A comparison of different trigger angles is shown in Figure 58. A larger angle means the trigger is steeper, and more in line with the tube.

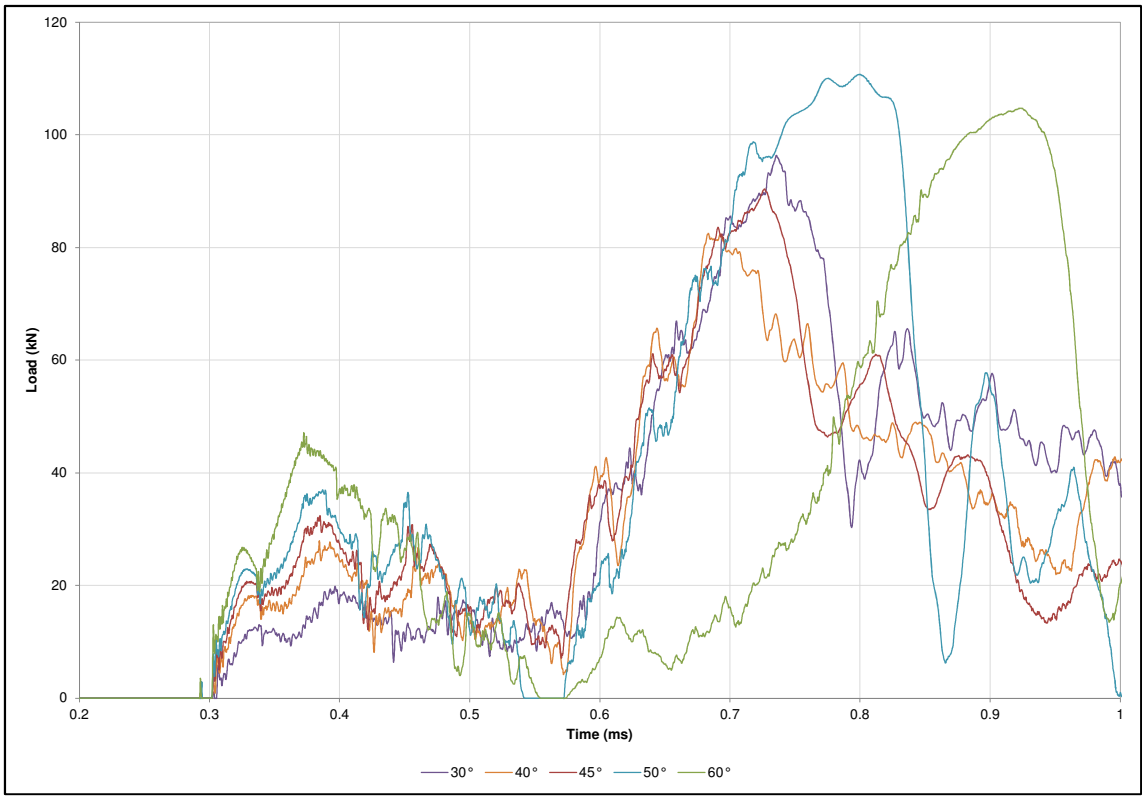

Figure 58: Trigger Angle Effect

The higher angle produces a higher peak load because the fibres are more in line with the loading axis. Note that the graph is truncated in order to only view the relevant part of the simulation. A tabulated list of the initial peak loads for each trigger angle can be seen in Table 23.

Table 23: Initial Peak Load of each Trigger Angle

Trigger Angle ($degrees$)	30	40	45	50	60
Initial Peak Load (kN)	19	27	32	36	47

While performing simulations to look at the effects of trigger angles, it was found that the load would drop to zero shortly after the impacting wall was past the trigger elements. Closer inspection showed that this is caused when the majority of elements in a horizontal row are deleted at once, which cause the tube to lose contact with the wall and reduced the load to zero. An example of a simulation exhibiting this drop in load can be seen in Figure 59.

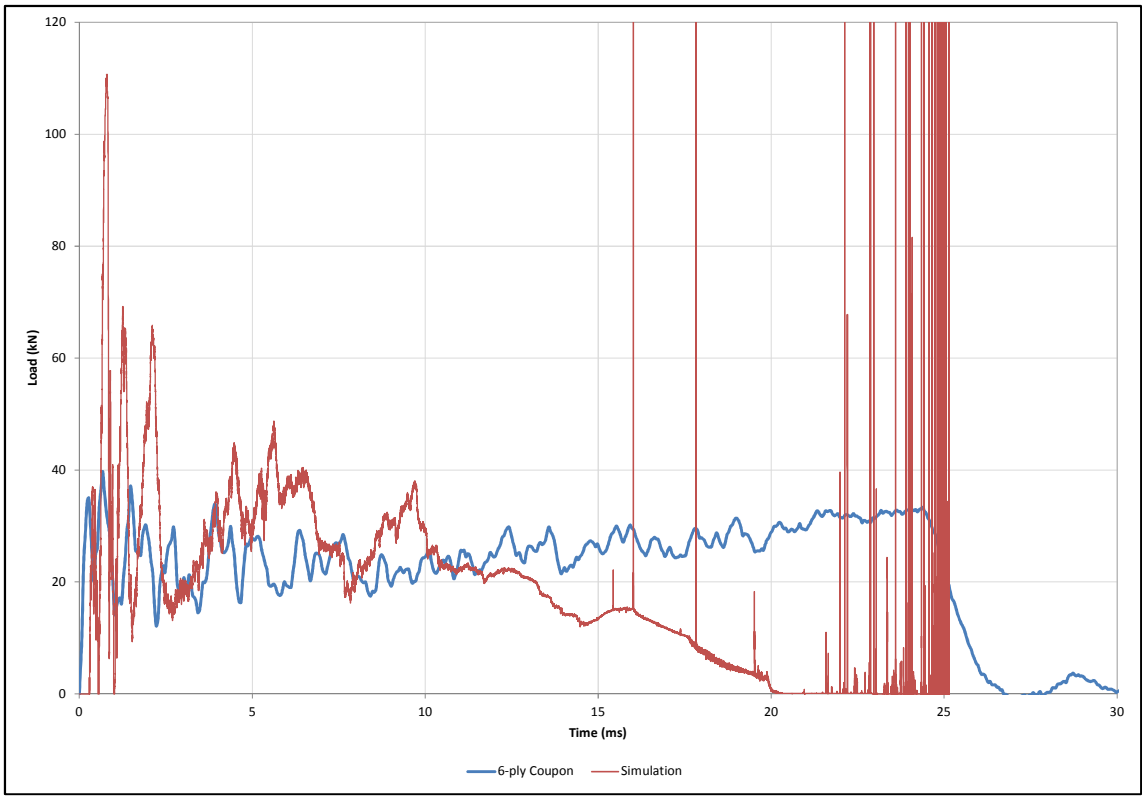

Figure 59: Simulation Load Drops to Zero

An idea to solve this was to force the elements to be different sizes around the circumference of the tube. If the elements in a horizontal row were of a different size relative to neighbouring elements, they would delete at different times. The first attempt at this kind of mesh can be seen in Figure 60 and is called a "2:1 Element Trigger." From the figure it can be seen that some element are about half as big as others. This design alleviated the problem somewhat but there would still be a significant drop in load after the impacting wall passes the trigger elements.

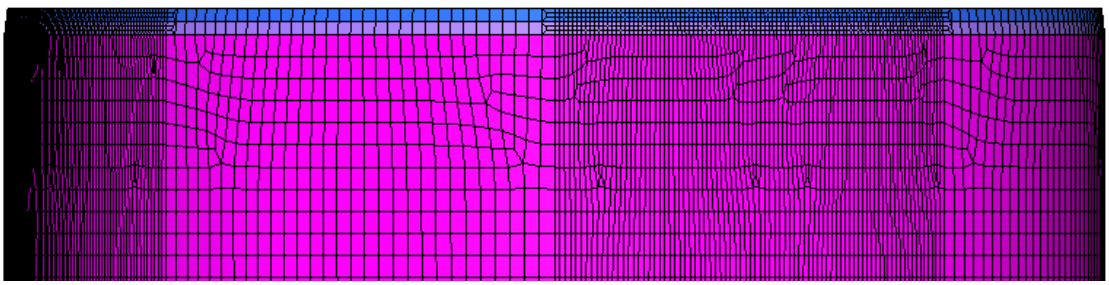

Figure 60: 2:1 Element Trigger

The next step in the mesh design was to drastically change the shape of elements along a horizontal row. This was done by creating a wave-like surface and using that to split the tube face. The tube surface split by these “cake layers” can be seen in Figure 61. Splitting the tube surface in this way forces the elements to be created along the wave lines. This can be seen in Figure 62.

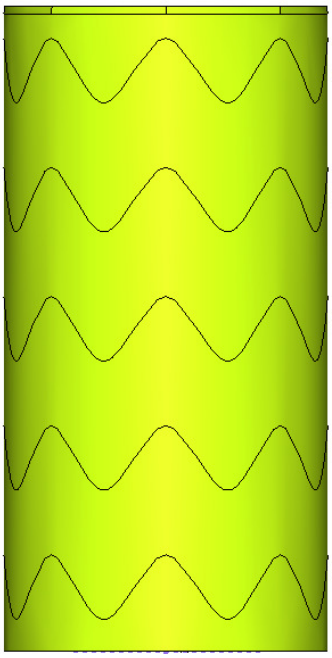

Figure 61: Cake Layer Surfaces

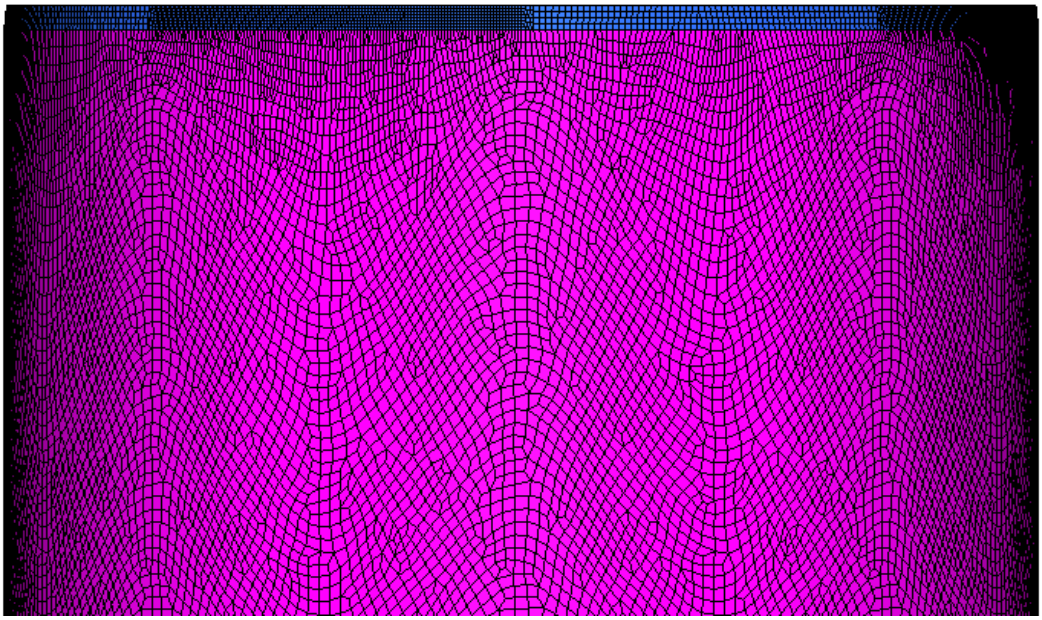

Figure 62: Cake Layer with 2:1 Trigger

In Figure 62 the main elements of the tube follow a wave around the circumference, while the trigger maintains the 2:1 feature from Figure 60. Again, this change was found to be helpful but not perfect. The problem was found to be that there still existed a horizontal line between the trigger and main part of the tube. Figure 63 shows what happened during the simulation. The trigger elements become detached from the main tube and leave the tube elements relatively intact. This simulation showed a lower first peak load but after the trigger was gone, there was another peak load that occurred when the impacting wall reached the remainder of the tube.

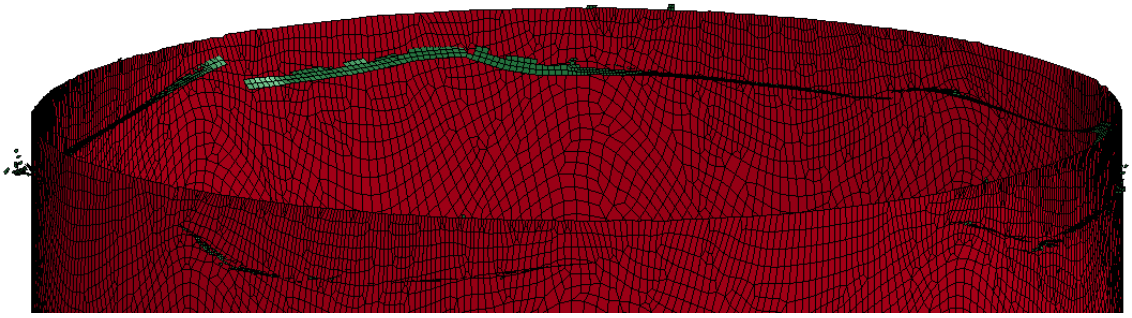

Figure 63: Trigger Separating from Main Tube

After this simulation, it was clear that the trigger elements and main tube elements needed to be integrated better. Originally, the tube and trigger were created in HyperMesh separately using a cylinder and a cone, respectively. The next approach was to create the trigger and main tube within one operation. A line was drawn and then revolved around the loading axis. This created a smooth transition from the trigger to the main tube and enabled elements to have nodes on either side of the previously existing boundary. This configuration of an integrated cake layer trigger can be seen in

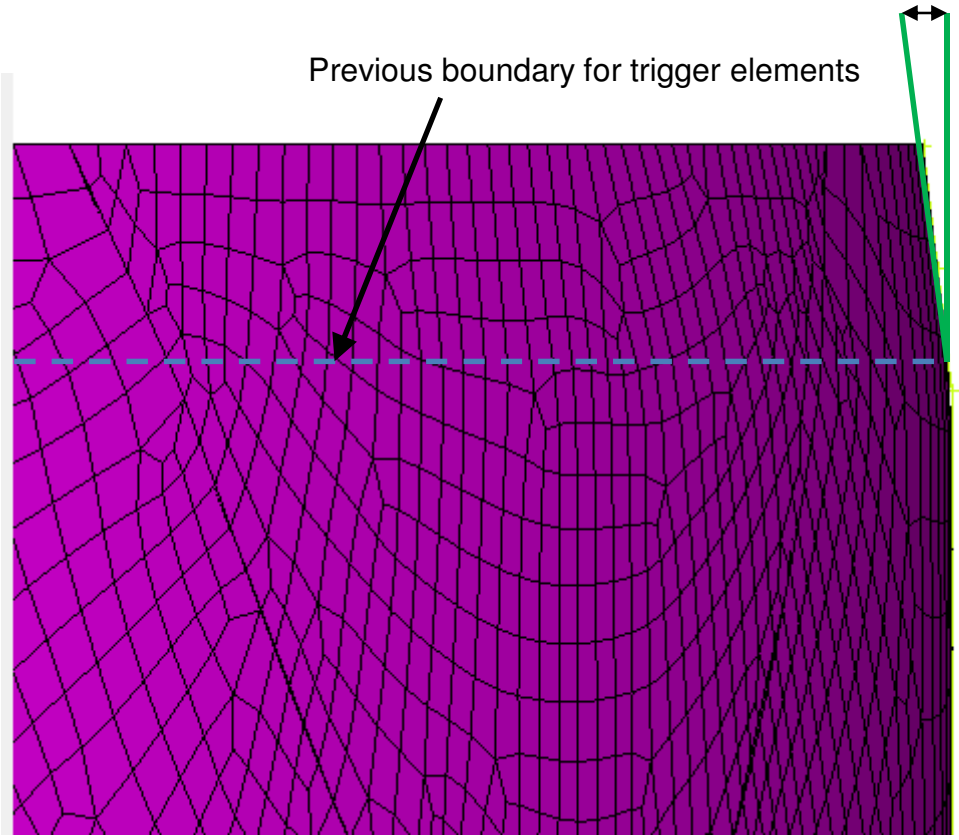

Figure 64: Integrated Trigger

This method worked well in decreasing the first peak load. However, the use of this method only worked up until a certain point. When the radial distance between the top of the trigger and the main tube goes beyond 40% of the laminate thickness, the surfaces no longer wanted to be continuous. This means that the trigger and main tube were still split by a horizontal line, even though the surface was made with a smooth, revolved line.

A mesh sensitivity study was done on this integrated cake layer model. It was found that a finer mesh did not produce the best results. It was also found that the element at the top of the tube should be of different sizes around the circumference, very similar to the 2:1 trigger mesh described earlier. Table 24 gives the values of the peak load for various mesh types. The first four rows refer to the starting mesh size; the next size from there is doubled, and then doubled again. An illustration of this can be seen in Figure 65. The remaining rows of Table 24 refer to meshes that have the same size elements throughout the mesh.

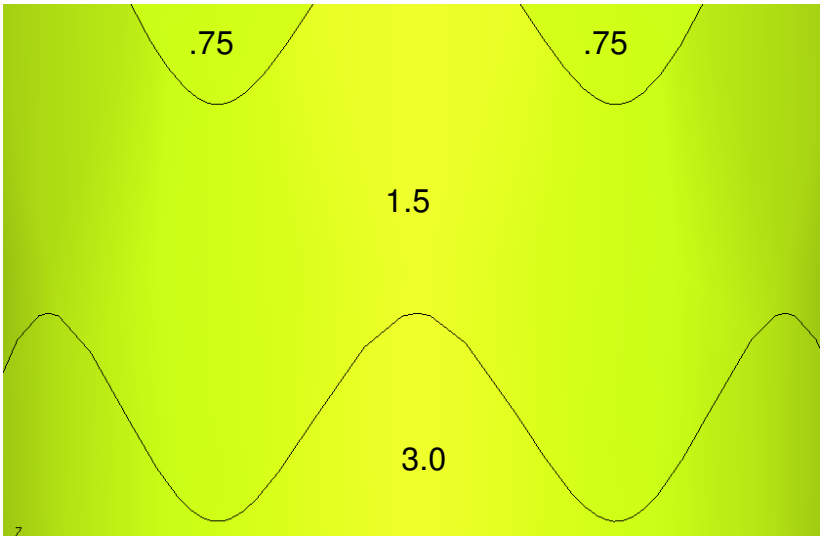

Figure 65: Mesh Size Designation

Table 24: Initial Peak Loads of each Mesh Type

Mesh Type	Initial Peak Load (kN)
0.5, 1.0, 2.0	83.25
0.75, 1.5, 3.0	47.15
0.85, 1.7, 3.4	42.57
1.0, 2.0, 4.0	80.45
.75 ALL	67.55
1.5 ALL	30.63

The data from the simulations can be seen in Table 24 compared with test results from one of the 6-ply coupons (Figure 66). In the case of this mesh setup, it can be seen that a mesh size of 0.5 and 1.0 give peak loads that are fairly close to each other, while the mesh sizes in between these two, 0.75 and 0.85, produce peak loads that are much lower. This suggests that the mesh size should be somewhere around 0.75 and 0.85, for this specific cake layer mesh setup.

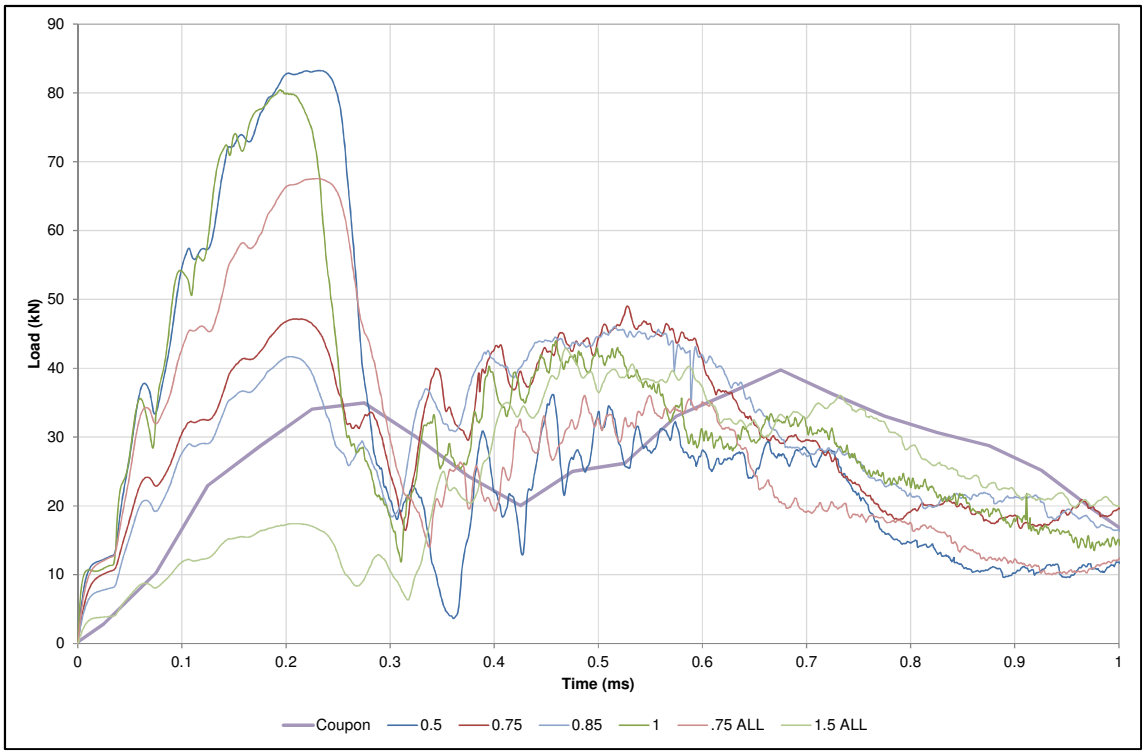

Figure 66: Effect of Mesh Density on Peak Load

7.1.2 TFAIL

TFAIL dictates if an element will fail or not based on its time-step. TFAIL is defined as a scale factor and it compares the initial time-step to the element's current time-step. For example, if TFAIL was set to 0.75, an element would fail when its time-step decreased to 75% of the initial time-step. A comparison of TFAIL numbers can be seen in Figure 67. The sustained loads from Figure 67 were found by taking an average through the maximum and minimum peaks in the data after the initial peak load. The tabulated data can be seen in Table 25.

Table 25: Sustained Load of each TFAIL

TFAIL	[Coupon]	0.75	0.80	0.85
Sustained Load (kN)	26.22	34.90	32.00	30.67

As expected, the higher TFAIL number produced a lower sustained load because a higher TFAIL number means that elements will be deleted sooner. It is interesting to note that in the case of this specialised mesh, the first peak load is the same for every value of TFAIL and the simulations only separate towards

the second peak. This is because the first elements are deleted for all simulations at the same time, when they reach their maximum stress criteria.

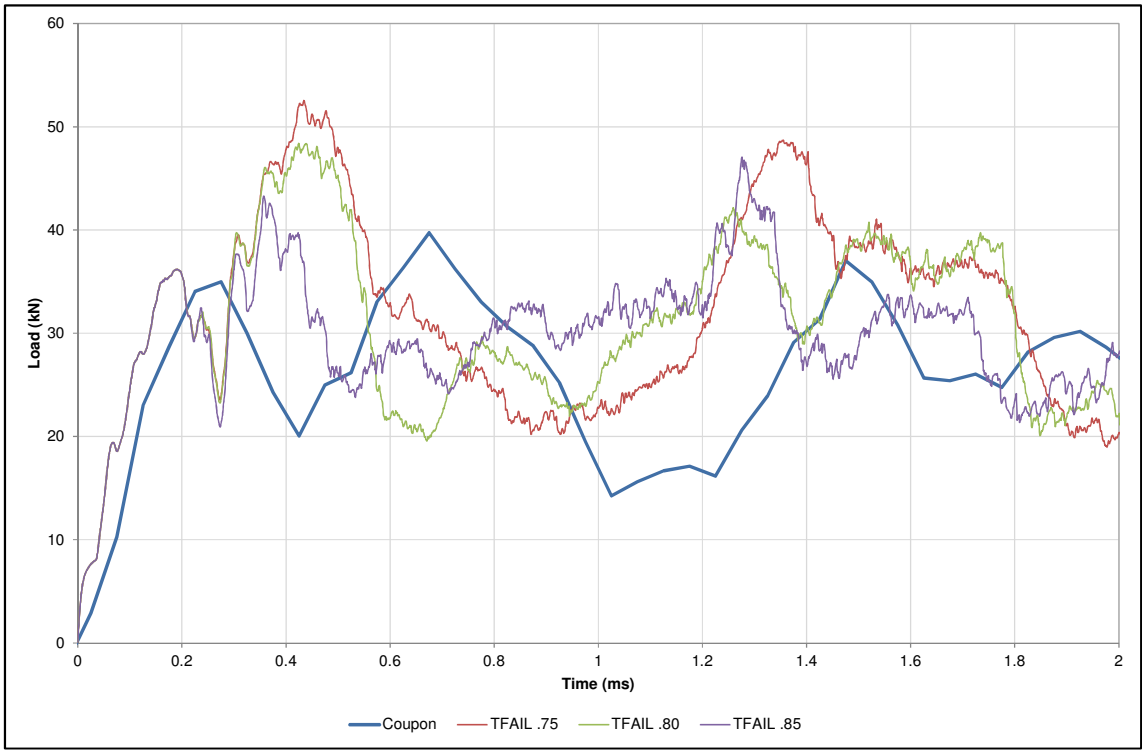

Figure 67: Effect of TFAIL Parameter on Sustained Load

In addition to affecting the peak loads, TFAIL also had an impact on whether the tube failed in a brittle or a ductile manner. If TFAIL was too low, the elements would not delete and cause the tube to exhibit local buckling like a metallic tube. If TFAIL was too high, the elements would delete too soon and the structure would not absorb enough energy.

7.1.3 SOFT

SOFT is a parameter that affects elements that are considered to be in the crashfront. Elements are in the crashfront if they shared a node with a deleted element. Once an element is in the crashfront, its strength is reduced by the factor assigned to SOFT. Simulations with different values of SOFT can be seen in Figure 68.

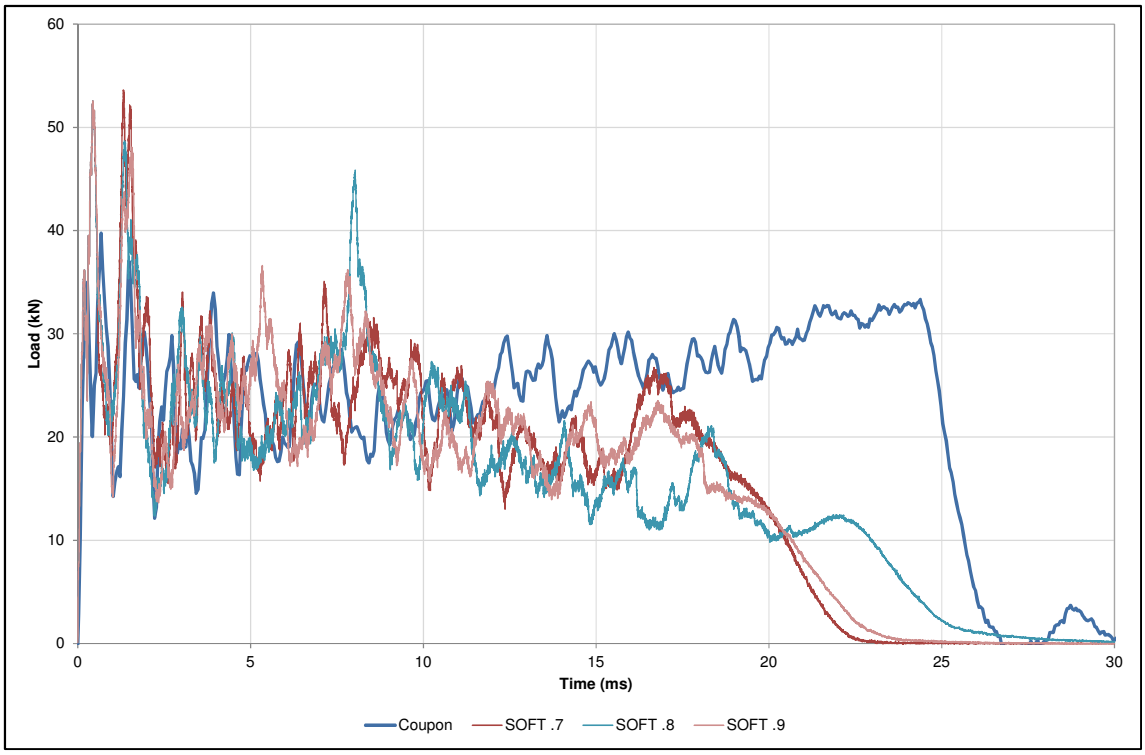

Figure 68: Effect of SOFT Parameter on Overall Energy Absorption

The SOFT parameter did not have any effect on the peak loads of the simulations (not shown). The SOFT parameter does not have an apparent effect on the overall energy absorption of the structures. Material model 055 only offers this one parameter for controlling the elements in the crashfront. Material model 054, on the other hand, has four parameters related to the crashfront. One of these parameters controls how many integration points must fail before the element is considered to be in the crashfront. This would increase the number of elements in the crashfront by allowing their strength values to be reduced before all integration points fail. It is possible that the range of other parameters being used with SOFT weakens its effect on the simulations.

7.1.4 Contact Stiffness

There are four parameters that directly affect the contact stiffness between the impacting wall and the tube. These parameters are listed in Table 26. Various combinations of these parameters have been simulated and can be seen in Figure 69.

Table 26: Contact Stiffness Scale Factors

	Value	Description	Card used on
SLSFAC	0.050	Scale factor for sliding interface penalties	*CONTROL_CONTACT
SFS	0.025	Scale factor on slave penalty stiffness	*CONTACT
SFM	1	Scale factor on master penalty stiffness	*CONTACT
SOFSCL	0.05	Scale factor for constraint forces of soft constraint option	*CONTACT

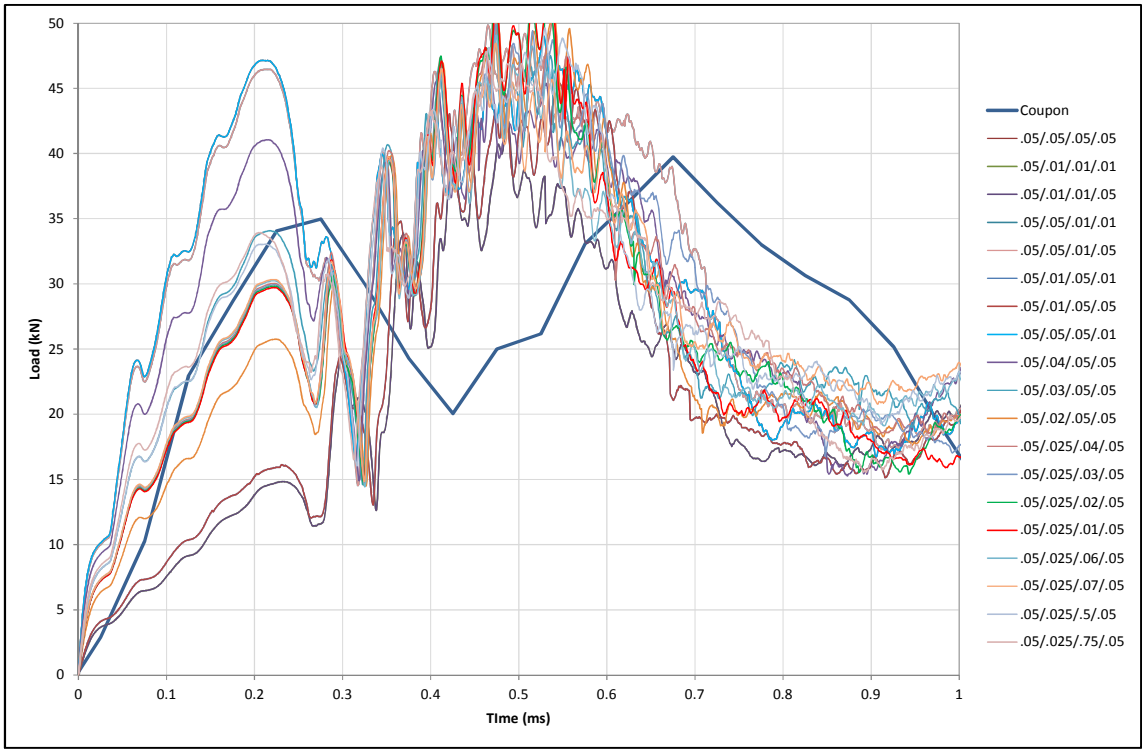

Figure 69: Effect of Contact Stiffness Parameters on Peak Load and Structure Stiffness

It can be seen in the graph that a combination of the contact stiffness scale factors will change the slope of the beginning of the graph. An optimum combination that best matched the coupon test data was selected and those values are listed in Table 26.

8 Conclusions and Future Work

While an exact match of simulation results to test data was not achieved, a lot was learned about the various parameters that are needed to make a simulation stable and how changes to parameters will affect the simulation results. An emphasis was placed on matching the simulations to the unfiltered test data and this was achieved for the beginning of the impact.

The tensile and compressive properties found during material testing were close to the given values by the prepreg manufacturer. It was shown from the tensile testing results that the transverse direction had higher properties than the longitudinal direction. For the compressive testing, the compressive modulus was not found because there was not any instrumentation used to measure the change of length of the specimen. The jig used for compressive testing could be modified to provide allowance for a strain gauge to be used on the specimen. A large discrepancy was found between the shear testing results and the given value. It is suspected that the method used for shear testing does not work with the evaluated material. Further work would have to be done to compare different methods for shear testing. For all of the material tests performed, it is suggested to use a higher number of specimens in order to get a better statistical spread of data.

The single-element simulations performed highlighted the limitations of each material model. Material model 022 does not have an allowance for compressive failure in the longitudinal direction. As such, the elements did not fail when subjected to a longitudinal compressive load. Material models 054 and 055 did not perform well in shear. More investigation would need to be done to determine why material models 054 and 055 did not perform as well in shear as material model 022. Material models 058 and 158 exhibited a nonlinear behaviour in the elastic region for all single element tests. This nonlinearity is because of the damage that is inherent in these models. The damage parameters for these models cannot be adjusted in LS-DYNA.

Simulations were performed using the same conditions as the actual material tests. Overall, it was seen that material models 054 and 055 were better correlated to the actual test data. Material model 022 matched the test data well for tension, but fell short in compression because of a lack of defined compressive failure strength in the longitudinal direction. The inherent damage present in material models 058 and 158 caused these simulations to drift from the test data, most notably in the compressive simulations. For the shear test simulations, only the results for material models 055 and 158 are shown because the results for material models 022 and 058 were unstable. More time would be needed to examine why these simulations became unstable.

Testing of small circular tube coupons were performed in a drop tower. Nine tubes were tested with three laminate variations. The laminate variations were three plies, six plies, and twelve plies. Each variation was subjected to different impact energies. All tubes failed by brittle fracturing. Although different impact energies were used, the majority of the coupons have similar values for specific energy absorption.

Simulations were performed that represented the drop tower tests of the circular tubes. A select amount of parameters were varied and the effect these had on the results were examined. It was found that the method of modelling of the chamfered trigger on the tube had a great effect on the initial peak load of the simulation. Furthermore, if this initial peak load was not relatively close to the value from the experiments, the tube would undergo global failure. A few alternative methods were used for defining the mesh. The best result occurred when the mesh was randomised through a combination of sectioning the surface of the tube and varying the size of surrounding elements. This created a mesh in which no element had a side that was perpendicular to the axis of the tube and the element size varied around the circumference of the tube. A size sensitivity study was done on this mesh and it was interesting to find that a finer mesh did not produce the best results. This optimum size for the mesh is most likely a property of the prepreg material, influenced by the size of the weave. This relationship between mesh size and material weave is an area for further

study. The best simulation result was based on the parameters outlined in Table 27. A graphical result of this combination of parameters can be seen in Figure 68 as SOFT .7.

Table 27: Best Simulation Result Parameters

Mesh	Trigger	TFAIL	SOFT
Cake Layer 0.75, 1.5, 3.0	Integrated Trigger, 30% of laminate thickness	0.75	0.70

For future work on this project, it would be ideal to judge all of the mentioned material models on their ability to define an impact structure. Material model 055 still seems like the preferred model to use for most studies, however, the amount of control material model 054 has on the crashfront is interesting and should be looked into further.

Material model 158 is interesting as it treats the material as if it has a spring-damper system overlaid on it. This will definitely be useful as it is apparent that prepreg materials are strain rate dependent. The definition of the spring-damper system is limited but it could prove to be useful.

An item that was not looked into during this project was the friction between the tube and the impacting wall. This could have a great effect on the results of the simulations, especially because the coupon tests exhibited lamina bending. As the coupons failed, the lamina bundles slid along the face of the impacting wall.

Finally, another item to look into will be solid modelling of laminates in order to see the correct failure mode in the simulation. Shell models cannot exhibit delamination of plies, and therefore, they cannot present the lamina bundles that were observed during testing. Solid modelling of laminates will involve a better grasp on through thickness properties and including a tiebreak contact between each layer. The values needed for this tiebreak contact will need testing for mode I and mode II delamination resistance. Solid modelling of laminates will hopefully be able to display the correct failure mode, but will also take much more computational resources than a shell model.

REFERENCES

Adams, D. F. (2005), *Current compression test methods*, available at: http://www.compositesworld.com/articles/current-compression-test-methods (accessed 3rd April 2012).

Agarwal, B. D., Broutman, L. J. and Chandrashekhara, K. (2006), *Analysis and Performance of Fiber Composites,* 3rd ed, John Wiley & Sons, Hoboken, NJ.

ASTM Standard D3039/D3039M, (2008), *Standard Test Method for Tensile Properties of Polymer Matrix Composite Materials*, ASTM International, West Conshohocken, PA.

ASTM Standard D5379/D5379M, (2005), *Standard Test Method for Shear Properties of Composite Materials by the V-Notched Beam Method*, ASTM International, West Conshohocken, PA.

ASTM Standard D695, (2010), *Standard Test Method for Compressive Properties of Rigid Plastics*, ASTM International, West Conshohocken, PA.

Bisagni, C., Di Pietro, G., Fraschini, L. and Terletti, D. (2005), "Progressive crushing of fiber-reinforced composite structural components of a Formula One racing car", *Composite Structures,* vol. 68, no. 4, pp. 491-503.

Chang, F. K. and Chang, K. Y. (1987a), "Post-failure analysis of bolted composite joints in tension or shear-out mode failure", *Journal of Composite Materials,* vol. 21, pp. 809-833.

Chang, F. K. and Chang, K. Y. (1987b), "A progressive damage model for laminated composites containing stress concentration", *Journal of Composite Materials,* vol. 21, pp. 834-855.

Dormegnie, D., Coutellier, D., Delsart, D. and Deletombe, E. (2003), "Studies of scale effects for crash on laminated structures", *Applied Composite Materials,* vol. 10, no. 1, pp. 49-61.

Farley, G. L. (1992), *Relationship between mechanical-property and energy-absorption trends for composite tubes,* L-17087, Vehicle Structures Directorate U.S. Army Research Laboratory Langley Research Center, Hampton, VA.

Hallquist, J.O., (2006), *LS-DYNA Theory Manual*, Livermore Software Technology Corp., Livermore CA.

Hashin, Z. (1980), "Failure criteria for unidirectional fiber composites", *Journal of Applied Mechanics,* vol. 47, no. June, pp. 329-334.

Hexcel Corporation (2005), *Prepreg technology*, available at: www.hexcel.com/Resources/DataSheets/Brochure-Data-Sheets/Prepreg_Technology.pdf (accessed 6th March 2012).

Hull, D. (1991), "A unified approach to progressive crushing of fibre-reinforced composite tubes", *Composites Science and Technology,* vol. 40, no. 4, pp. 377-421.

Jackson, K. E. (1994), "Workshop on scaling effects in composite materials and structures", November 15-16, 1993, Langley Research Center Hampton, Virginia, NASA Conference Publication 3271, pp. 1.

Kubiak, P. (2007), *Simulation of composite material crash energy absorbers for F1 racing cars* (MSc thesis), Cranfield University, Cranfield.

Mahdi, E., Hamouda, A. M. S., Sahari, B. B. and Khalid, Y. A. (2002), "Effect of material and geometry on crushing behaviour of laminated conical composite shells", *Applied Composite Materials,* vol. 9, no. 5, pp. 265-290.

Mamalis, A. G., Manolakos, D. E., Demosthenous, G. A. and Ioannidis, M. B. (1994), "Axial collapse of thin-walled fibreglass composite tubular components at elevated strain rates", *Composites Engineering,* vol. 4, no. 6, pp. 653-677.

Mamalis, A. G., Robinson, M., Manolakos, D. E., Demosthenous, G. A., Ioannidis, M. B. and Carruthers, J. (1997), "Crashworthy capability of composite material structures", *Composite Structures,* vol. 37, no. 2, pp. 109-134.

Matzenmiller, A., Lubliner, J. and Taylor, R. L. (1995), "A constitutive model for anisotropic damage in fiber-composites", *Mechanics of Materials,* vol. 20, no. 2, pp. 125-152.

Mellor, A. N. (2002), "Impact testing in formula one", *International Journal of Crashworthiness,* vol. 7, no. 4, pp. 475-486.

Price, J. N. and Hull, D. (1987), "Axial crushing of glass fibre-polyester composite cones", *Composites Science and Technology,* vol. 28, no. 3, pp. 211-230.

Rezadoust, A. M., Esfandeh, M. and Sabet, S. A. (2008), "Crush behavior of conical composite shells: Effect of cone angle and diameter/wall thickness ratio", *Polymer - Plastics Technology and Engineering,* vol. 47, no. 2, pp. 147-151.

Savage, G. (2010), "Formula 1 Composites Engineering", *Engineering Failure Analysis,* vol. 17, no. 1, pp. 92-115.

Schweizerhof, K., Weimar, K., Münz, T. and Rottner, T. (1998), "Crashworthiness analysis with enhanced composite material models in LS-DYNA – Merits and Limits ", *5th International LS-DYNA Users Conference,* Dearborn MI, .

Tarfaoui, M., Gning, P. B., Davies, P. and Collombet, F. (2007), "Scale and size effects on dynamic response and damage of glass/epoxy tubular structures", *Journal of Composite Materials,* vol. 41, no. 5, pp. 547-558.

Tsai, S. W. and Wu, E. M. (1971), "A general theory of strength for anisotropic materials", *Journal of Composite Materials,* vol. 5, pp. 58-80.

Viot, P., Ballère, L., Guillaumat, L. and Lataillade, J. -. (2008), "Scale effects on the response of composite structures under impact loading", *Engineering Fracture Mechanics,* vol. 75, no. 9, pp. 2725-2736.

Vishay Precision Group (2010)*, Data Book VMM-DB0103-1011 Precision Strain Gages*, available at: http://www.vishaypg.com/doc?50003 (accessed 5th June 2012).

Vishay Precision Group (2011)*, Tech Note TN-509 Errors Due to Transverse Sensitivity in Strain Gages*, available at: http://www.vishaypg.com/doc?11059 (accessed 26th April 2012).

Wright, P. (2001), *Formula 1 Technology,* Society of Automotive Engineers, Warrendale, PA.

APPENDICES

Appendix A Material Testing Results

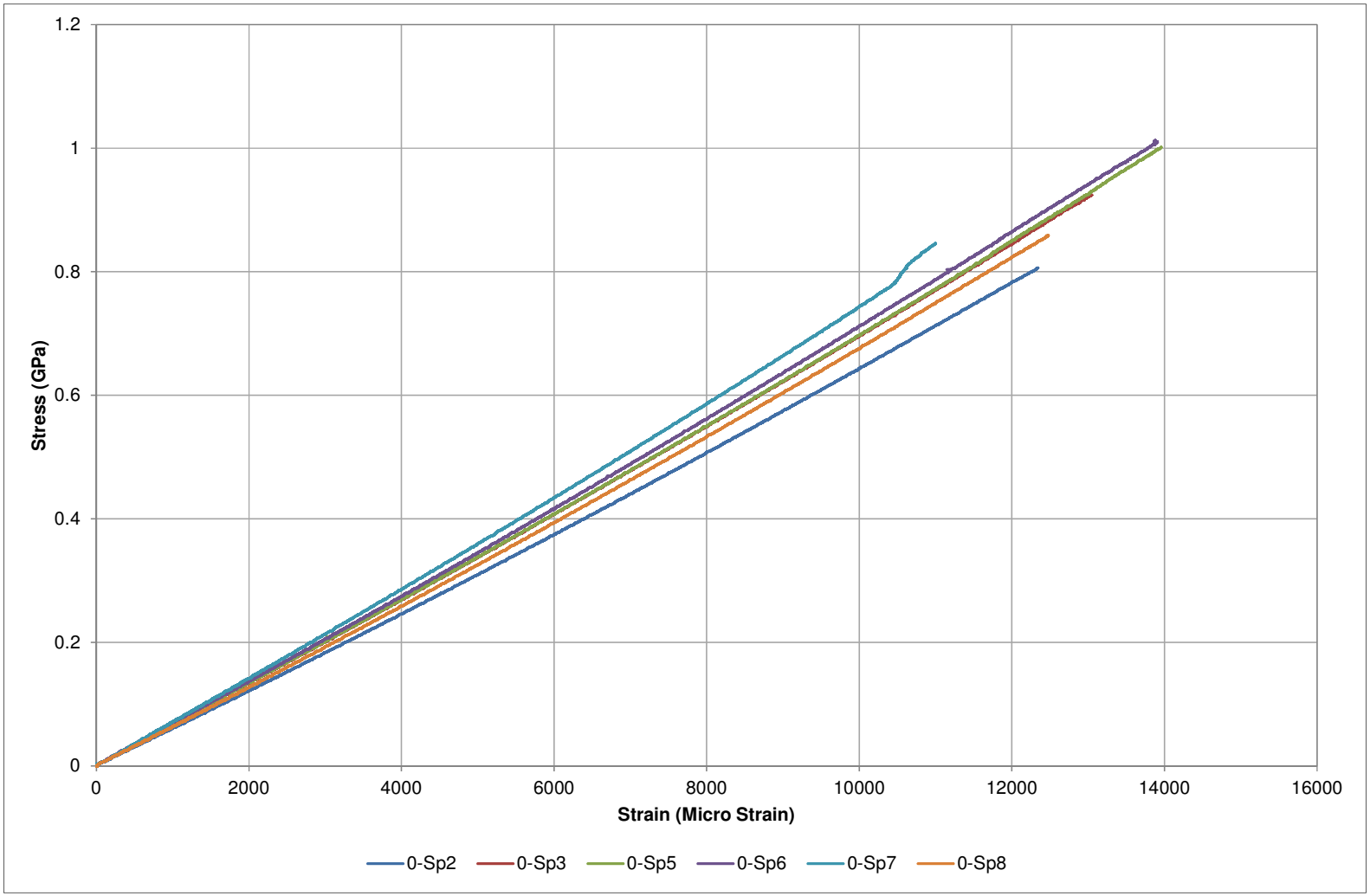

Figure A-1: Tensile Stress versus Corrected Strain - 0 degrees

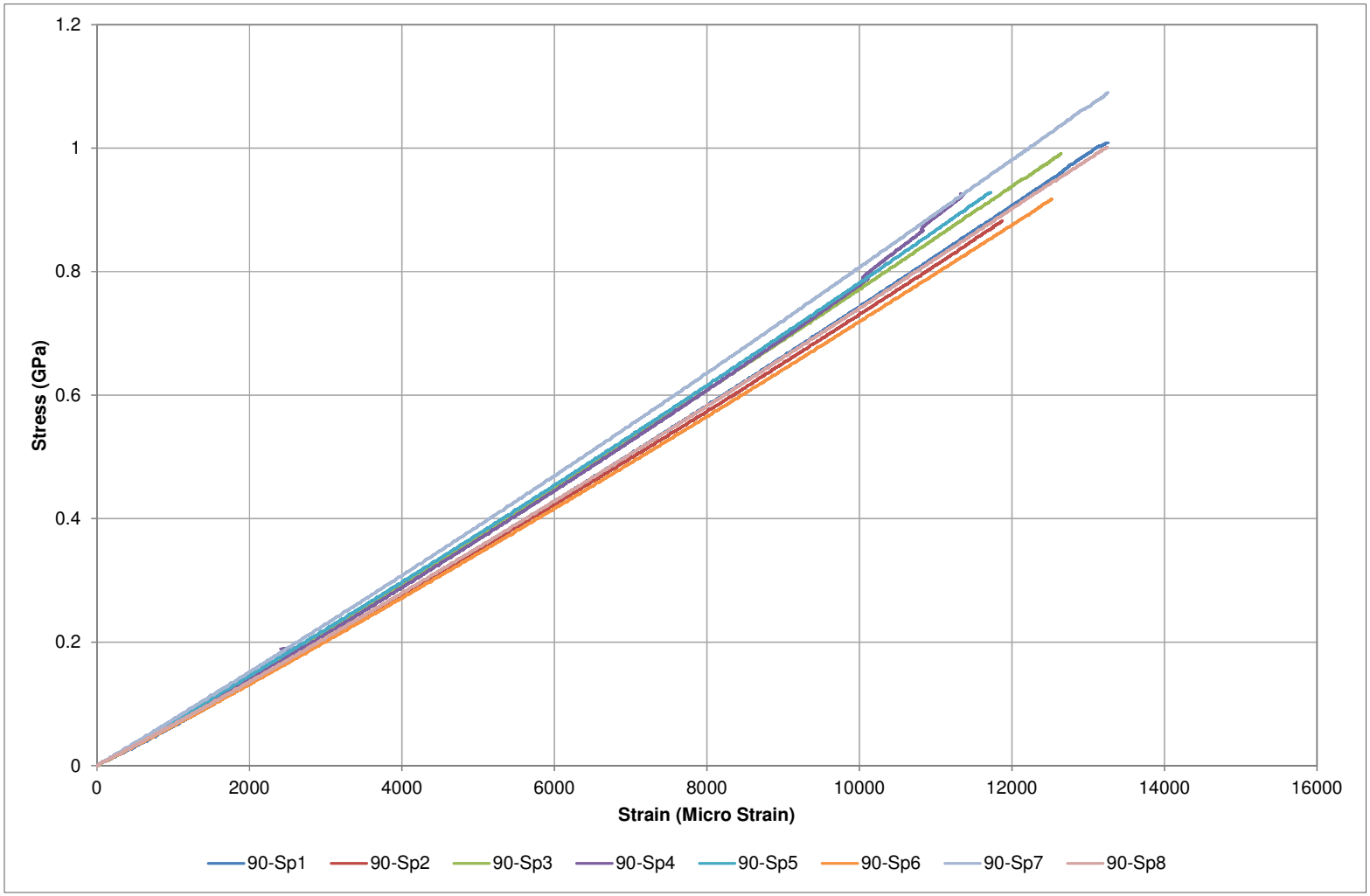

Figure A-2: Tensile Stress versus Corrected Strain - 90 degrees

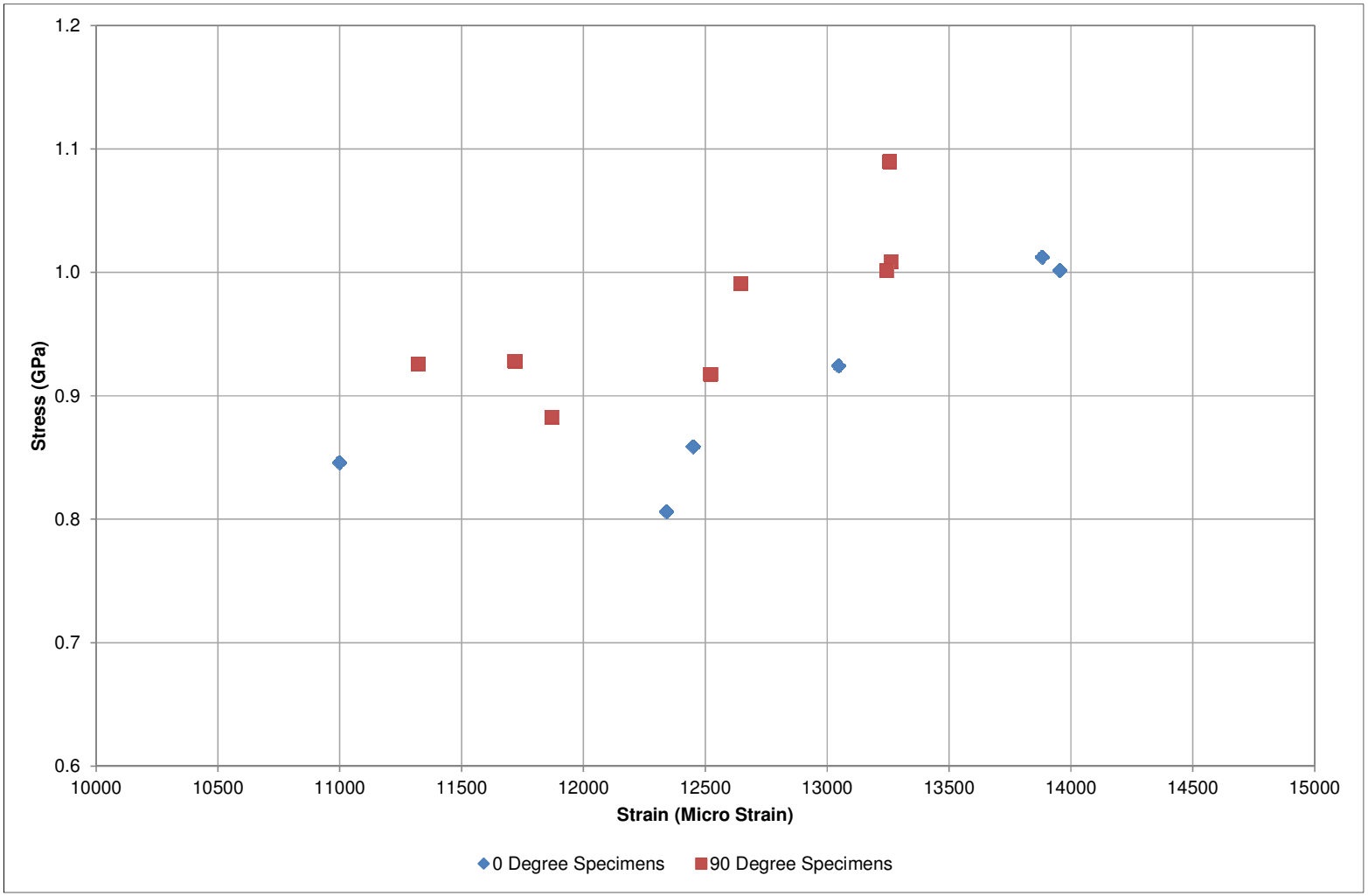

Figure A-3: Tensile Fracture Strength Data Spread

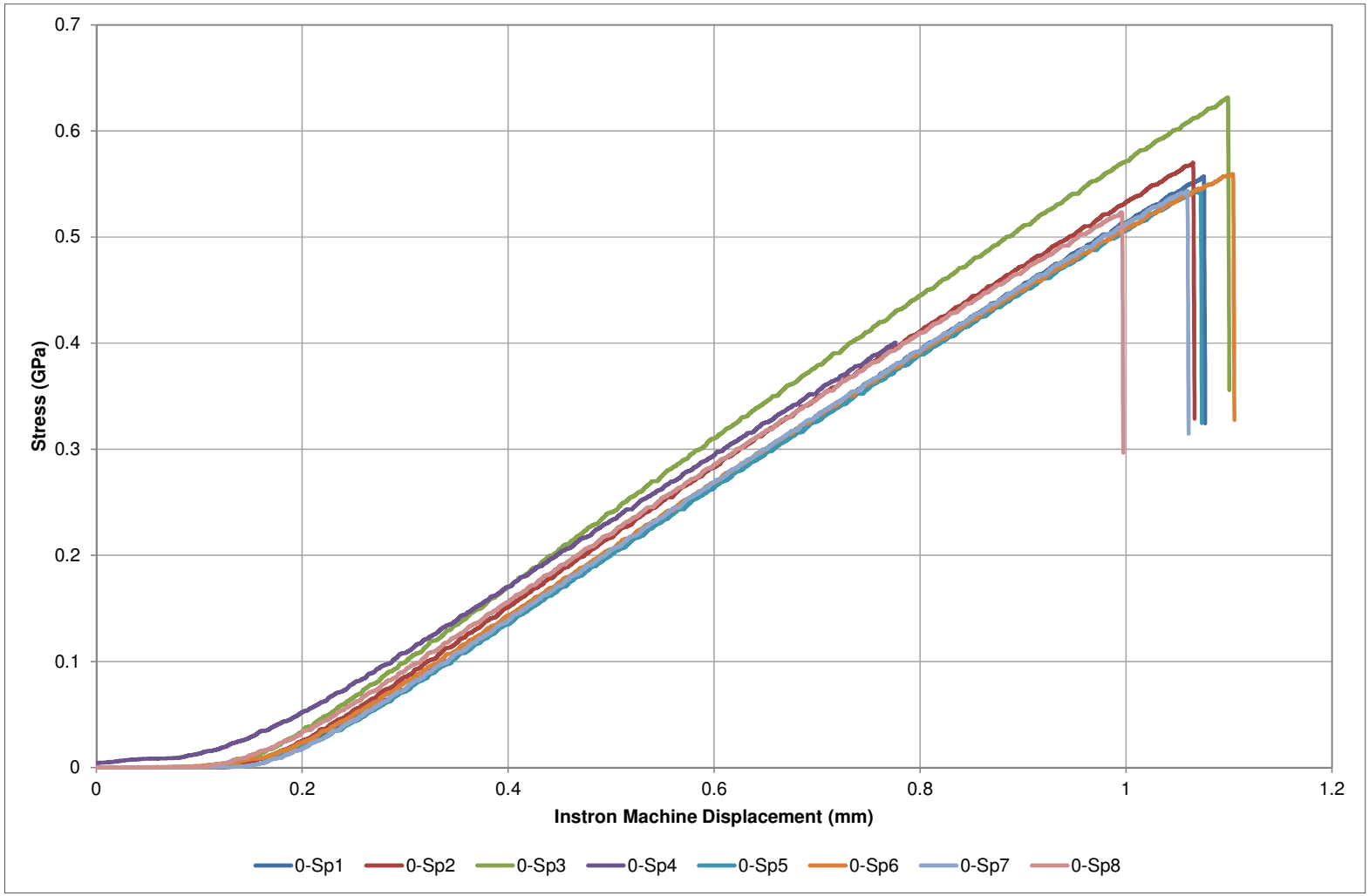

Figure A-4: Compressive Stress versus Displacement - 0 degrees

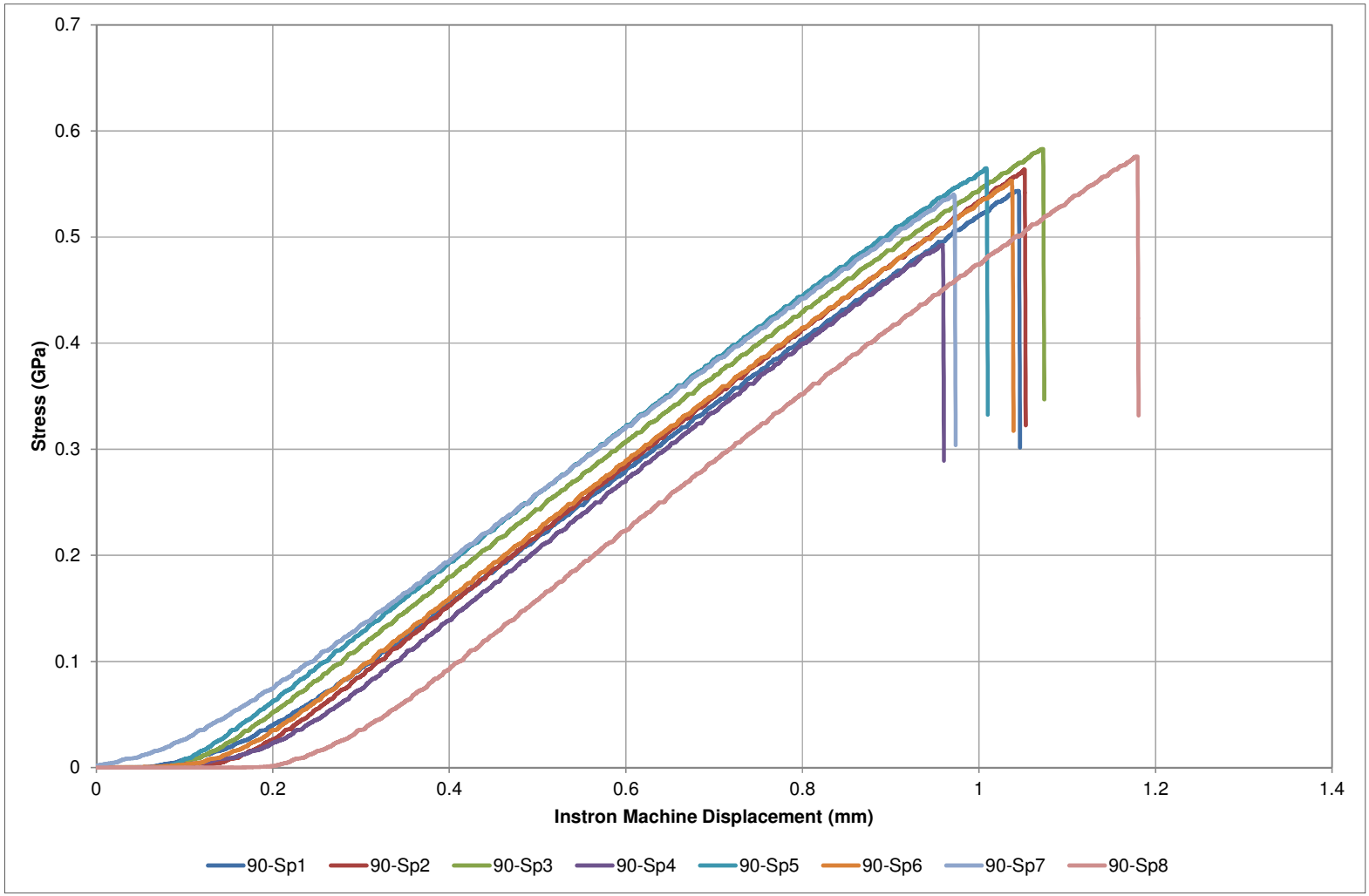

Figure A-5: Compressive Stress versus Displacement - 90 degrees

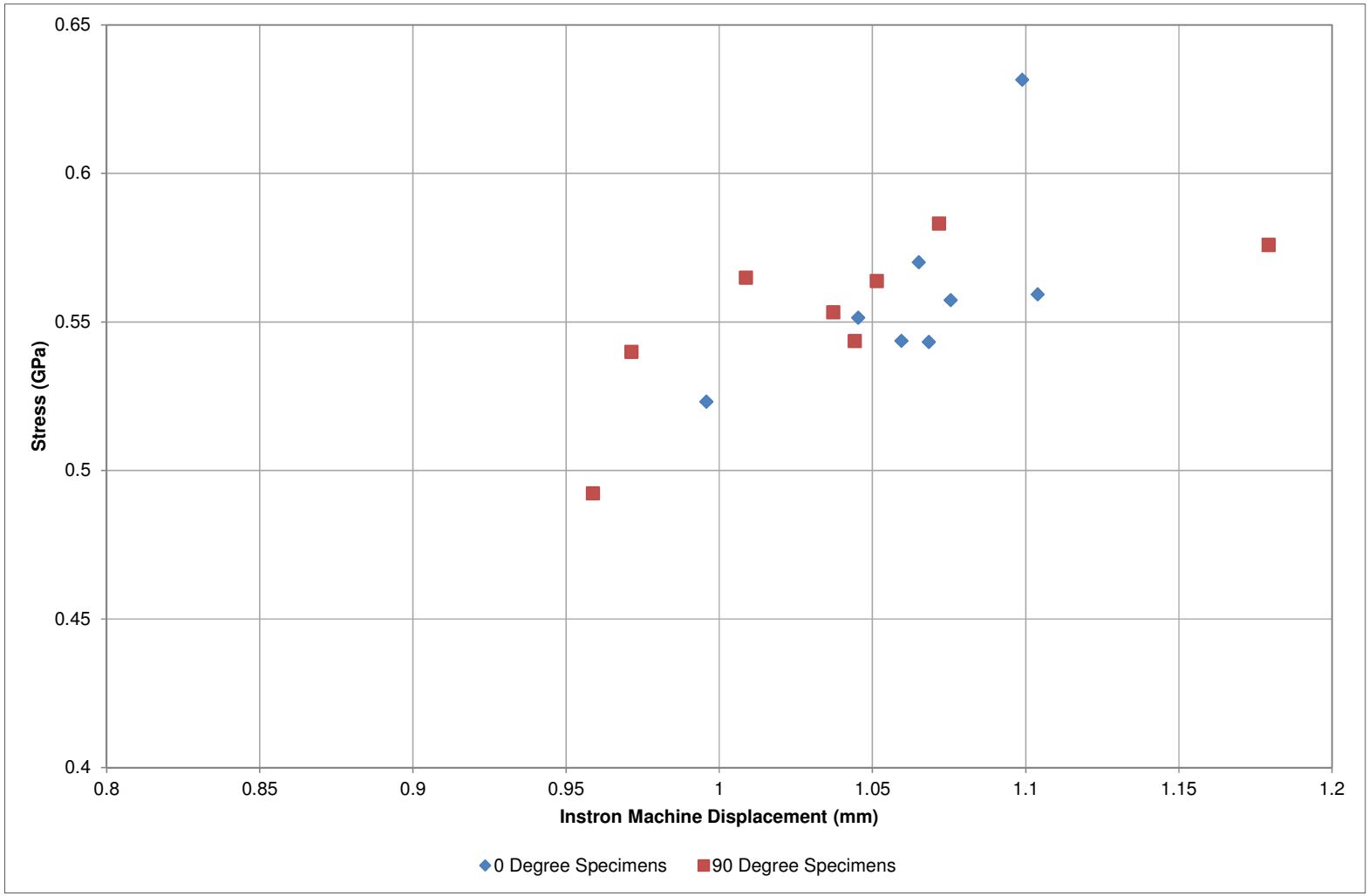

Figure A-6: Compressive Fracture Strength Data Spread

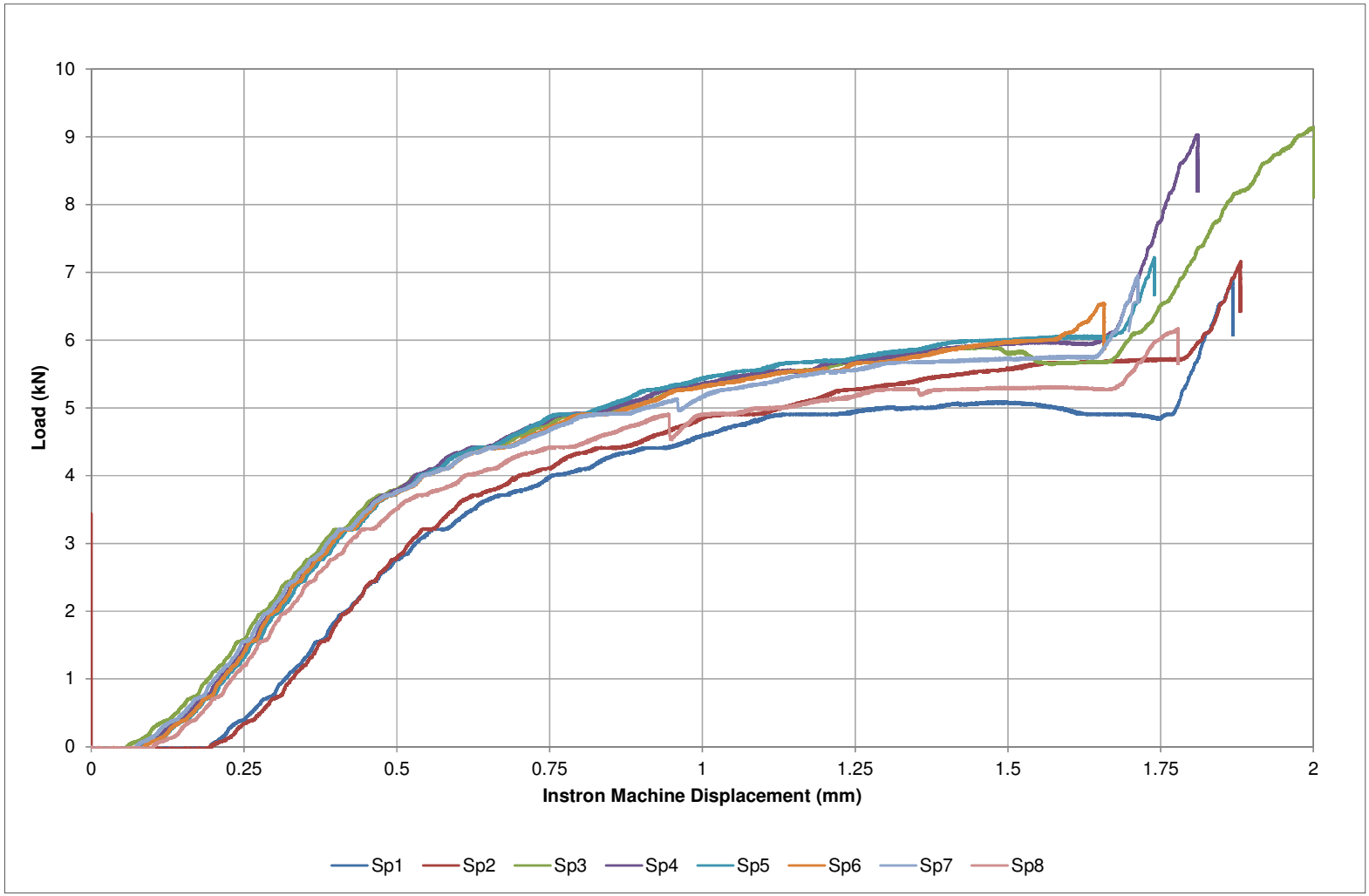

Figure A-7: Shear - Load versus Displacement

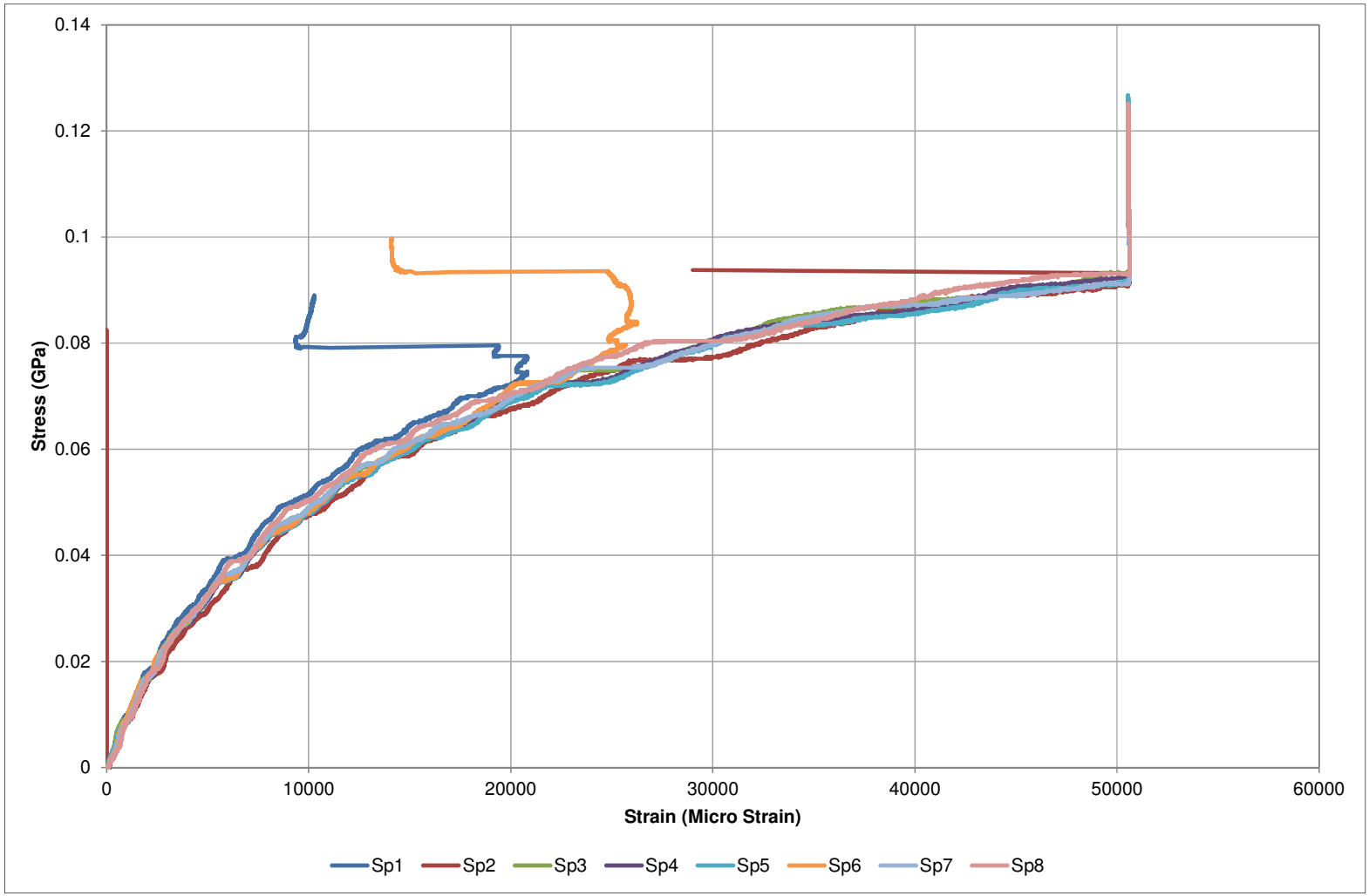

Figure A-8: Shear Stress versus Corrected Strain

Appendix B Transverse Sensitivity of Strain Gauges

Strain gauges are calibrated using a uniaxial state of stress for one material. When the strain gauge is used on a different material or the stress state induced by the testing is something other than a uniaxial state of stress in line with the gauge's sensing axis, the measurements from the strain gauge needs to be corrected for transverse sensitivity. (Vishay Precision Group, 2011)

Per Vishay's (Micro Measurement) Tech Note 509, equations 20 and 21:

$$\varepsilon_1 = \frac{\hat{\varepsilon}_1\left(1 - v_0 K_{t_1}\right) - K_{t_1}\hat{\varepsilon}_2(1 - v_0 K_{t_2})}{1 - K_{t_1}K_{t_2}} \qquad \textbf{Equation 19}$$

$$\varepsilon_2 = \frac{\hat{\varepsilon}_2\left(1 - v_0 K_{t_2}\right) - K_{t_2}\hat{\varepsilon}_1(1 - v_0 K_{t_1})}{1 - K_{t_1}K_{t_2}} \qquad \textbf{Equation 20}$$

Where:

ε_1, ε_2 = the corrected strains along gauge axes (1) and (2)

$\hat{\varepsilon}_1$, $\hat{\varepsilon}_2$ = the uncorrected measured strains along gauge axes (1) and (2)

K_{t_1}, K_{t_2} = the transverse sensitivity coefficients for gauges (1) and (2)

v_0 = the Poisson's ratio of the material on which the manufacturer's gauge factor was measured

The values for the constants K_{t_1}, K_{t_2}, and v_0 that were used for the tensile and shear specimens can be seen in Table B-1.

Table B-1: Transverse Sensitivity Constants

	K_{t_1}	K_{t_2}	v_0
Tensile Specimens	0.005	0.003	0.285
Shear Specimens	0.007	0.007	0.285

Appendix C Material Specimen Profiles

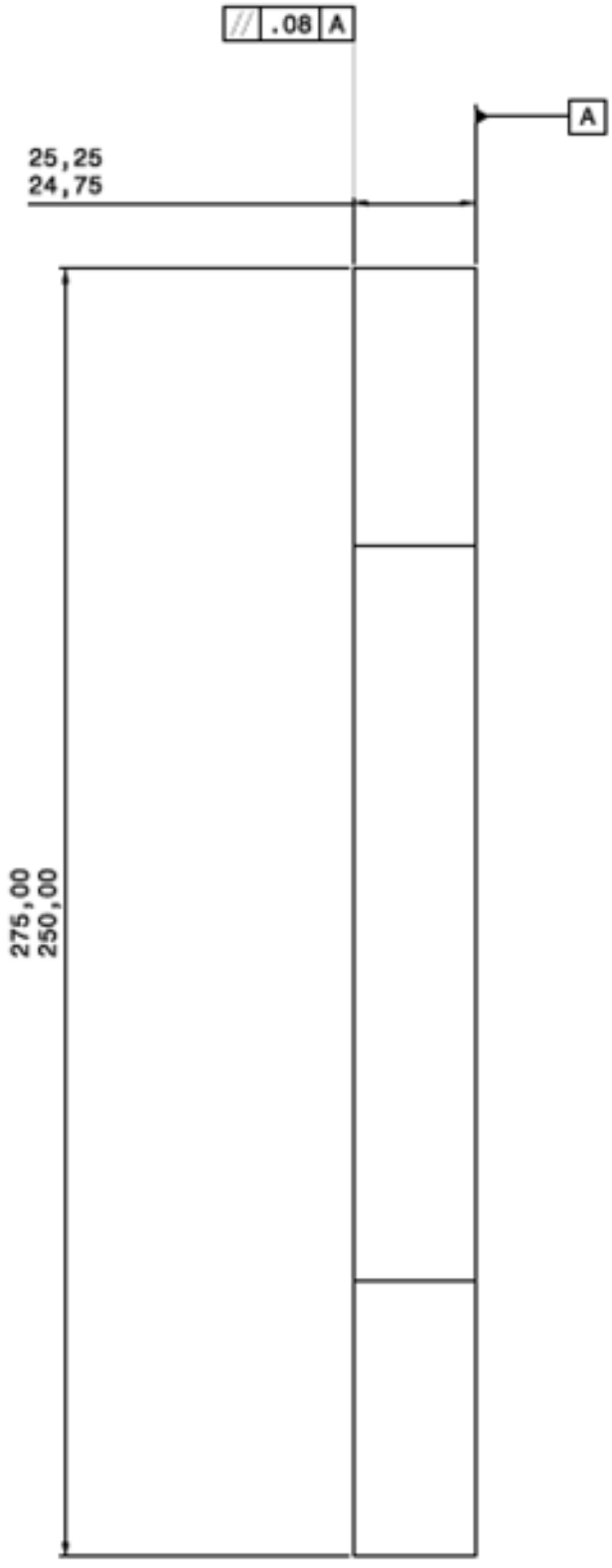

Figure C-9: Tensile Specimen Profile

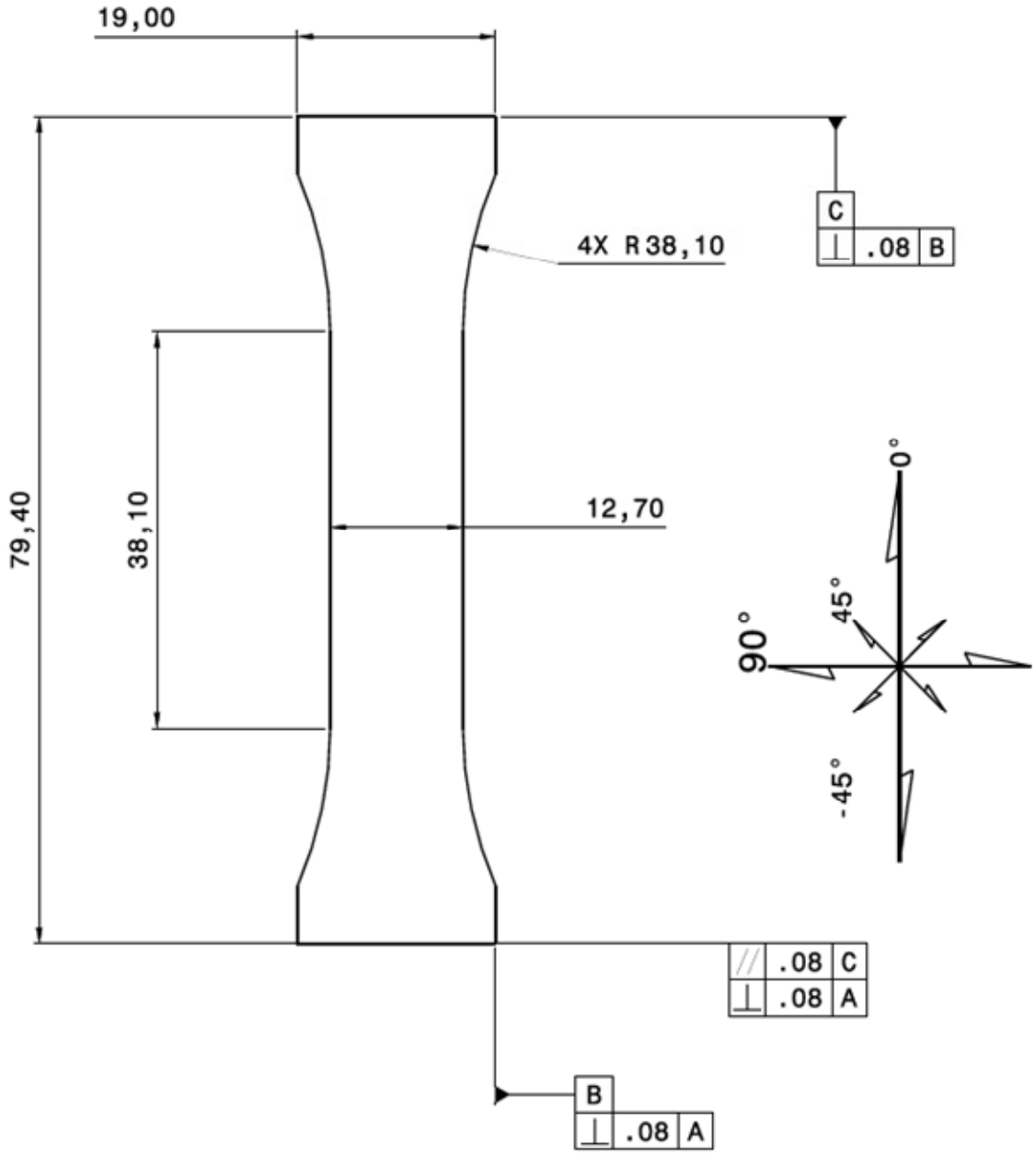

Figure C-10: Compression Specimen Profile

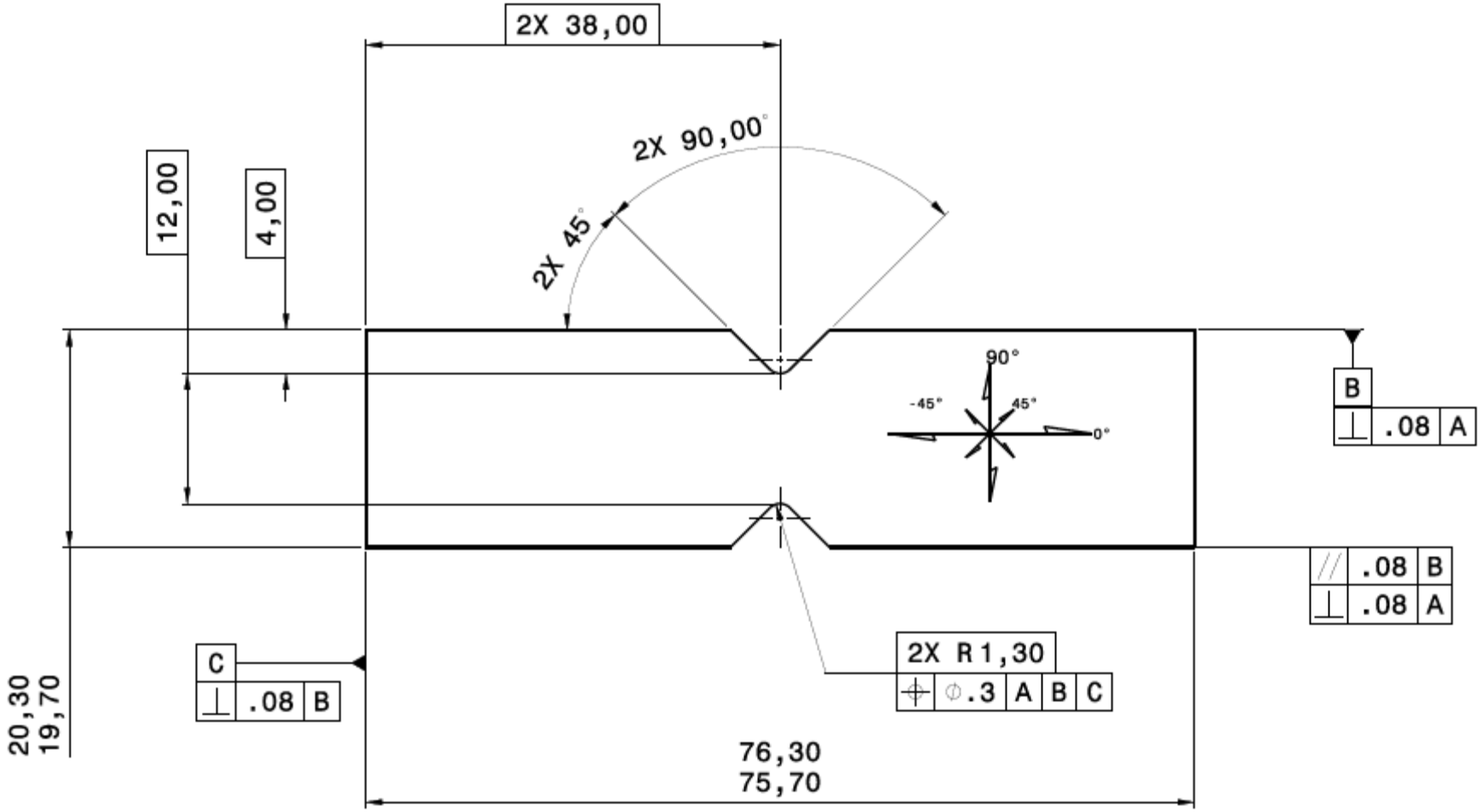

Figure C-11: Shear Specimen Profile

Appendix D Coupon Testing Raw Data

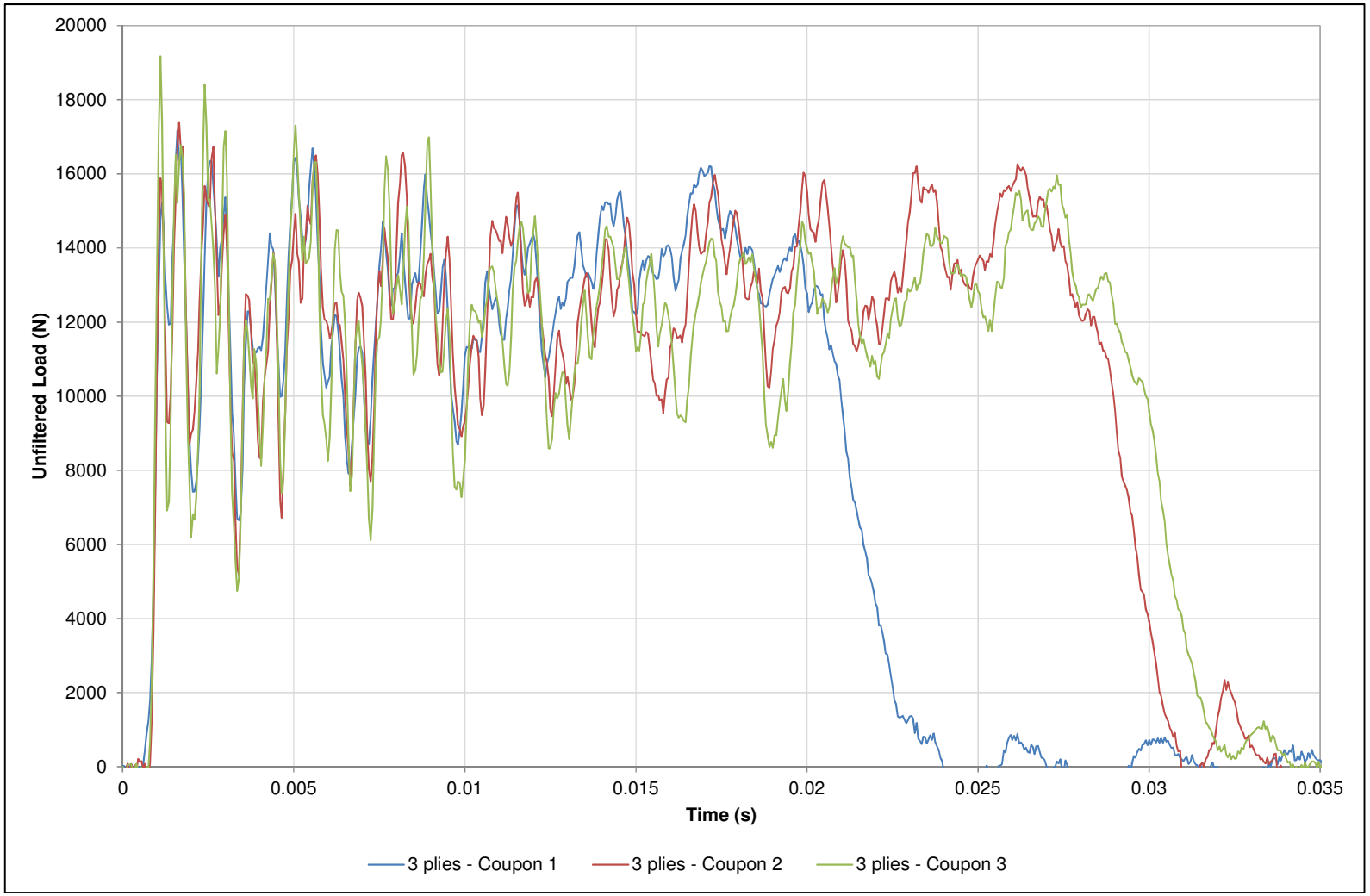

Figure D-12: 3-ply Configuration Test Results

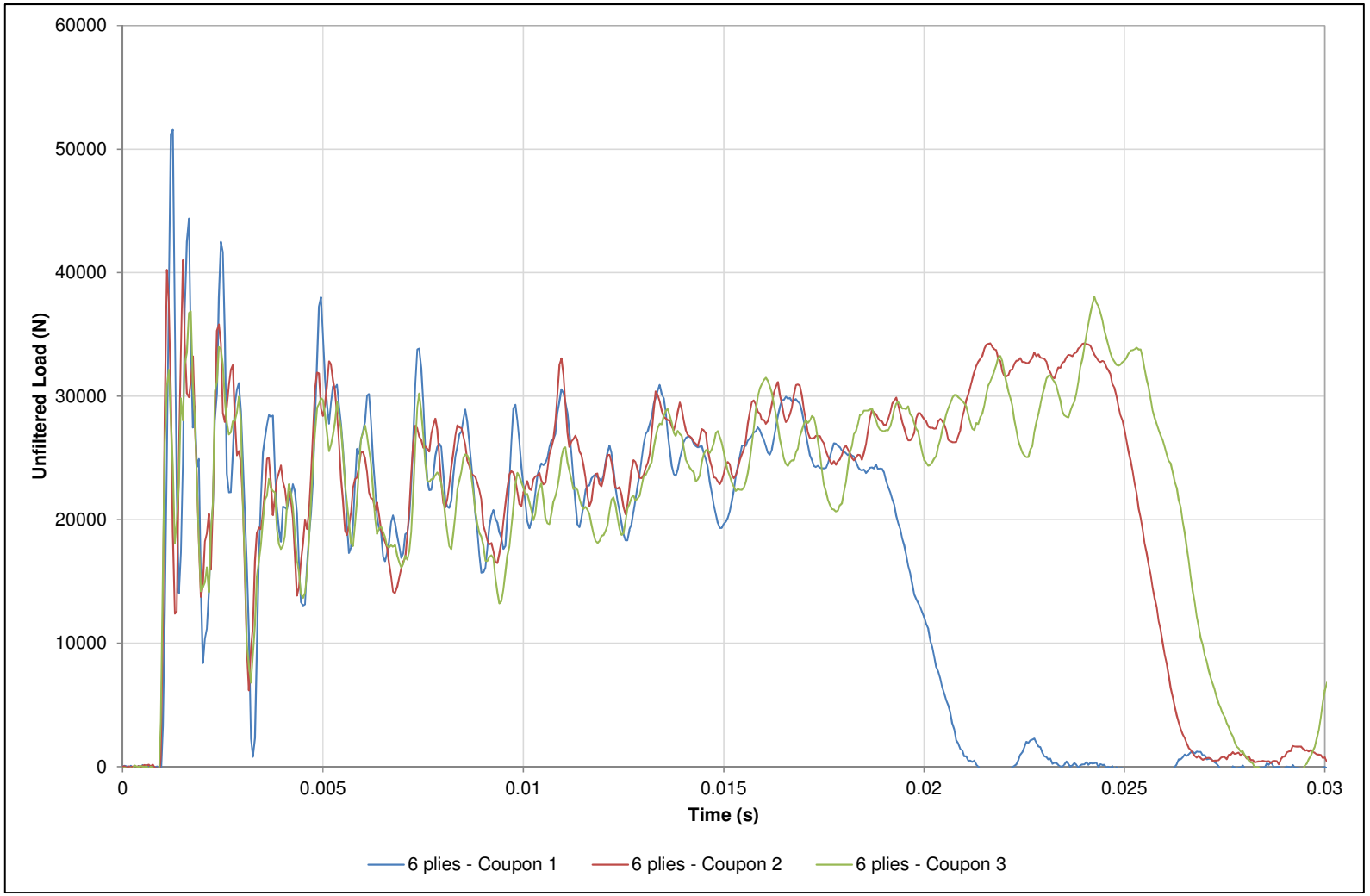

Figure D-13: 6-ply Configuration Test Results

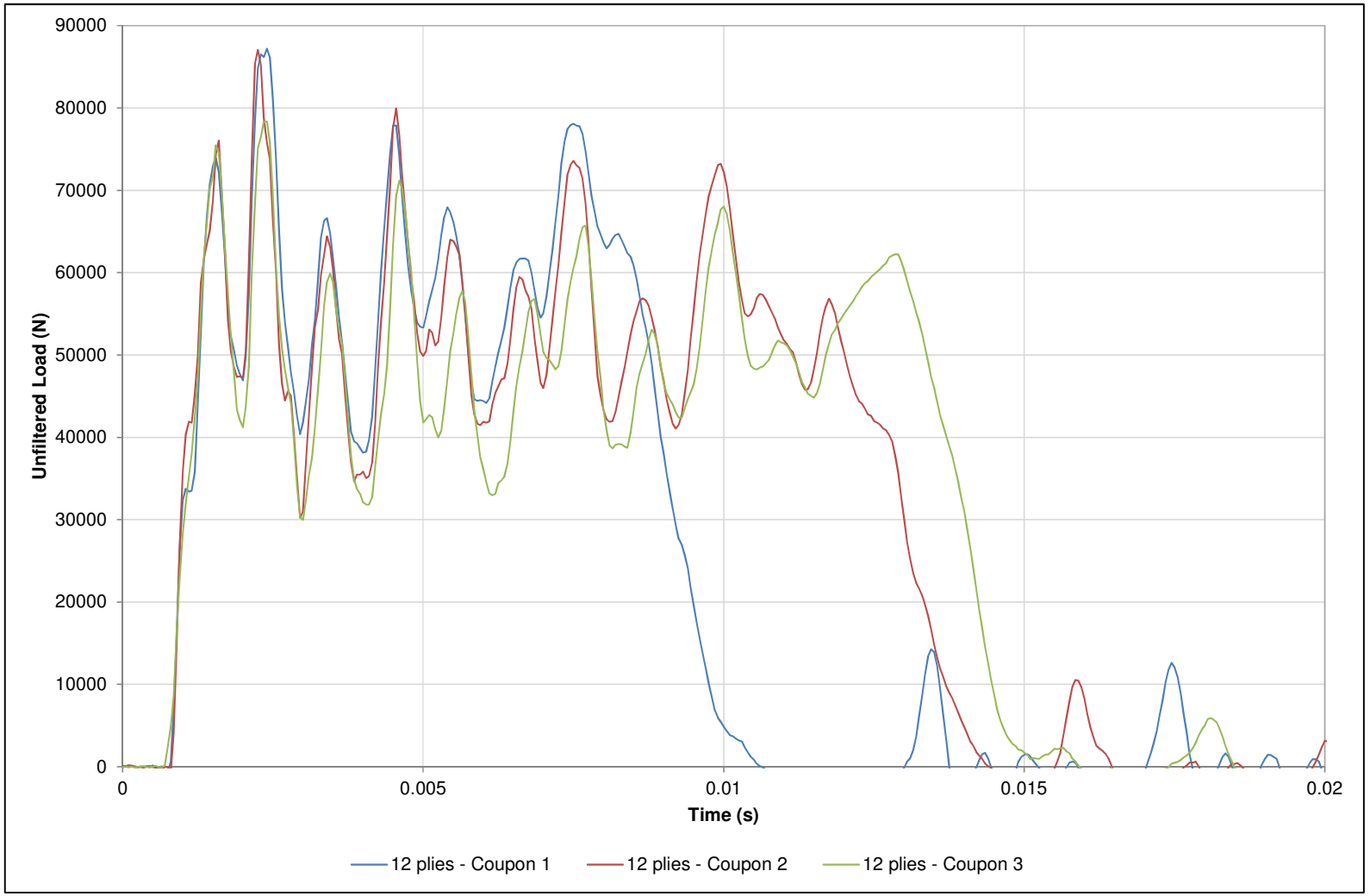

Figure D-14: 12-ply Configuration Test Result